
Compact Binary Merger Simulations in Numerical Relativity

DISSERTATION

zur Erlangung des akademischen Grades
doctor rerum naturalium (Dr. rer. nat.)



vorgelegt dem Rat der
PHYSIKALISCH-ASTRONOMISCHEN FAKULTÄT
der
FRIEDRICH-SCHILLER-UNIVERSITÄT JENA
von

Francesco Maria Fabbri (M.Sc.)

geboren am 11.05.1991 in Pescia, Italy

Gutachter:

1. Prof. Dr. Bernd Brüggemann
Theoretisch-Physikalisches Institut, Friedrich-Schiller-Universität Jena
2. Prof. Dr. Kostas Kokkotas
Universität Tübingen
3. Dr. habil. Sylvio Klose
TLS, Thüringer Landessternwarte Tautenburg

Tag der Disputation: 22.11.2022

Dissertation, Friedrich-Schiller-Universität Jena, [2022]

To Mum and Dad

*“Lo duca e io per quel cammino ascoso
intrammo a ritornar nel chiaro mondo;
e senza cura aver d’alcun riposo,*

*salimmo sù, el primo e io secondo,
tanto ch’i’ vidi de le cose belle
che porta ’l ciel, per un pertugio tondo.*

E quindi uscimmo a riveder le stelle.”

Dante Alighieri

FRIEDRICH-SCHILLER-UNIVERSITÄT JENA

Abstract

PHYSIKALISCH-ASTRONOMISCHE FAKULTÄT

Theoretisch-Physikalisches Institut

zur Erlangung des akademischen Grades doctor rerum naturalium (Dr. rer. nat.)

Compact Binary Merger Simulations in Numerical Relativity

by Francesco Maria FABBRI (M.Sc.)

The era of Gravitational Waves Astronomy was launched after the success of the first observation run of the LIGO Scientific Collaboration and the VIRGO Collaboration. The large laser interferometers incredible achievement prompted the need of extensive studies in the field of compact astrophysical objects, such as Black Holes and Neutron Stars. Today, seven years after this event, the field of study underwent a notable expansion, corroborated by the detection of a signal coming from a Binary Neutron Star merger, together with its electro-magnetic counterpart, and, more recently, by the first detections of signals coming from mixed compact binaries, i.e. Black Hole-Neutron Star binaries.

In this thesis work we span our attention across different aspects of compact objects mergers, including the inclusion of new physics into the already performing numerical relativity code BAM and the study of specific systems of compact objects.

We first explore the treatment of neutrinos in case of Binary Neutron Star mergers and a tool to identify and further analyze regions containing trapped neutrinos, in the hot remnant of such mergers. Neutrinos, play in fact a key role into the rapid processes that characterize the formation of elements in the dynamical ejecta expelled during these catastrophic events.

In the following we explore a variety of configurations of mixed compact binary systems. After the development of the new ID code *Elliptica*, and the steps taken to verify its accuracy, we make use of its capability to evolve sets of physical system with various properties. Exploring the space of parameters we study different spin configurations and magnitudes of single objects and their effects on the merger dynamics.

Contents

Abstract	vii
1 Introduction	1
2 Numerical Relativity	5
2.1 Einstein Equations	5
2.2 3 + 1 decomposition	11
2.3 Gauge conditions	15
3 General Relativistic Hydrodynamics	17
3.1 General Relativistic HydroDynamics Equations (GRHD)	18
3.2 General Relativistic Magneto-HydroDynamics Equations (GRMHD)	23
3.3 Radiative Transport and Microphysics	27
4 Numerical Codes	33
4.1 Initial Data Codes	33
4.2 Evolution Codes	45
5 Results	49
5.1 Neutrinospheres	49
5.2 BAM GRMHD implementation	58
5.3 Mixed Binaries	74
6 Conclusions	97
A General notions about PDEs	101
A.1 Well-posedness	101
A.2 Character of PDEs	101

B 3+1 Evolution Equations	105
B.1 ADM Formalism	105
B.2 BSSNOK Formalism	106
B.3 Z4 Formalism	110
C Conservative Formulations	115
D Equations of State	119
E Recovery of Primitive Variables	123
Bibliography	127
Acknowledgements	149
Additional Material	151

Abbreviations and Notation

We employ the Geometric units, $c = G = M_{\odot} = 1$, unless specified otherwise. In several cases we write c , and M_{\odot} explicitly for clarity. Classical units satisfy the relations

$$1\text{cm} \rightarrow 1.476625 \times 10^{-5} M_{\odot} \quad (1)$$

$$1\text{g} \rightarrow 1.98847 \times 10^{-33} M_{\odot} \quad (2)$$

$$1\text{s} \rightarrow 4.92569 \times 10^6 M_{\odot} \quad (3)$$

For the indices we are adopting *Greek indices* like $\alpha, \beta = 0, 1, 2, 3$ as 4D or spacetime indices, while *Latin indices* like $i, j = 1, 2, 3$ as 3D or spatial indices. For general indices, spanning from 1 to an arbitrary n , we employ $a, b, c, \dots = 1, 2, \dots, n$. We are also adopting *Einstein summation's rule* for which a contraction of indices $^{\alpha}{}_{\alpha}$ (unless otherwise stated) implies a summation over the indices themselves \sum_{α} .

In the following, when we refer to a tensor we usually indicate the full set of covariant/contravariant indices (e.g. the Riemann curvature tensor ${}^{(4)}R_{\alpha\beta\gamma\delta}$). However, for the sake of readability, we might abstain to indicate the full list of indices in the text outside of the equations (e.g. ${}^{(4)}R_{\alpha\beta\gamma\delta} \rightarrow {}^{(4)}R$). We hope that such simplifications won't confuse the reader, leading to mix scalar quantities with tensors of similar notation, and that the context will be clear enough to interpret the symbols in the correct way.

The following abbreviations are used (they are also introduced in the text at their first appearance):

ADM	Arnowitt, Deser and Misner
AH	Apparent Horizon
BH	Black Hole
BAM	Bifunctional Adaptive Mesh
bamps	Bifunctional Adaptive Mesh Pseudo-Spectral
BBH	Binary Black Hole
BNS	Binary Neutron Star
CCSN	Core-Collapse Supernova
CT	Constrained Transport

CTS	Conformal Thin Sandwich
EFE	Einstein's Field Equations
EH	Event Horizon
EOS	Equation Of State
EOB	Effective-One-Body
FFT	Fast Fourier Transform
GHG	Generalized Harmonic Gauge
GR	General Relativity
GRB	Gamma-Ray Burst
GRHD	General-Relativistic Hydrodynamics
GRMHD	General-Relativistic Magnetohydrodynamics
GW	Gravitational Wave
HD	HydroDynamics
HMNS	Hyper-Massive Neutron Star
IMHD	Ideal MagnetoHydroDynamics
ID	Initial Data
ISCO	Innnermost Stable Circular Orbit
IVP	Initial Value Problem
LHS	Left Hand Side
LIGO	Laser Interferometer Gravitational-Wave Observatory
MHD	MagnetoHyroDynamics
NR	Numerical Relativity
NS	Neutron Star
ODE	Ordinary Differential Equation
PDE	Partial Differential Equation
PN	Post-Newtonian
RHS	Right Hand Side
RHD	Relativistic HydroDynamics
SGRB	Short Gamma-Ray Burst
SMNS	Supra-Massive Neutron Star
SN	Supernova
TOV	Tolman-Oppenheimer-Volkoff
XCTS	eXtended Conformal Thin Sandwich

Chapter 1

Introduction

Compact objects have been investigated and studied more and more in recent years. The first detection of Gravitational Waves (GW) from the merger of Binary Black Holes (BBH), made by the LIGO Scientific Collaboration and the VIRGO Collaboration announced in Abbott et al., 2016 (GW150914), and the consequential assignment to Rainer Weiss, Kip Thorne, and Barry Barish of the Nobel Prize in physics for directly detecting Gravitational Waves (see *Nobel Prize in Physics 2017* n.d.), proved the effectiveness of the large laser interferometers and opened up the era of Gravitational Waves Astronomy. Suddenly theoretical models and numerical simulations of Compact Objects, as well as other impactful astrophysical phenomena, were granted an experimental counterpart to rule out and discern the correctness of their results. On top of that, the aim to improve the sensibility and the accuracy of the detections required (and still does) efforts in different fields, from statistical analysis and parameter estimation to numerical simulations.

Simulating compact objects mergers is then important from the point of view of accurate GW signals, for the description of Electro-Magnetic (EM) phenomena and to shed light on the behavior of exotic nuclear matter (i.e. matter in extreme conditions). In fact, no more than two years after the first GW detection, the first signal from a Binary Neutron Star (BNS) merger was detected (see Abbott et al., 2017a), together with a follow-up detection of an EM signal that has been proven to be associated with the BNS merger itself (see Abbott et al., 2017b). The importance of this detection lies in the fact that NSs are the densest astrophysical objects in the Universe, with BHs being the only known denser objects. Contrary to BH though, NS matter is not constrained in space and time by the presence of an event horizon and can be stripped out of the system and/or ejected on the occasion of such cataclysmic event. A close encounter of two such objects can significantly, or completely, disrupt the NS, releasing large amounts of matter and energy that can power the observed Electromagnetic

(EM) and the predicted neutrino signature.

Furthermore, in 2020, the first signals from two compact binary inspirals that are consistent with Black Hole-Neutron Star (BHNS) binaries were detected (see Collaboration et al., 2021). These represent the first confident observations to date of BHNS binaries via any observational means. Mixed binary detections add an ulterior level of complexity into the mix, representing a bridging case with respect to BNS and BBH systems. More work is, in fact, needed into defining a way to establish clear-cut thresholds for parameters related to these astrophysical setups and it can be candidly stated that, due to their complexity and the timeline of the detections, BHNS are the most interesting compact object systems to be studied as of this moment.

Summing up, the world surrounding Gravitational Wave detections is expanding at a phenomenal speed. Physical aspects of different nature are continuously put on the plate and the horizon of possible studies is expanding. The interest in extreme astrophysical phenomena is at an all-time peak and our eyes are now pointed to the sky. The first GW detection proved to the community that experiments often marked as impossible in the past decades are achievable and the payoff of this incredible research effort is enormous. Now the number of collaboration experiments is rising, promising new exceptional discoveries in the years to come.

This thesis work spans different aspects of compact objects merger, from the strictly computational point of view to the analysis of compact object merger of different kinds.

The first part of this thesis work is dedicated to reporting, in a compact and effective way, the concepts and ideas which compose the foundations of Numerical Relativity (NR) i.e., the numerical evolution of astrophysical objects in the context of General Relativity (GR). In particular, we go through the relevant formulas and formulations of NR in Chap. 2 and present the formulations adopted to transpose the relevant GR formulas into code in Chap. 3, discussing the vastly studied General Relativistic HydroDynamics (GRHD) with some of the relevant addition and developments of the recent years.

In Chap. 4 we briefly describe the numerical codes which this work is based on, and their key features, which play an important role in the result obtained.

The second part of this thesis work is solely dedicated to the results obtained, which

have been condensed in Chap. 5, for better readability. In particular, the different aspects of compact objects simulations here developed are presented separately, first presenting the work on the Neutrinospheres published in Endrizzi et al., 2020 in Sec. 5.1, the work on magnetic field augmentation of the `BAM` code (described in Sec. 4.2.1) with the introduction of General Relativistic MagnetoHydroDynamics (GRMHD) formulation in Sec. 5.2 and, lastly, the main work on mixed binaries, composed by a Black Hole and a Neutron Star (BHNS), following the developments of the `Elliptica` code (presented in Rashti et al., 2022) in Sec. 5.3.

Finally, we present the conclusive remarks of this work in Chap. 6.

The thesis work presented in the main chapters is supported by additional discussions in the Appendices. For the sake of brevity, being limited by a word count, we added these further discussions at the end of the manuscript. More extensively, we cover the key concepts of Partial Differential Equations (PDE) in Appendix A; we explicitly show the most important formulations related to 3+1 decomposition in Appendix B; we explain the characteristics and the importance of Conservative Formulations in Appendix C and give a brief introduction about Equations of States (EOS) to describe nuclear interactions inside a Neutron Star (NS) in Appendix D. Finally, leaning on the computational side, we outline the importance of the Recovery of Primitive Variables in Appendix E.

Chapter 2

Numerical Relativity

2.1 Einstein Equations

In this chapter, we present the expression for the so-called Einstein's Field Equations (EFE) and the fundamental properties and consequences derived from them.

Making use of the key concepts of Differential Geometry (see, for example, Spivak, 1975 for a brief overview of the subject), we can define the **Riemann curvature tensor** as a map:

$$R(-, -) : \mathcal{V}(\mathcal{M}) \times \mathcal{V}(\mathcal{M}) \times \mathcal{V}(\mathcal{M}) \rightarrow \mathcal{V}(\mathcal{M}), \quad (2.1)$$

with

$$R(V, W)Z = D(V, D(W, Z)) - D(W, D(V, Z)) - D([V, W], Z), \quad (2.2)$$

where $[V, W](f) = V(W(f)) - W(V(f))$ are the *Lie brackets* or *commutators*. With the appropriate choice of coordinate basis, the Riemann curvature tensor on a 4D-Riemannian manifold can be expressed as

$$R_{\beta\gamma\delta}^{\alpha} = \partial_{\gamma}\Gamma_{\delta\beta}^{\alpha} - \partial_{\delta}\Gamma_{\gamma\beta}^{\alpha} + \Gamma_{\gamma\tau}^{\alpha}\Gamma_{\delta\beta}^{\tau} - \Gamma_{\delta\tau}^{\alpha}\Gamma_{\gamma\beta}^{\tau}, \quad (2.3)$$

with properties

$$R_{\beta\gamma\delta}^{\alpha} = -R_{\beta\delta\gamma}^{\alpha}, \quad (2.4)$$

$$R_{\beta\gamma\delta}^{\alpha} + R_{\gamma\delta\beta}^{\alpha} + R_{\delta\beta\gamma}^{\alpha} = 0, \quad (2.5)$$

$$\nabla_{\mu}R_{\beta\gamma\delta}^{\alpha} + \nabla_{\gamma}R_{\beta\delta\mu}^{\alpha} + \nabla_{\delta}R_{\beta\mu\gamma}^{\alpha} = 0, \quad (2.6)$$

where Eq. (2.6) are called *Bianchi identities*.

We can define then the **Ricci tensor** as

$$R_{\mu\nu} = R_{\mu\tau\nu}^{\tau}. \quad (2.7)$$

Now putting ourselves on a Riemaniann manifold we can consider the unique symmetric compatible connection derived by the metric, in terms of which we can write

$$R_{\alpha\beta\gamma\delta} = g_{\mu\alpha} R_{\beta\gamma\delta}^{\mu}, \quad (2.8)$$

with properties:

$$R_{\alpha\beta\gamma\delta} = -R_{\beta\alpha\gamma\delta}, \quad (2.9)$$

$$R_{\alpha\beta\gamma\delta} = R_{\gamma\delta\alpha\beta}, \quad (2.10)$$

$$R_{\mu\nu} = R^{\nu\mu}. \quad (2.11)$$

We can finally define the **Ricci scalar** as

$$R = R_{\mu}^{\mu}, \quad (2.12)$$

and the **Einstein tensor** as

$$G_{\mu\nu} = R_{\mu\nu} - \frac{1}{2}g_{\mu\nu}R, \quad (2.13)$$

which, as a consequence of the Bianchi identities in Eq. (2.6), is divergence-less

$$\nabla_{\nu}G^{\mu\nu} = 0. \quad (2.14)$$

Lastly, we need to derive the **Einstein field equations**, the fundamental block of the theory on which this thesis is based. For simplicity, we start from the Einstein equation in vacuum. We first assume a *Lagrangian theory* for a description of the gravitational field

$$\mathcal{L}(\mathbf{g}, \partial\mathbf{g}) = R = g^{\mu\nu}R_{\mu\nu}, \quad (2.15)$$

where we use \mathbf{g} to indicate the metric to distinguish from the determinant $g = \det(\mathbf{g})$.

We can then write the action in the form

$$\mathcal{S}_G[\mathbf{g}] = \int_{\mathcal{M}} \mathcal{L}(\mathbf{g}, \partial\mathbf{g})\sqrt{-g}d^4x = \int_{\mathcal{M}} R\sqrt{-g}d^4x, \quad (2.16)$$

and applying the variational principle we obtain

$$\delta\mathcal{S}_G[\mathbf{g}] = \int_{\mathcal{M}} d^4x [\sqrt{-g}g^{\mu\nu}\delta R + \sqrt{-g}(\delta g_{\mu\nu})R^{\mu\nu} + g^{\mu\nu}R_{\mu\nu}\delta(\sqrt{-g})]. \quad (2.17)$$

Since listing all the calculations is beyond the scope of this work, we can directly jump to

$$R_{\mu\nu} - \frac{1}{2}g_{\mu\nu}R = 0, \quad (2.18)$$

or

$$G_{\mu\nu} = 0, \quad (2.19)$$

which are the **Einstein field equations in vacuum**. We can split this set of equations into two subsets, namely

$$R_j^i - \frac{1}{2}\delta_j^i R = 0, \quad (2.20)$$

which are 6 equations containing second derivatives with respect to x^0 of g_{ij} and first derivatives of $g_{0\mu}$ and

$$R_j^0 = 0, \quad (2.21)$$

$$R_0^0 - \frac{1}{2}R = 0, \quad (2.22)$$

which only contains first derivatives with respect to x^0 of g_{ij} . Eq. (2.21) and (2.22) are also referred to as the *constraints* of the system, since they put restrictions on the choice of the initial conditions. They represent the arbitrariness in the choice of the reference system, resulting from the principle of *general covariance*.

The Einstein equations in vacuum (2.20) have another important consequence: they describe the propagation of the gravitational field in empty space and, analogously to electromagnetism, predict the existence of gravitational waves, i.e. perturbations in the gravitational field that propagate at the speed of light c (see Eq. (2.32)). To get the complete set of equations we then need to add the source terms to Eq. (2.20). We first need to define the **Stress-Energy tensor** $T^{\mu\nu}$. To do so, we consider a *Field Theory* with N fields ϕ^a , $a = 1, \dots, N$ that admits a Lagrangian formulation so that

$$T_\nu^\mu = \frac{\partial\mathcal{L}}{\partial(\partial_\mu\phi^a)}(\partial_\nu\phi^a) - \delta_\nu^\mu\mathcal{L} \quad (2.23)$$

is the stress-energy tensor, which is divergence-less, i.e.

$$\partial_\mu T_\nu^\mu = 0, \quad (2.24)$$

if \mathcal{L} doesn't depend explicitly on the coordinates. This tensor, as the name suggests, is related to the energy/matter distributions and properties (as we will see in Ch. 3), hence it poses as the source term in Einstein equations.

Now applying again the variational principle to

$$\mathcal{S} = \int_{\mathcal{M}} d^4x \sqrt{-g} \mathcal{L}(\phi, \partial\phi, \mathbf{g}, \partial\mathbf{g}), \quad (2.25)$$

we end up with the complete set of **Einstein equations**

$$G_{\mu\nu} = R_{\mu\nu} - \frac{1}{2}g_{\mu\nu}R = 8\pi T_{\mu\nu}. \quad (2.26)$$

These equations are the building block of *General Relativity* and represent a generalization of the relativistic Newton's field equation

$$\nabla\phi = 4\pi\rho. \quad (2.27)$$

Gravitational Waves To extract the equations that describe gravitational waves we begin by assuming a small perturbation of the flat *Minkowski* metric $\eta_{\mu\nu}$:

$$\eta_{\mu\nu} = \begin{pmatrix} -1 & 0 & 0 & 0 \\ 0 & +1 & 0 & 0 \\ 0 & 0 & +1 & 0 \\ 0 & 0 & 0 & +1 \end{pmatrix},$$

which we can write as

$$g_{\mu\nu} = \eta_{\mu\nu} + h_{\mu\nu}, \quad (2.28)$$

with $|h_{\mu\nu}| \ll 1$. With this linear expansion we can also write

$$R_{\alpha\beta\gamma\delta} = \frac{1}{2}(\partial_\beta\partial_\gamma h_{\alpha\delta} + \partial_\alpha\partial_\delta h_{\beta\gamma} - \partial_\beta\partial_\delta h_{\alpha\gamma} - \partial_\alpha\partial_\gamma h_{\beta\delta}). \quad (2.29)$$

To quickly show the relevant solution we first define the *trace reversed* field tensor

$$\bar{h}_{\mu\nu} \equiv h_{\mu\nu} - \eta_{\mu\nu} \frac{h}{2}, \quad (2.30)$$

and the gauge choice that we associate with this transformation

$$\partial_\mu \bar{h}^{\mu\nu} = 0, \quad (2.31)$$

which is called the *Lorentz Gauge* and is of the same type of the which used in electromagnetism.

With these choices, we finally obtain the field equation

$$\square \bar{h}_{\mu\nu} = -16\pi T_{\mu\nu}, \quad (2.32)$$

where $\square = g^{\mu\nu} \partial_\mu \partial_\nu$ is the d'Alambertian operator in flat space.

As stated before, Eq. (2.32) represents a wave equation for the gravitational field.

To find a solution we start with the trivial ansatz of a plane wave solution

$$\bar{h}_{\mu\nu} = \hat{h}_{\mu\nu} e^{ik_\mu x^\mu}, \quad (2.33)$$

where $\hat{h}_{\mu\nu}$ is the *amplitude tensor* and k_μ the *wave vector*. Making use of Eq. (2.32) we have that

$$\eta^{\mu\nu} k_\mu k_\nu = k_\nu k^\nu = 0, \quad (2.34)$$

so k_μ is a null vector and using the Lorentz gauge

$$\hat{h}^{\mu\nu} k_\nu = 0, \quad (2.35)$$

we can see how the amplitude vector is orthogonal to the wave vector.

Having still freedom within the choice of the Lorentz gauge, we put ourselves in the so-called *transverse-traceless gauge* (TT)

$$\square \xi^\mu = 0, \quad (2.36)$$

which for our case reads as

$$\hat{h}_\mu^\mu = 0 \text{ and } \hat{h}_{\mu\nu} u^\nu = 0 \quad (2.37)$$

for an arbitrary constant 4-velocity u^ν (i.e. an arbitrary timelike unit vector). In particular, we can assume a propagation along z -axis and write, in matrix form,

$$\hat{h}_{\mu\nu}^{TT} = \begin{pmatrix} 0 & 0 & 0 & 0 \\ 0 & h_+ & h_\times & 0 \\ 0 & h_\times & -h_+ & 0 \\ 0 & 0 & 0 & 0 \end{pmatrix},$$

where h_+ and h_\times are the remaining degrees of freedom and are commonly referred to as the two polarizations of gravitational waves. To visualize the effect of the two different polarizations refer to Fig. 2.1

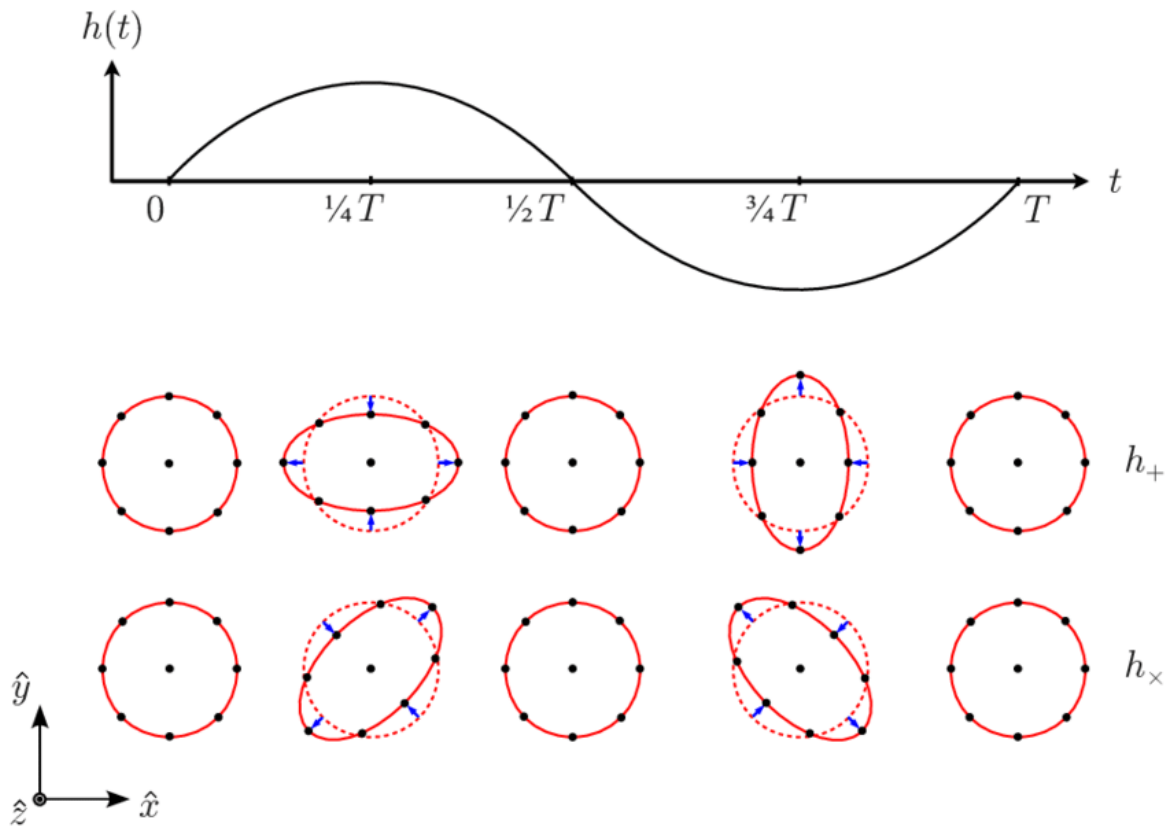


FIGURE 2.1: Effect of a monochromatic gravitational wave of pulsation $\omega = 2\pi/T$ propagating along the z direction. The lower panel shows the effects of $+$ and \times polarizations on a ring of freely falling particles, in a local inertial frame. These effects show why the two polarizations are labeled as such.

From Le Tiec et al., 2016

2.2 3 + 1 decomposition

2.2.1 Foliation

In section Sec. 2.1 we wrote Einstein's field equation, in a manifold \mathcal{M} , in a fully covariant way. In this form, directly derived from differential geometry, all dimensions are treated in a similar way. From now on we localize ourselves on a 4D-spacetime. All the equations derived before remain valid, only we assume the manifold to be 4D. In order to computationally evolve the 4D-spacetime, we employ a technique called **3+1 decomposition**, in which the 4D-spacetime domain of the simulation is divided into a 3D slice and a 1D time evolution axis. We assume that the manifold \mathcal{M} (space-time) in exam is globally hyperbolic, i.e. that there exists a set \mathcal{C} that is spacelike and if chronologically extended in the past and future it covers the entire manifold. More loosely speaking, a globally hyperbolic manifold is such that we can define a concept of causality for every point contained. For the sake of our discussion, a globally hyperbolic spacetime can be completely *foliated*, i.e. fully decomposed into 3D spacelike hypersurfaces Σ . To identify different hypersurfaces we can define a global parameter t that can be considered as a universal time function. Passing from a hypersurface at time Σ_t to a hypersurface at time Σ_{t+dt} we can define two key functions:

- **Lapse function** (α): describes the change in proper time $d\tau$ between the two hypersurfaces along the *normal* or *Eulerian* direction as in

$$d\tau = \alpha(t, x^i)dt. \quad (2.38)$$

- **Shift vector** (β^i): describes the change in spatial coordinates moving from a hypersurface (Σ_t) to the following (Σ_{t+dt}) moving along *normal* or *Eulerian* direction as in

$$x^i_{t+dt} = x^i - \beta^i(t, x^j)dt. \quad (2.39)$$

In terms of α and β^i the metric is split as

$$ds^2 = (-\alpha^2 + \beta_i\beta^i)dt^2 + 2\beta_idtdx^i + \gamma_{ij}dx^idx^j, \quad (2.40)$$

so the metric tensor is

$$g_{\mu\nu} = \begin{pmatrix} -\alpha^2 + \beta_k\beta^k & \beta_i \\ \beta_j & \gamma_{ij} \end{pmatrix},$$

$$g^{\mu\nu} = \begin{pmatrix} -1/\alpha^2 & \beta^i/\alpha^2 \\ \beta^j/\alpha^2 & \gamma^{ij} - \beta^i\beta^j/\alpha^2 \end{pmatrix}.$$

Now we can differentiate between the 4-metric $g_{\mu\nu}$ and the 3-metric γ_{ij} . In the same way, we can establish a relation for the determinants:

$$\sqrt{-g} = \alpha\sqrt{\gamma}. \quad (2.41)$$

In addition, we can specify the coordinates of the unit normal vector to the hypersurface n with these two variables

$$n^\mu = \frac{1}{\alpha}(1, -\beta^i), \quad n_\mu = -\alpha(1, 0), \quad (2.42)$$

which has properties $n^\mu n_\mu = -1$, i.e. it is timelike. We can then define the *time vector* t^μ in terms of $\beta^\mu = (0, \beta^i)$ as

$$t^\mu = \alpha n^\mu + \beta^\mu. \quad (2.43)$$

This 4-vector is basically the tangent vector to lines of constant spatial coordinates. We have that $t^\mu n_\mu = -\alpha$, thus $t^\mu \nabla_\mu t = 1$.

Finally, we express the spatial metric as a full 4-tensor as

$$\gamma_{\mu\nu} = g_{\mu\nu} + n_\mu n_\nu, \quad (2.44)$$

where $n^\nu \gamma_{\mu\nu} = 0$.

2.2.2 Intrinsic and Extrinsic Curvature

As a key feature of this decomposition, we need to distinguish between the properties of the 3D hypersurface and its behavior in the full 4D spacetime. In particular, as we have seen in Sec. 2.1, we need to adapt the concept of curvature, usually described by the Riemann tensor, to our foliated spacetime. In practice, we are going to replicate the decomposition of the metric to the rest of the relevant physical quantities.

From this point on, we are going to fix a clear distinction between vectors/tensors defined on the 3D-hypersurface and the full 4D-spacetime. Hence we will indicate with ⁽⁴⁾ the full 4D quantities and with ⁽³⁾ the local ones (to the hypersurface). Now the curvature of the manifold can be seen as divided into an intrinsic curvature i.e. the Riemann curvature tensor of the 3D-hypersurface ⁽³⁾ R and an extrinsic curvature K , defined by the parallel transport of the normal vector on the hypersurface and that

describes the relation by the 3D hypersurfaces and the whole 4D-spacetime. For the sake of our decomposition we define

$$P_\nu^\mu \equiv \delta_\nu^\mu + n^\mu n_\nu \quad (2.45)$$

as the projection operator, which projects all tensorial quantities onto the hypersurface. In our decomposition, we use the definition

$$P_{\mu\nu} \equiv \gamma_{\mu\nu}. \quad (2.46)$$

Using the projector operator we define the **extrinsic curvature** as

$$K_{\mu\nu} = -P_\mu^\sigma \nabla_\sigma n_\nu \quad (2.47)$$

$$= -(\nabla_\mu n_\nu + n_\mu n^\sigma \nabla_\sigma n_\nu) \quad (2.48)$$

$$= -P_\mu^\alpha P_\nu^\beta \nabla_\alpha n_\beta, \quad (2.49)$$

which is symmetric and purely spatial, so we have

$$K_{\mu\nu} = K_{\nu\mu}, \quad (2.50)$$

$$n^\mu K_{\mu\nu} = n^\nu K_{\mu\nu} = 0, \quad (2.51)$$

where n is the direction of the normal vector n^μ .

It is important to notice that in terms of the Lie Derivative, we can write the extrinsic curvature as

$$K_{\mu\nu} = -\frac{1}{2} \mathcal{L}_n \gamma_{\mu\nu}. \quad (2.52)$$

The extrinsic curvature, as a result of the decomposition, describes the relationship between the hypersurfaces and the 4D-spacetime around them. In fact, as we see from Eq. (2.49) the extrinsic curvature represents the variation of the normal vector n_μ to the hypersurface, calculated along the hypersurface itself.

For the following, is useful to define D_{ij} , which is simply the 3D covariant derivative, i.e. the one associated with the hypersurface metric γ_{ij} . With more generality, we can write

$$D_\mu \equiv P_\mu^\alpha \nabla_\alpha, \quad (2.53)$$

which also satisfies the metric compatibility condition

$$D_\alpha \gamma_{\mu\nu} = 0. \quad (2.54)$$

Now working out calculations and knowing that in the foliation's coordinates we can write

$$\mathcal{L}_t = \partial_t, \quad (2.55)$$

we get

$$\partial_t \gamma_{ij} = -2\alpha K_{ij} + D_i \beta_j + D_j \beta_i, \quad (2.56)$$

where we restricted directly to spatial components because all other vanish.

To finally obtain the full decomposition of the 4D-Riemann tensor, i.e. ${}^{(4)}R_{\alpha\beta\gamma\delta}$ we simply apply the projection operator multiple times. Skipping here the long calculations, we can report directly the final result, which is expressed respectively by the *Gauss-Codazzi equations* (2.57) and, for the first contracted form of, by the *Codazzi-Mainardi equations* (2.58)

$$P_\mu^\alpha P_\nu^\beta P_\sigma^\gamma P_\tau^\delta {}^{(4)}R_{\alpha\beta\gamma\delta} = {}^{(3)}R_{\mu\nu\sigma\tau} + K_{\mu\sigma} K_{\nu\tau} - K_{\mu\tau} K_{\nu\sigma}, \quad (2.57)$$

$$P_\mu^\alpha P_\nu^\beta P_\sigma^\gamma n^\delta {}^{(4)}R_{\alpha\beta\gamma\delta} = D_\nu K_{\mu\sigma} - D_\mu K_{\nu\sigma}. \quad (2.58)$$

2.2.3 Evolution equations

All the definitions above are necessary to write down a set of evolution equations which can be employed to numerically evolve different spacetime configurations. For the sake of the page-limit for this manuscript we direct the reader to Appendix B, where we describe the most important 3 + 1 formulations, in terms of evolution equations, both from a historical point of view and for the relevance in numerical schemes and codes, like the ones used for this work. In particular, we illustrate the following formalisms

- ADM formalism in Sec. B.1, the most important from a historical point of view, first introduced in Arnowitt et al., 1959 and then improved in York, 1979;
- BSSNOK formalism in Sec. B.2, collectively perfected by the work in Nakamura et al., 1987; Shibata et al., 1995; Baumgarte et al., 1998a;
- Z4 formulation in Sec. B.3, first proposed in Bona et al., 2003; Bona et al., 2004, and a relevant subsequent extension of the original formulation, i.e. Z4c (see Bernuzzi et al., 2010);

2.3 Gauge conditions

So far with our treatment of 3+1 decomposition, we are left to deal with four degrees of freedom, which do not have an effect on the value of physical observables and therefore are referred to as **Gauge conditions**. We in fact have to specify two conditions: one for the lapse function α , called **slicing condition** and one for the shift vector β^i , called **shift condition**. The basic rules in the choice of these conditions are the following:

- singularities of the spacetime should be avoided and any coordinate distortion that could arise should be counteracted;
- conditions should be expressed in a 3-covariant form, to be spatial-coordinates invariants;
- conditions should be well-behaved (mathematically) and should be computationally simple and cheap.

2.3.1 Slicing condition

Following the principles stated above, we want to choose a condition that allows us to deal with singularities smoothly. Examples of the most used slicing conditions are:

- **Geodesic slicing condition** from Hahn et al., 1964, i.e. $\alpha = 1$. The proper acceleration of the Eulerian observers vanishes but if the gravitational field is non-uniform, it allows different Eulerian observers to focus (i.e. crossing of paths). Our coordinate system loses then its bijection and a singularity arises.
- **Maximal slicing condition** from Lichnerowicz, 1944, i.e. $K = 0$ and $\partial_t K = 0$. For $K = 0$ the volume of the hypersurfaces is maximal with respect to small variations. It prevents the hypersurfaces from coming arbitrarily close to singularities and ensures that Eulerian observers will not focus.
- **Bona-Massò** family of slicing conditions from Bona et al., 1995, i.e.

$$\frac{d}{dt}\alpha = \partial_t\alpha - \mathcal{L}_{\beta}\alpha = -f(\alpha)\alpha^2(K - K(t=0)), \quad (2.59)$$

with $f(\alpha) > 0$, $\alpha = h(x^i) + \ln(\gamma^{k/2})$ and $h(x^i)$ is a positive, arbitrary time-independent function. Setting different values for f we obtain various types of slicings:

- $f = 1$, **Harmonic slicing**
- $f = k/\alpha$. **1+log slicing**

2.3.2 Shift conditions

To take care of the shift vector β^i now, we have to specify appropriate gauge conditions. As for slicing conditions, some of the most used shift conditions are the following:

- $\beta^i = 0$, one of the more simple and used conditions but which causes BH horizons to grow rapidly in coordinate space leading to the computational domains to fall inside the BH.
- **Minimal Distortion** shift condition, i.e.

$$\Delta_L \beta^i = 2D_j(\alpha B^{ij}), \quad (2.60)$$

where

$$\Delta_L \beta^i \equiv D_j(L\beta)^{ij} = D_i D^i \beta^i + \frac{1}{3} D^i D_j \beta^j + R_j^i \beta^j \quad (2.61)$$

is an elliptical shift condition that minimizes the integral of the *distortion tensor* over the spatial hypersurface with respect to the shift

- **Gamma-freezing** shift condition, i.e. $\partial_t \hat{\Gamma}^i = 0$ (where Γ is defined in Eq. (B.16)) proposed as a natural shift condition in context of BSSNOK formulation described in Sec. B.2, as it freezes three of the independent degrees of freedom.
- **Gamma driver** shift condition from Alcubierre et al., 2001, which is a reformulation of the Gamma-freezing shift condition for $\hat{\Gamma}^i$ and is expressed by:

$$\partial_t \beta^i - \beta^j \partial_j \beta^i = \frac{3}{4} B^i, \quad (2.62)$$

$$\partial_t B^i - \beta^j \partial_j B^i = \partial_t \hat{\Gamma}^i - \beta^j \partial_j \hat{\Gamma}^i - \eta B^i, \quad (2.63)$$

where B^i is an auxiliary variable and η is a damping term to avoid oscillations in the shift due to large variations of the gauges. They are extremely robust in BH simulations with puncture initial data (see Sec. 4.2.1), controlling both the slice stretching and the shear due to the rotation of the BH.

Chapter 3

General Relativistic Hydrodynamics

In chapter Ch. 2 we discussed how to decompose the spacetime in 3+1 dimensions and especially showed how this applies to the Einstein equations (2.26). In this chapter we continue the procedure to specify the source term in the previously mentioned equations, specifying the matter/energy contribution and to obtain a complete set of equations to evolve matter in a relativistic context.

The starting point is to specify an expression for the stress-energy tensor $T^{\mu\nu}$. First we need to expand the definition given in Eq. (2.23) of the stress-energy tensor itself. This tensor, as we see, is deeply related to the matter description. In fact considering a 4D-spacetime we can define the stress-energy tensor $T^{\mu\nu}$ (also called *energy-momentum tensor*) and interpret specific components in a physical way

$$T^{00} = \text{energy density}, \quad (3.1)$$

$$T^{0i} = \text{momentum density}, \quad (3.2)$$

$$T^{i0} = \text{energy flux}, \quad (3.3)$$

$$T^{ij} = \text{flux of } i \text{ momentum in direction } j. \quad (3.4)$$

From Eq. (2.24) we can also write our usual conservation laws for energy and momentum as:

$$\nabla_{\nu} T^{\mu\nu} = 0. \quad (3.5)$$

In fact, with $\mu = 0$ we get the energy conservation law, while for $\mu = i$ we get the momentum conservation law. In general these conservation laws only hold locally, since the gravitational field modifies the energy and momentum of the system.

3.1 General Relativistic HydroDynamics Equations (GRHD)

To specify the matter (or in general the energy content) of the spacetime, we need to specify the Lagrangian energy density \mathcal{L} in Eq. (2.23). We start from what we consider a good basic approximation, namely a perfect fluid approximation, for which, skipping the calculations, we obtain

$$T^{\mu\nu} = (\rho(1 + \epsilon) + p)u^\mu u^\nu - pg^{\mu\nu} = \rho h u^\mu u^\nu - pg^{\mu\nu}, \quad (3.6)$$

where h is the *specific enthalpy*, expressed by

$$h = 1 + \epsilon + \frac{p}{\rho}, \quad (3.7)$$

and where we simply assumed $T^{00} = \rho$, $T^{ii} = p$ and $T^{\mu\nu}$ which describes a fluid with rest mass energy density ρ , specific internal energy ϵ , pressure p , no heat conduction $T^{0i} = 0$ in the frame co-moving with the fluid whose 4-velocity is represented by u^μ , with the property $u^\mu u_\mu = 1$.

It is helpful to define the *rest-mass density current* $J_{(\rho)}^\mu$ as

$$J_{(\rho)}^\mu = \rho u^\mu. \quad (3.8)$$

Next step is to specify a set of conservation equations for the matter evolution. We are again using Eq. (3.5) for the conservation of energy and momentum and the continuity equation in the following, Eq. (3.10):

$$\nabla_\nu T^{\mu\nu} = 0, \quad (3.9)$$

$$\nabla_\mu J_{(\rho)}^\mu = \nabla_\mu (\rho u^\mu) = 0. \quad (3.10)$$

In the following we will describe the principal approaches to the numerical solution of these equations to obtain a complete description of matter evolution.

3.1.1 Wilson formulation

In the 1970s J.R. Wilson published an Eulerian formulation in Wilson., 1972, based on the introduction of the dynamical variables

$$D \equiv \rho u^0, \quad (3.11)$$

$$S_\mu \equiv \rho h u^0 u_\mu, \quad (3.12)$$

$$E \equiv \rho u^0 \epsilon, \quad (3.13)$$

that, as seen before, represent the rest mass density, the covariant momentum and the generalized internal energy density in the Eulerian frame (and for this are referred as *dynamical variables*).

Using these variables we can expand the set of Eq. (3.9) and Eq. (3.10) to obtain

$$\frac{1}{\sqrt{-g}} \partial_t (\sqrt{-g} D) + \frac{1}{\sqrt{-g}} \partial_i (\sqrt{-g} D V^i) = 0, \quad (3.14)$$

$$\frac{1}{\sqrt{-g}} \partial_t (\sqrt{-g} S_\mu) + \frac{1}{\sqrt{-g}} \partial_i (\sqrt{-g} S_\mu V^i) + \partial_\mu p + \frac{1}{2} (\partial_\mu g^{\alpha\beta}) \left(\frac{S_\alpha S_\beta}{S^0} \right) = 0, \quad (3.15)$$

$$\partial_t (\sqrt{-g} E) + \partial_i (\sqrt{-g} E V^i) + p \partial_\mu (\sqrt{-g} u^0 V^\mu) = 0, \quad (3.16)$$

with

$$V^\mu \equiv \frac{u^\mu}{u^0}, \quad (3.17)$$

that is the 4-velocity measured by an Eulerian observer or *transport velocity*.

The previous set of equations represents the **Wilson formulation** of relativistic hydrodynamics. To complete the system of equations we need to specify an equation of state of the type

$$P = \rho \epsilon (\gamma - 1), \quad (3.18)$$

with $\gamma = \text{const.}$

It can be easily shown that these equations are **not** written in a *conservative form* (see Appendix C), fundamental for numerical simulations, and hence require the use of a term of *artificial viscosity* which is added to the pressure and which acts in the same way as a physical bulk viscosity.

This method is proven effective if we are able to deal with the divergences that could arise with ultra-relativistic flows due to the nonlinear coupling between the artificial viscosity and the fluid velocity.

3.1.2 Valencia Formulation

In the 1990s a new Eulerian formulation of Relativistic HydroDynamics (RHD) was developed by the Spanish team of Martí, Ibáñez and Miralles and for that took the name of **Valencia formulation** (see Martí et al., 1991). Contrary to Wilson's formulation, the one described in the following can be proven to be *conservative*. In the following we show the equations written directly in general relativistic form (GRHD) employing a 3 + 1-decomposition.

Using the same procedure as in Sec. 3.1.1 we first define the conserved variables as

$$D \equiv \rho W, \quad (3.19)$$

$$S_\mu \equiv \rho h W^2 v_\mu, \quad (3.20)$$

$$S_{\mu\nu} \equiv \rho h W^2 v_\mu v_\nu + P \gamma_{\mu\nu}, \quad (3.21)$$

$$E \equiv \rho h W^2 - P, \quad (3.22)$$

where we defined the *Lorentz factor*

$$W \equiv -n_\mu u^\mu = \alpha u^0 = \frac{1}{\sqrt{1 - V^i V_i}}, \quad (3.23)$$

using the relations in Eq. (2.41), (2.42) and (3.17) and v^μ is part of the decomposition of the fluid 4-velocity u^μ in Eq. (3.26). With these definitions we can write the stress-energy tensor as

$$T^{\mu\nu} = \rho h u^\mu u^\nu + p g^{\mu\nu} = E n^\mu n^\nu + S^\mu n^\nu + S^\nu n^\mu = \quad (3.24)$$

$$= \rho h W (n^\mu + v^\mu)(n^\nu + v^\nu) + p(\gamma^{\mu\nu} + n^\mu n^\nu), \quad (3.25)$$

where we used the fact that

$$u^\mu = W(n^\mu + V^\mu). \quad (3.26)$$

We can now take, for example, Eq. (3.10) and write it as

$$\begin{aligned} \nabla_\mu(\rho u^\mu) &= \frac{1}{\sqrt{-g}} \partial_\mu(\sqrt{-g} \rho u^\mu) = \\ &= \frac{1}{\sqrt{-g}} [\partial_t(\sqrt{-g} \rho u^0) + \partial_i(\sqrt{-g} \rho u^i)] = 0. \end{aligned} \quad (3.27)$$

Using the definitions in Eq. (3.19), (3.17) and relation (2.41) we get the expression

$$\partial_t \left(\sqrt{\gamma} D \right) + \partial_i \left[\sqrt{\gamma} D (\alpha V^i - \beta^i) \right] = 0. \quad (3.28)$$

In the same way we obtain

$$\partial_t (\sqrt{\gamma} S_j) + \partial_i \left[\sqrt{\gamma} (\alpha S_j^i - \beta^i S_j) \right] = \frac{1}{2} \sqrt{-g} T^{\mu\nu} \partial_j g_{\mu\nu}, \quad (3.29)$$

and

$$\partial_t (\sqrt{\gamma} E) + \partial_i \left[\sqrt{\gamma} (\alpha S^i - \beta^i E) \right] = -\frac{1}{2} \sqrt{-g} T^{\mu\nu} \nabla_\mu n_\nu. \quad (3.30)$$

We can now glue together the previous expressions in a more compact form

$$\partial_t \left(\sqrt{\gamma} \vec{U} \right) + \partial_i \left(\sqrt{\gamma} (\vec{F})^i \right) = \vec{S}, \quad (3.31)$$

where we have defined the vectors

$$\vec{U} = (D; S_j; E)^T = (\rho W; \rho h W^2 V_j; \rho h W^2 - P)^T, \quad (3.32)$$

$$(\vec{F})^i = (\alpha V^i D - \beta^i D; \alpha S_j^i - \beta^i S_j; \alpha S^i - \beta^i E)^T, \quad (3.33)$$

$$\vec{S} = \sqrt{\gamma} \left(0; \frac{1}{2} \alpha S^{ik} \partial_j \gamma_{ik} + S_i \partial_j \beta^i - E \partial_j \alpha; \alpha S^{ij} K_{ij} - S^j \partial_j \alpha \right)^T. \quad (3.34)$$

Eq. (3.31) represents the set of PDE's describing GRHD in the *Valencia formulation*. Eq. (3.32)- (3.34) are valid in any curved spacetime written in any coordinate systems with ds of the form in Eq.(2.40).

Because linear combinations of conserved variables are still solutions to the equations in conservative form, the original formulation in Banyuls et al., 1997 used as conserved energy the quantity

$$\tau \equiv \rho W (hW - 1) - p = E - D, \quad (3.35)$$

which represents conserved energy. This choice has purely numerical motivations, i.e., the conservation of τ as a combination of two conserved quantities is more accurate than that of E only. Because of this it is the one employed in most numerical codes (see Baiotti et al., 2005).

Looking now at the source terms in Eq. (3.34) we can see that if we choose a set of Cartesian coordinates for a flat spacetime they vanish, leaving us with a set of homogeneous equations, since they do not contain derivatives of the fluid variables and are

therefore finite even in the presence of physical shocks. Finally the main procedure to be implemented in the code for the Valencia formulation is schematized this way:

Primitive var. \implies **Conserved var.** \implies **Evolution** \implies **Primitive var.**

Why are all these steps needed? The recovery of the primitive variables is not mathematically necessary, but it is fundamental in order to get a physical interpretation of the results and to interface the evolution equations with the microphysical description coming from the EoS (see Appendix D), which is naturally expressed in terms of the primitive variables. The conserved variables can be expressed in terms of the primitive variables in a straightforward manner but the opposite is not true and a root-finding procedure is needed to obtain the primitive variables from the conserved ones that have been evolved in time. This procedure is usually computationally expensive, and represents a source of numerical errors. For more details refer to Appendix E.

For the sake of completeness we analyze the eigenvalues of

$$(\vec{A})^i = \frac{\partial \sqrt{\gamma}(\vec{F})^i}{\partial \sqrt{\gamma}\vec{U}} = \frac{\partial (\vec{F})^i}{\partial \vec{U}}, \quad (3.36)$$

in relation to the expression in Eq. (3.31), needed for the treatment of fluxes in NR (to expand on this topic we refer to more extensive treatments of High Resolution Shock Capturing methods). in Shibata, 2015; Rezzolla et al., 2013) Taking $i = x$ the eigenvalues are

$$\lambda_0 = \alpha v^x - \beta^x, \quad (3.37)$$

$$\lambda_{\pm} = \frac{\alpha}{1 - v^2 c_s^2} - \left[v^x (1 - c_s^2) \pm \sqrt{(1 - v^2)[\gamma^{xx}(1 - v^2 c_s^2) - v^x v^x (1 - c_s^2)]} \right] \beta^x. \quad (3.38)$$

We note that the λ_0 eigenvalue is triple-degenerate.

From the eigenvalues λ_0, λ_{\pm} we can derive the right and left eigenvectors $\vec{R}^0, \vec{R}^{\pm}, \vec{L}^0, \vec{L}^{\pm}$. λ_{\pm} measure the propagation speed of the so called *acoustic waves* while λ_0 measure the propagation speed of the so called *matter waves* or *entropy waves*.

3.2 General Relativistic Magneto-HydroDynamics Equations (GRMHD)

With the formalism described up to now we haven't taken into account magnetic and electric fields. In the following we will describe a formalism which allows us to evolve hydrodynamics equations and Maxwell's equations. For this treatment we refer to Anton et al., 2006 and Giacomazzo et al., 2007. GRMHD formulation is widely known so one may refer to other works like Koide et al., 1999; Komissarov, 1999; McKinney et al., 2004; Duez et al., 2005; Shibata et al., 2005.

We first introduce the 4-vectors E^μ and B^μ , which represent respectively the *electric field* and the *magnetic field* which satisfy the relation

$$E^\mu n_\mu = B^\mu n_\mu = 0, \quad (3.39)$$

that implies that they are purely spatial vectors ($E^0 = B^0 = 0$). In terms of these newly introduced vectors we can write $F^{\mu\nu}$, the ElectroMagnetic (EM) anti-symmetric tensor field or *Faraday tensor*, as

$$F^{\mu\nu} = n^\mu E^\nu - n^\nu E^\mu + \varepsilon^{\mu\nu\tau} B_\tau, \quad (3.40)$$

with

$$\varepsilon_{\alpha\beta\gamma} = n^\delta \varepsilon_{\delta\alpha\beta\gamma}, \quad (3.41)$$

that is the 3D *Levi-Civita pseudo-tensor*, defined from the contraction of the 4D one. We remind that

$$\varepsilon_{ijk} = \sqrt{\gamma} e_{ijk}, \quad (3.42)$$

where e_{ijk} is the Levi-Civita pseudo-tensor in a flat spacetime.

We can also specify the relations

$$F^{\mu\nu} F_{\mu\nu} = 2(B^2 + E^2), \quad (3.43)$$

$${}^*F_{\mu\nu} F^{\mu\nu} = 4E^\mu B_\mu, \quad (3.44)$$

where ${}^*F_{\mu\nu}$ is $F_{\mu\nu}$'s dual.

Since we are adding another field to the domain we need to modify the source term of

Einstein equations (2.26), i.e. the stress-energy tensor, which can be written as

$$T_{\mu\nu} = T_{\mu\nu}^{HD} + T_{\mu\nu}^{EM}, \quad (3.45)$$

where $T_{\mu\nu}^{HD}$ is the hydrodynamic stress-energy tensor in Eq. (3.6)

$$T_{\mu\nu}^{EM} = F^{\mu\sigma} F_{\sigma\nu} - \frac{1}{4} g^{\mu\nu} F^{\sigma\tau} F_{\sigma\tau}. \quad (3.46)$$

To proceed we have to rewrite *Maxwell's equations* in terms of the quantities previously defined:

$$\nabla_{\nu} {}^*F^{\mu\nu} = \nabla_{\nu} \left(\frac{1}{2} \varepsilon^{\mu\nu\sigma\tau} F_{\sigma\tau} \right) = 0, \quad (3.47)$$

$$\nabla_{\nu} F^{\mu\nu} = 4\pi J^{\mu}, \quad (3.48)$$

with J^{μ} the charge-current 4-vector which can be expressed as

$$J^{\mu} = q u^{\mu} + \sigma F^{\mu\nu} u_{\nu}, \quad (3.49)$$

where q is the proper charge density, σ is the conductivity and u^{μ} the 4-velocity of the fluid.

If we assume that the fluid is a perfect conductor, i.e. $\sigma \rightarrow \infty$, and $F^{\mu\nu} u_{\nu} = 0$ (electric field measured by co-moving observers) we are in the *ideal magnetohydrodynamic regime* (IMHD). In this limit we can write the EM tensor in terms of magnetic field only as

$$F^{\mu\nu} = \eta^{\mu\nu\sigma\tau} b_{\sigma} u_{\tau}, \quad (3.50)$$

$${}^*F^{\mu\nu} = b^{\mu} u^{\nu} - b^{\nu} u^{\mu}, \quad (3.51)$$

and Maxwell equations as

$$\nabla_{\nu} {}^*F^{\mu\nu} = \frac{1}{\sqrt{-g}} \partial_{\nu} [\sqrt{-g} (b^{\mu} u^{\nu} - b^{\nu} u^{\mu})] = 0, \quad (3.52)$$

where b^{μ} is the magnetic field with respect to a co-moving observer, while, in the following, B^{μ} is the magnetic field with respect to an Eulerian observer. The relations

between b^μ and B^μ are

$$b^0 = \frac{WB^iV_i}{\alpha}, \quad (3.53)$$

$$b^i = \frac{B^i + \alpha b^0 u^i}{W}, \quad (3.54)$$

$$b^2 = b^\mu b_\mu = \frac{B^2 + \alpha^2 (b^0)^2}{W^2}, \quad (3.55)$$

where

$$B^2 = B^i B_i. \quad (3.56)$$

If we define

$$\hat{B}^k = \sqrt{\gamma} B^k, \quad (3.57)$$

we can divide Eq. (3.52) into components to get

$$\partial_i \hat{B}^i = \partial_i \sqrt{\gamma} B^i = 0, \quad (3.58)$$

$$\partial_t \hat{B}^i = \partial_j [(\alpha V^i - \beta^i) \hat{B}^j - (\alpha V^j - \beta^j) \hat{B}^i], \quad (3.59)$$

where Eq. (3.58) define the divergence-free constraint and Eq. (3.59) describe the evolution of the magnetic field.

Now passing to matter evolution we have to rewrite the stress-energy tensor to include magnetic energy density and pressure as

$$T^{\mu\nu} = (\rho h + b^2) u^\mu u^\nu + \left(p + \frac{b^2}{2} \right) g^{\mu\nu} - b^\mu b^\nu. \quad (3.60)$$

With this expression of $T^{\mu\nu}$ it is possible to write the GRMHD equation as in Eq. (3.31), given that we redefine \vec{F} , \vec{U} , \vec{S} and the conserved variables as

$$\begin{aligned} (\vec{F})^i = & \left(\frac{D\tilde{V}^i}{\alpha}; \frac{S_j \tilde{V}^i}{\alpha} + \left(p + \frac{b^2}{2} \right) \delta_j^i - \frac{b_j B^i}{W}; \frac{\tau \tilde{V}^i}{\alpha} + \right. \\ & \left. + \left(P + \frac{b^2}{2} \right) V^i - \frac{\alpha b^0 B^i}{W}; \frac{B^k \tilde{V}^i}{\alpha} - \frac{B^i \tilde{V}^k}{\alpha} \right)^T, \end{aligned} \quad (3.61)$$

$$\vec{U} = (D; S_j; \tau; B^k)^T, \quad (3.62)$$

$$\vec{S} = \left(0; T^{\mu\nu} (\partial_\mu g_{\nu j} - \Gamma_{\nu\mu}^\delta) \gamma_{\delta j}; \alpha (T^{\mu 0} \partial_\mu \ln(\alpha) - T^{\mu\nu} \Gamma_{\nu\mu}^0); 0; 0; 0 \right)^T, \quad (3.63)$$

with the definitions

$$D = \rho W, \quad (3.64)$$

$$S_j = (\rho h + b^2) W^2 V_j - \alpha b^0 b_j, \quad (3.65)$$

$$\tau = (\rho h + b^2) W^2 - \left(P + \frac{b^2}{2} \right) - \alpha (b^0)^2 - D. \quad (3.66)$$

In the expressions before we made use of the definition

$$\tilde{V}^i = \alpha V^i - \beta^i. \quad (3.67)$$

In ideal magnetohydrodynamics, there are in general seven independent characteristic speeds, if no degeneracy is present. This is in contrast to pure hydrodynamics, in which there are only three characteristic modes. Here we are presenting the eigenvalues modes. The eigenvectors can be derived by the same procedure as in the pure hydrodynamics case after an extremely lengthy calculation Anile, 1990; Komissarov, 1999; Anton et al., 2006. Showing details of this calculation is beyond the scope of this work.

Here we summarize the eigenvalues, first writing

$$\lambda_e = \alpha v^x - \beta^x, \quad (3.68)$$

$$\lambda_{\pm}^k = \frac{b^k \pm u^k \sqrt{4\pi\rho h + b^2}}{b^0 \pm u^0 \sqrt{4\pi\rho h + b^2}}, \quad (3.69)$$

which represent three different wave-speeds corresponding to the *entropy wave* (as in Eq. (3.37)) and the *Alfven waves*.

The remaining four solutions, which correspond to the *slow* and *fast* modes of *magnetohydrodynamics waves*, can be obtained by solving a fourth-order equation written as

$$(u^0)^4 (\lambda^k - v^k)^4 (1 - \zeta) + \left[c_s^2 \frac{(b^k - \lambda^k b^0)^2}{4\pi\rho h + b^2} - (u^0)^2 (\lambda^k - v^k)^2 \zeta \right] \times \left[\gamma^{xx} - \frac{(\beta^k + \lambda^k)^2}{\alpha^2} \right] = 0, \quad (3.70)$$

where v_A is the *Alfven velocity* defined as

$$\zeta \equiv \frac{4\pi\rho hc_s^2 + b^2}{4\pi\rho h + b^2} = v_A^2 + c_s^2 - v_A^2 c_s^2, \quad (3.71)$$

$$v_A^2 \equiv \frac{b^2}{4\pi\rho h + b^2}. \quad (3.72)$$

Let us note that the entropy waves and the Alfven waves appear as double roots. These superfluous eigenvalues appear associated with nonphysical waves and are the result of working with the unconstrained, 10×10 system of equations. Any attempt to develop a numerical procedure based on the wave structure of the GRMHD equations must remove these nonphysical waves (and the corresponding eigenvectors) from the wave decomposition.

This is necessary since degenerate states in which two or more wave speeds coincide, will break the strict hyperbolicity of the system. In the fluid rest frame, the degeneracy in both classical and relativistic MHD are the same: either the slow and Alfven waves have the same speed as the entropy wave when propagating perpendicularly to the magnetic field or the slow wave, the fast wave, or both have the same speed as the Alfven wave when propagating in a direction aligned with the magnetic field.

More details about the treatment of these eigenvalues can be found in BAM's GRMHD implementation discussed in Sec. 5.2. To summarize we can visualize the complete set of seven different speeds related to the eigenvalues in Fig. 3.1.

3.3 Radiative Transport and Microphysics

One of the aspects of simulations involving non-singular compact objects, is the additional complexity added by the matter treatment: simply put, when working with BHs we can treat them as stand-alone objects, basically neglecting whatever content may lie inside the EH (or, from a computational perspective, inside the AH). To the first degree of approximation, a simple but nonphysical treatment of the matter evolved in simulations, especially in the case of NSs, still allows substantial and meaningful results to be obtained (e.g. from the point of view of the gravitational signal and the GW emission). However, a rising interest in the past years has pushed simulations towards better and better descriptions of matter, allowing different properties to be accounted for, like the magnetic fields (MFs) treatment described in the previous sections. When focusing on systems like Core-Collapse Supernovae (CCSN) or the simulation of ejecta, in binary mergers we stress the importance of a better physical description in order to

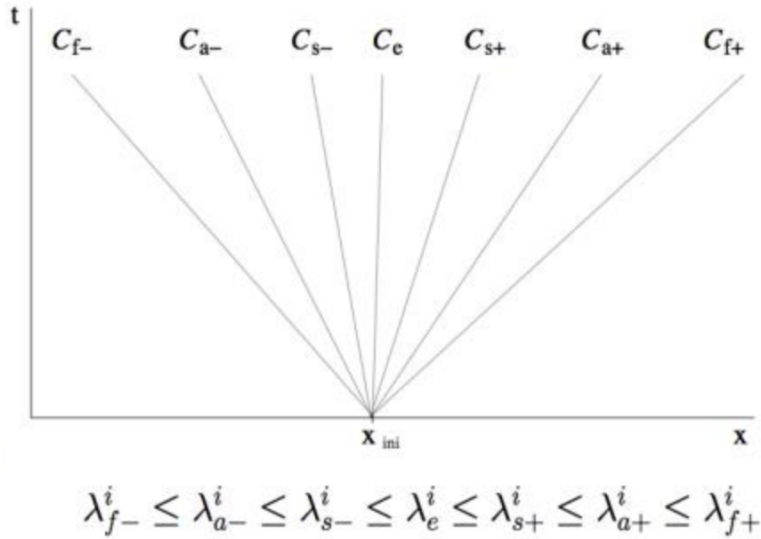


FIGURE 3.1: Complete set of eigenspeeds for the GRMHD formulation. The labels refer to, respectively, f = fast magneto-sonic waves, a = Alfvén waves, s = slow magneto-sonic waves, e = entropy or matter wave. For each set of waves the \pm propagation is shown.

From presentation *Towards relativistic magneto-rotational core collapse simulations* by T. Font

obtain results that align with currently available or future observations. Concretely, these phenomena derive from systems with high densities, $\rho \gtrsim 10^{14} \text{ g/cm}^3$, and high temperatures, $T \gtrsim 10 \text{ MeV}$. Generally in states with $\rho \gtrsim 10^{11} \text{ g/cm}^3$, the electron degeneracy pressure plays a major role in determining the total pressure and the neutron richness. In addition, with high-temperature $T \gtrsim$ a few MeV, the neutrino emission and neutrino transfer lead an important role, not only in cooling and heating, but also in determining the electron number density, thanks to electron and positron captures on nucleons and heavy nuclei. We then need to account for the evolution of the electron number density and the neutrino transfer processes for physically modeling high-density and high-temperature phenomena. Therefore, in addition to the continuity, Euler, and energy equations, we need to add to the system the *radiation transfer equation for neutrinos* and the *evolution equation for lepton number density*. Moreover, we need to provide a suitable EOS, that includes an appropriate microphysics description. Equations of state for high-density and high-temperature matter, which have been derived aiming primarily at the use for core-collapse supernova simulations, are usually constructed in a tabulated form (see Appendix D). Usually in tabulated EOS, the relevant thermodynamical quantities (i.e. pressure, internal energy, entropy, temperature, fractions of protons, neutrons, light nuclei, and heavy nuclei) are written as functions of the rest-mass density ρ , the temperature T and the electron fraction

per nucleon Y_e . In GRHD simulations, it is easy to derive the first two quantities from the simulation (assuming a correct choice of EOS), while we need to establish a way to calculate Y_e . Different methods can be used here. A simple way out is to assume, for example, β -equilibrium such as $p + e^- \leftrightarrow n + \nu_e$ and $n + e^+ \leftrightarrow p + \bar{\nu}_e$ but such conditions usually represents nonphysical scenarios. In general, we aim to write a set of evolution equations to solve numerically. We write, in the fluid rest frame

$$u^a \nabla_a Y_e = -\gamma_e, \quad (3.73)$$

where here γ_e is defined by the local capture rate of electrons by nuclei minus the local capture rate of positrons by nuclei. By some reworking, we get to the continuity-type equation

$$\partial_t(\rho^* Y_e) + \partial_k(\rho^* Y_e v^k) = -\rho \sqrt{-g} \gamma_e. \quad (3.74)$$

If we add to the system the fractions of neutrinos and total leptons, Y_ν and Y_l , we also have to solve their equivalent continuity-type equations of the type of Eq. (3.74).

We refer to more extensive works for ways to solve for Y_e , like Sekiguchi, 2010.

If we now address the radiation transfer equation for neutrinos ν_i the main approaches are the following:

1. **Boltzmann equation;**
2. **Leakage schemes;**
3. **Moment formalisms.**

For strictly handling radiation transfer effects, it is necessary to solve Boltzmann's equation numerically, taking into account absorption, emission, and scattering terms. This equation has a 3+3+1 dimensional form (3+1-spacetime dimensions + 3-momentum dimensions) so the computational domain has to cover a six-dimensional phase space. It is an extremely challenging task to perform a well-resolved numerical simulation with a sufficient grid resolution for this equation, unless a high spatial symmetry such as spherical symmetry is imposed. For this reason, adding such complexity to already computations-heavy simulations, could possibly increase n-fold the time required for a single run. Not to be carried away by the description we refer the reader to Mezzacappa et al., 1989; Liebendörfer et al., 2001; Liebendorfer et al., 2004 for basic formulations, Liebendörfer et al., 2001; Sumiyoshi et al., 2005 for results in spherically symmetric and general relativistic simulations and to Cardall et al., 2003;

Cardall et al., 2013; Shibata et al., 2014 for examples of attempts at including the full treatment on GRHD simulations.

It is now clear how approximate treatments are computationally favored in NR simulations, in the context of transport equation and neutrino treatment. A straightforward choice are **Leakage schemes**. In these schemes, equations for the radiation transfer are not essentially solved, but cooling (and heating in some cases) effects are phenomenologically taken into account. A leakage scheme uses the local properties of the fluid and an estimate of the neutrino optical depth to determine the amount of energy lost locally to neutrino-matter interactions, and the associated change in the composition of the fluid. Computational costs for a solution of radiation hydrodynamics by this scheme are less expensive than those by solving Boltzmann's equation or moment equations mentioned later. On top of this, it can still yield a semi-quantitative numerical result for radiation hydrodynamics that captures the essence of the radiation effects. We refer to van Riper et al., 1981; Epstein et al., 1981; Van Riper, 1982; Baron et al., 1985; Cooperstein, 1988; Ruffert et al., 1995; Rosswog et al., 2003; Sekiguchi, 2010; Sekiguchi, 2010 for first implementations of the scheme, as well as examples of applications for CCSN and BNS.

A more detailed approach is represented by Thorne's **Moment formalism**, first described in Thorne, 1981, and to a more modern version called **Truncated Moment Formalism** presented in Shibata et al., 2011. The formalism is based on the introduction of hierarchical equations for unprojected moments of massless particles associated with a moving medium. As pointed out in the original implementation, it is possible to choose any fiducial frame in the moment formalism. However, we have to keep in mind that for deriving a truncated moment formalism in a closed form, it is necessary to assume a closure relation that is determined by a physically reasonable assumption. This requires us to choose a good fiducial observer for deriving a useful truncated formalism from the moment formalism. In the dense medium, any radiation is strongly coupled to a fluid. This implies that in the 0th order, the radiation is in equilibrium with the medium, and radiation flow (measured by an observer co-moving with the fluid) is a small correction. The difficulty of this approach stands in describing the different behaviors in the *optically thick* region, the *optically thin* region, and in between these two (*gray* regimes). We can assume that the degree of anisotropy of the distribution function in the local rest frame is weak and that the distribution function is approximated by lower-order harmonics in the optically thick region. The radiation should propagate with the speed of light, while the radiation flow at each spacetime

point should be pointed primarily to a particular null direction (which is automatic in regions distant from sources). For optically grey regions, these two closure relations adopted for the two limiting cases are linked via the so-called **Eddington factor** (introduced in Levermore, 1984). On top of momentum formulations, other closures can be used like a *Monte-Carlo method* as in Foucart et al., 2018a.

For more details regarding neutrino transports, we refer to general reviews, like in Shibata, 2015.

An extended treatment of the subject of microphysics is beyond the scope of this work, but we refer to Appendix D for more details.

Chapter 4

Numerical Codes

The evolution of binary systems requires the design of ad hoc numerical codes that take care of designing the physical system and the subsequent evolution. These two aspects are treated separately with the employment of stand-alone codes for the computation of Initial Data (ID) and the actual evolution of binary systems and single stars. The theoretical basis on which the computation of Initial Data and the evolution of compact systems is based represent very complex aspects of NR and an accurate description of the topic would swerve from the aim of this work. For an in-depth take on these topics we point the reader to, for example, Alcubierre, 2008; Gourgoulhon, 2012 for an extensive description of the basis of Initial Data computation and to Tichy, 2016 for a review specific to the aforementioned topic. On the topic of the evolution of compact objects we recommend texts as Shibata, 2015; Rezzolla et al., 2013 for a general outlook on the methods employed by numerical codes.

In the following we are going to describe the numerical code used for computation of ID, used during this work (in Sec. 4.1) while in Sec. 4.2 we then describe BAM, the main evolution code used for this work, with its implementation and the developments added as a separate project (in Sec. 5.2).

4.1 Initial Data Codes

In the following we are going to briefly describe Initial Data codes relevant for the description of this project, i.e. **SGRID** in Sec. 4.1.1 and **Elliptica** in Sec. 4.1.2. Note that many different ID codes, both public and private, are available in the scientific panorama at the time of writing. Different codes employ different approaches and/or allow different settings for physical parameters. For the sake of completeness we mention some of the main codes used in numerical relativity: the **COCAL** code (Uryu et al., 2012; Tsokaros et al., 2015) for BBH and BNS initial data; the publicly available **FUKA**

code (Papenfort et al., 2021) for BBH, BNS, and BHNS binaries with aligned or anti-aligned spins; the public code `LORENE` (Lorene, n.d.; Grandclement, 2006; Taniguchi et al., 2006; Taniguchi et al., 2007; Taniguchi et al., 2008) for BBH, BHNS, and BNS, where only black holes can have spins that are aligned or anti-aligned; the `NRPyElliptic` code (Assumpcao et al., 2021) for BBHs; `SpECTRE`'s elliptic solver (Fischer et al., 2021a; Fischer et al., 2021b) for computing BBHs initial data; the private code `Spells` (Pfeiffer et al., 2003a; Foucart et al., 2008; Tacik et al., 2015; Tacik et al., 2016) for BBH, BNS, and BHNS binaries with arbitrary spin and asymmetric masses; and `TwoPunctures` (Ansorg et al., 2004; Ansorg, 2005; Khamesra et al., 2021) for BBHs and non-spinning BHNSs.

4.1.1 SGRID

We start presenting the **SGRID** code, a numerical code for NS initial data (in isolation or as binaries), used in particular to provide ID for the `BAM` code (see Sec. 4.2.1). The code was developed by W. Tichy in Tichy, 2009, Tichy, 2012 and Tichy et al., 2019 and has been upgraded over the years to include high arbitrary spins, high compactness, and high mass-ratios.

Here we described the main points of the formulations of the code and the numerical structure of the code itself. **SGRID** makes use of the **eXtended Conformal Thin Sandwich** method (XCTS) Pfeiffer et al., 2003b; York, 1999 which is an extension of the CTS method described in York, 1999. For a more extensive take on the subject refer again the reader to more extensive works as Cook, 2000, Tichy, 2016, Alcubierre, 2008, Gourgoulhon, 2012, and Baumgarte et al., 1998b.

We start by the choice of metric conformal decomposition. We then assume the binary to be in quasi-circular orbit and that the stars composing it are co-rotating. This implies the existence of an approximate helical Killing vector that in turn lets us assume that the time derivative of the conformal metric $\partial_t \bar{\gamma}^{ij}$ and the time derivative of the trace of the extrinsic curvature $\partial_t K$ vanish. We then choose maximal slicing and the conformal metric to be flat, i.e.

$$K = 0, \tag{4.1}$$

$$\bar{\gamma}_{ij} = \delta_{ij}. \tag{4.2}$$

We can then write

$$K^{ij} = \frac{1}{2\psi^4\alpha} (\bar{L}B)^{ij}. \tag{4.3}$$

We express the fluid 4-velocity u^μ in terms of the 3-velocity as

$${}^{(3)}u^i = h\gamma_\mu^i u^\mu, \quad (4.4)$$

that can be split in

$${}^{(3)}u^i = \nabla^i \phi + \omega^i, \quad (4.5)$$

with $\nabla^i \phi$ the irrotational part and ω^i the rotational part. This brings us to the set of equations

$$\bar{D}^2 \psi + \frac{\psi^5}{32\alpha^2} (\bar{L}B)^{ij} (\bar{L}B)_{ij} + 2\pi\psi^5 E = 0, \quad (4.6)$$

$$\bar{D}_j (\bar{L}B)^{ij} - (\bar{L}B)^{ij} \bar{D}_j \ln(\alpha\psi^{-6}) - 16\pi\alpha\psi^4 S^i = 0, \quad (4.7)$$

$$\bar{D}^2(\alpha\psi) - \alpha\psi \left[\frac{7\psi^4}{32\alpha^2} (\bar{L}B)^{ij} (\bar{L}B)_{ij} + 2\pi\psi^4 (E + 2S) \right] = 0, \quad (4.8)$$

$$\nabla_i \left[\frac{\rho_0 \alpha}{h} (\nabla^i \phi + \omega^i) - \rho \alpha u^0 (\beta^i + \xi^i) \right] = 0, \quad (4.9)$$

$$h = \sqrt{L^2 - (\nabla_i \phi + \omega_i)(\nabla^i \phi + \omega^i)}, \quad (4.10)$$

where we used the relations

$$(\bar{L}B)^{ij} = \bar{D}^i B^j + \bar{D}^j B^i - \frac{2}{3} \delta^{ij} \bar{D}_k B^k, \quad (4.11)$$

$$\bar{D}_i = \partial_i, \quad (4.12)$$

$$B^i = \beta^i + \Omega \varepsilon^{ij3} (x^j - x_{CM}^j), \quad (4.13)$$

$$u^0 = \frac{\sqrt{h^2 + (\nabla_i \phi + \omega_i)(\nabla^i \phi + \omega^i)}}{\alpha h}, \quad (4.14)$$

$$L^2 = \frac{b + \sqrt{b^2 - 4\alpha^4 [(\nabla_i \phi + \omega_i)\omega^i]^2}}{2\alpha^2}, \quad (4.15)$$

$$b = [(\xi^i + \beta^i) \nabla_i \phi - C]^2 + 2\alpha^2 (\nabla_i \phi + \omega_i) \omega^i, \quad (4.16)$$

and where C is a constant of integration that, in general, can have a different value inside each star, Ω is the angular velocity, and x_{CM}^i is the position of the center of mass.

The Boundary Conditions (BC)

$$\lim_{r \rightarrow \infty} \psi = 1, \quad (4.17)$$

$$\lim_{r \rightarrow \infty} B^i = 0, \quad (4.18)$$

$$\lim_{r \rightarrow \infty} \alpha\psi = 1, \quad (4.19)$$

at the spatial infinity, and

$$(\nabla^i \psi)(\nabla_i \rho) + \omega^i \nabla_i \rho = hu^0(\beta^i + \xi^i) \nabla_i \rho_0, \quad (4.20)$$

are imposed to close the system on the NS surface.

We now describe the numerical method used to solve the set of elliptic equations Eq. (4.6) - (4.9), together with the algebraic constraint Eq. (4.10). The motivation for the last constraint derives from the fact that the NS surface is not known a priori so we need a constraint to solve for its location.

There are two main ingredients of the code: its specific grid structure and the pseudo-spectral method used in the code.

The grid structure is shaped to take full advantage of the pseudo-spectral method, i.e. in such a way that the star surfaces are domain boundaries. However, when updating the matter distribution given by h within the iterative approach, the stars change shape; hence the domain boundaries have to be adjusted as well. In order to address this problem, the foliated hypersurface is covered by multiple domains, each described by its own coordinates. For the star domains, these coordinates depend on a freely specifiable function which will allow us to adapt the domain boundaries to the star surface. In the latest version of the code, *surface fitting* cubed sphere coordinates that have no singularities are used.

In Fig. 4.1 is shown how, in the case of a BNS, the stars are covered by a central cube surrounded by several cubed sphere wedges. The space around the stars is covered by additional domains. All domains together cover two cubes containing the stars and their surroundings. The cubes put next to each other are surrounded by wedges so as to cover a large sphere. This sphere can in turn be surrounded by additional shells.

As for the pseudo-spectral character, we use *Chebyshev expansions* and introduce grid

points at the Chebyshev extrema. Once the number of grid points is chosen, all derivatives are approximated by a linear combination of the field values at the grid points. Such a pseudo-spectral method is similar in spirit to finite differences, but it uses all grid points in one direction to approximate the corresponding derivative and is more accurate for smooth fields. Once all derivatives have been discretized in this way, we end up with a set of non-linear equations for all fields at all grid points.

The conformal factor ψ has to satisfy Eq. (4.6), but unfortunately, using the maximum principle in the Laplace equation for the NS mass, this equation is not guaranteed to have unique solutions. When this happens, the linear solver fails and one cannot find initial data. To solve this problem we modify it by introducing

$$\bar{E} \equiv \psi^8 E, \quad (4.21)$$

so that we get

$$\bar{D}^2 \psi + \frac{\psi^5}{32\alpha^2} (\bar{L}B)^{ij} (\bar{L}B)_{ij} + 2\pi\psi^{-3}\bar{E} = 0. \quad (4.22)$$

For challenging cases with high spins or high masses we find numerical problems close to the star surface arising from this equation. In these cases the first derivatives of ϕ can develop visible kinks just inside the star surface. We have found that we can smooth out these kinks by replacing Eq. (4.9) with

$$\begin{aligned} \frac{c(\rho_0)\alpha}{h} \phi^{-4} \partial^2 \phi + 2 \frac{\rho_0 \alpha}{h} \psi^{-5} (\partial_i \psi) (\partial^i \phi) + \left(\nabla_i \frac{\rho_0 \alpha}{h} \right) (\nabla^i \phi) + \\ + \nabla_i \left[\frac{\rho_0 \alpha}{h} \omega^i - \rho \alpha u^0 (\beta^i - \xi^i) \right] = 0, \end{aligned} \quad (4.23)$$

where we used the relation

$$c(\rho_0) = \rho_0 + \epsilon \rho_{0c} \left(\frac{\rho_{0c} - \rho_0}{\rho_{0c}} \right)^4, \quad (4.24)$$

which depends on ρ_{0c} , set to ρ_0 at the star center, and the free parameter ϵ .

It is helpful to specify, as an approximation, the formula for the irrotational velocity potential

$$\phi = \Omega (x_{C^*}^1 - x_{CM}^1) x^2, \quad (4.25)$$

where $x_{C^*}^1$ is the position of the star center and x_{CM}^1 is the position of the center of mass.

We can now summarize the procedure for the solution of the relevant elliptic equations:

1. Find an initial guess for h within each star \rightarrow Tolman-Oppenheimer-Volkoff (TOV) solution.
2. Choose ϕ as in Eq. (4.25).
3. **If** residual of Eq. (4.23) $>$ residual of Eq. (4.22) + Eq. (4.7) + Eq. (4.8) \rightarrow solve for ϕ .
4. Solve Eq. (4.22), Eq. (4.7) and Eq. (4.8) for (ψ, B^i, α) and update the old solution, using a relaxation scheme.
5. Solve Eq. (4.10) imposing $\partial_1 h|_{x_{C_{1,2}}^1} = 0$ and employ a root finder for Ω and $x_{CM}^1 \rightarrow$ **Force Balance method**.
6. Update h for each star and star boundaries.
7. Evaluate residual of left-hand side of Eq. (4.22), Eq. (4.7) and Eq. (4.8).
8. Keep star centers fixed by root finder for $\partial_i h = 0$ and translating h and other matter quantities.
9. Go back to step 3.

4.1.2 Elliptica

We now describe the `Elliptica` code, developed by A. Rashti and W. Tichy in Rashti et al., 2022. The code shares some key properties with the `SGRID` code, previously described, and extends its capabilities to mixed binaries of compact objects, i.e. Black Hole - Neutron Star binaries (BHNS). This ID code represents the basis for the setups used in this work.

`Elliptica`, much like `SGRID`, is a pseudo-spectral code that makes use of the coordinate sphere domain. The spectral decomposition is again done using Chebychev polynomials. In a similar way, the grid structure is based on Cartesian and cubed spherical coordinate systems (better illustrated in Fig. 4.2, for a BHNS system). Compared to `SGRID`, the grid structure shows additional splits in the outermost patches that increase the angular resolution at larger radii and result in avoiding interpolation for interface BCs. Novelty of the approach used to design this code span from the spectral decomposition of the Jacobian for a linearized set of elliptic PDEs to the use of a decomposition method on the domain just described.

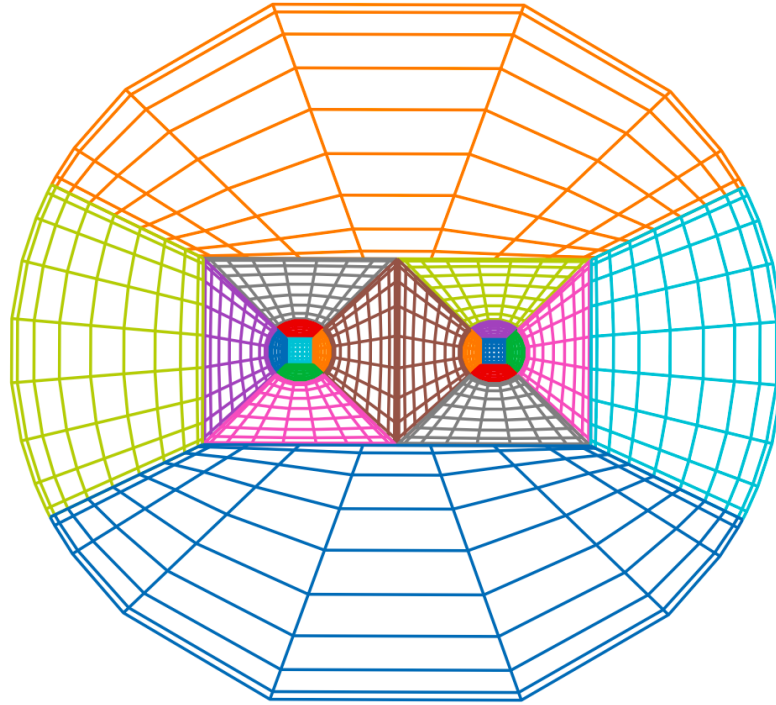


FIGURE 4.1: The domains in and around both stars in a BNS system. The result is a large sphere that covers both stars and the outside domain.

From Tichy et al., 2019

We start from a general decomposition in Chebychev polynomials of the problem $F_i(\vec{u}) = 0$, where we have discretized a PDE over N grid points, turning it into an algebraic equation for the field $u = u(x) \rightarrow \vec{u} = (u_0, \dots, u_{N-1})^T$. In this case we define the Jacobian matrix as

$$J_{ij} \equiv \frac{\delta F_i(\vec{u})}{\delta u_j} \quad (4.26)$$

Now we decompose using

$$T_i(X) = \cos(i \arccos(X)) \quad (4.27)$$

where $X = \frac{2x-(a+b)}{a-b}$ and $i = 0, 1, \dots, N-1$, so that we can expand the fields as

$$u_i = \sum_{n=0}^{N-1} \eta_n c_n T_n(X_i), \quad (4.28)$$

with

$$\eta_n = \begin{cases} 1, & \text{if } n = 0 \text{ or } n = N-1 \\ 2, & \text{otherwise} \end{cases} \quad (4.29)$$

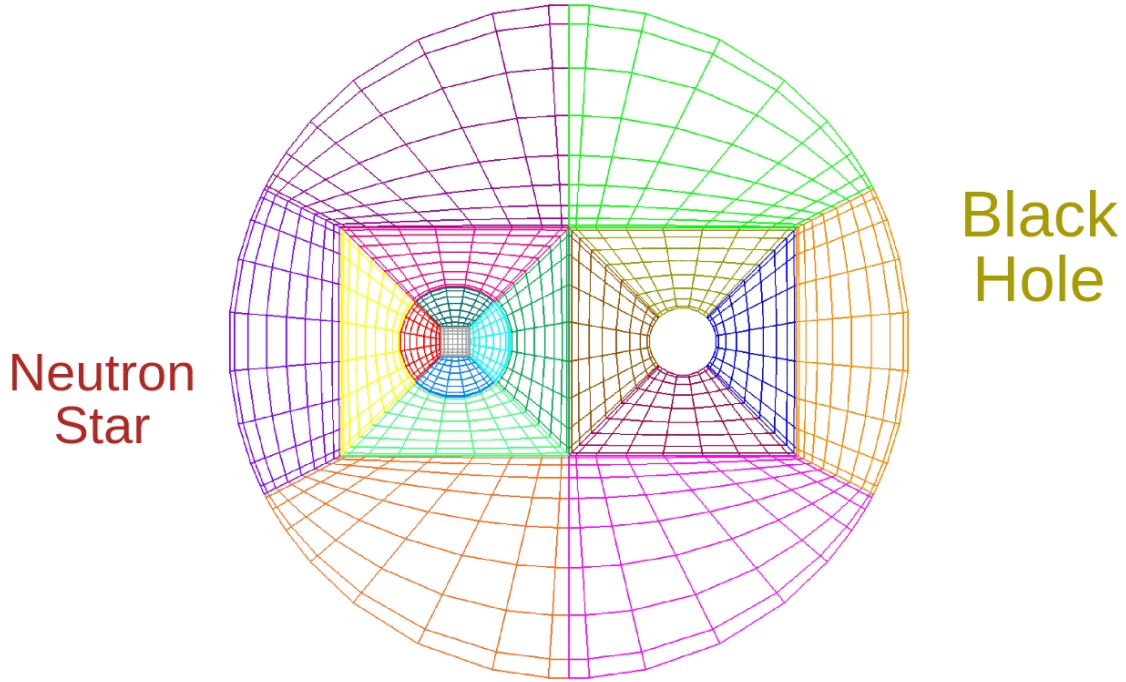


FIGURE 4.2: Example of a computational grid for a mixed binary system BHNS using cubed spherical coordinates. Shown is the intersection of the domains with the xy-plane

and

$$c_n = \frac{1}{2(N-1)} \sum_{k=0}^{N-1} \eta_k u_k T_k(X_n) \quad (4.30)$$

working out the calculations we obtain the full expansion of the Jacobian matrix:

$$J_{ij} = \frac{\eta_j}{2(N-1)} \left(\frac{dX}{dx} \right)^2 \times \left\{ \frac{\partial^2}{\partial X_i^2} \left(\frac{\sin((N - \frac{1}{2})(\theta_i + \theta_j))}{2 \sin(\frac{\theta_i + \theta_j}{2})} \right) + \frac{\partial^2}{\partial X_i^2} \left(\frac{\sin((N - \frac{1}{2})(\theta_i - \theta_j))}{2 \sin(\frac{\theta_i - \theta_j}{2})} \right) - (-1)^j \frac{d^2}{dX^2} T_{N-1}(X)|_{X=X_i} \right\}, \quad (4.31)$$

with $X_i = \cos(\theta_i)$. The advantage point of this expansion is that it only depends on the number of grid points, so the part of the matrix derived from derivative operators unchanged at each resolution. This permits to perform the calculation of the Jacobian only once per different resolution. Since `Elliptica` is based on an iterative scheme that gradually increases the resolution, although spending many iterations per resolution,

the use of such decomposition greatly speeds up the code's computations.

A Newton-Raphson root finder (see Burden, 2011; Taylor et al., 1987) is here employed to solve the equation

$$J\tilde{u} = F \quad (4.32)$$

with $u \rightarrow u + \tilde{u}$.

Another key feature of the code is the use of **Schur Complement Domain Decomposition** (SCDD) described in Saad, 2003. This method represents a *divide and conquer* approach for sparse matrices that fits the need of solving the elliptic equation on a domain subdivided into different patches. We recall from Appendix A that elliptic equations have a unique solution if appropriate boundary conditions (BCs) are imposed. Thus, attempting to solve these equations separately on each subdomain would lead to an under-determination of the system. Let's take the case in Fig. 4.3 as an example: to solve the equations in the two patches Ω_1 and Ω_2 we first need the boundary condition on Γ as well as for $\partial\Omega$. If we imagine extending this picture to the

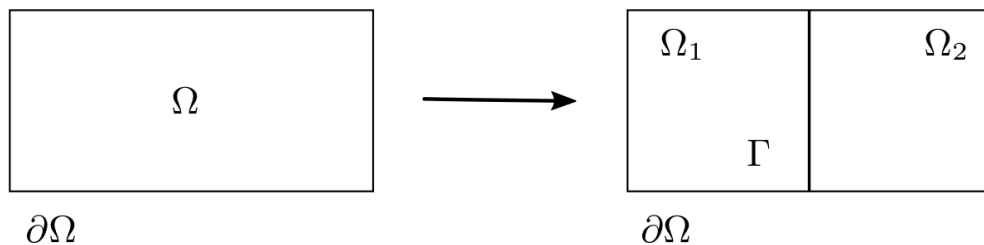


FIGURE 4.3: An example of a 2-dimensional grid Ω that is covered by two subdomains Ω_1 and Ω_2 with a common interface Γ .

From Rashti et al., 2022

full grid covering the domain we can see how, unless we are at the outer boundaries or at the innermost boundary, $\partial\Omega$ represent again different intra-patches borders like Γ . Following this idea, the elliptic PDEs are decoupled on all the patches covering the domain and the equations need to be solved first on every edge Γ between patches. In

Algorithm 1 Schur complement domain decomposition method.

- 1: Solve $BE' = E$ for E' ;
 - 2: Solve $Bf' = f$ for f' ;
 - 3: Compute $g' = g - Ff'$;
 - 4: Compute $S = (C - FE')$;
 - 5: Solve $S\tilde{w} = g'$ for \tilde{w} ;
 - 6: Compute $\tilde{v} = f' - E'\tilde{w}$;
-

subdomains.

- The Schur complement matrix consists of just couplings from the interfaces, thus its dimension is as big as the total number of points on all interfaces. From the comment before we see that such a matrix is sparse, hence the use of an efficient sparse solver is prompted.
- To invert B_p matrices and solve Eq. (4.38) the open-source Unsymmetric Multi-Frontal direct solver **UMFPACK** Davis, 2004 is used.

The general formalism of **Elliptica** includes the use of the *eXtended Conformal Thin Sandwich* method (XCTS) for the Einstein's equations (together with the ADM 3 + 1 formalism, see Sec. B.1), the same treatment of the fluid equations as in **SGRID** (see Sec. 4.1.1 and Tichy, 2012). On top of that, to treat the BH singularity, the excision approach described in Cook et al., 2004 is used: the BH singularity is excised from the computational domain, together with the spacetime included inside the Apparent Horizon (AH) of the BH, and suitable BCs are applied around the BH. The AH depends on the BCs chosen for the system.

It is worth mentioning that when an NS is present we introduced, in order to solve the fluid equations for an arbitrary spin, a purely spatial vector spin (to encapsulate the rotational part of the fluid) as in Tichy, 2012. In this manner we can decompose the rotational part of the fluid velocity ω^i from Eq. (4.5) as:

$$\omega^i = \epsilon_{ijk} \Omega_{\text{NS}}^j (x^k - \bar{x}_{\text{NS}}^k), \quad (4.39)$$

in which, \bar{x}_{NS}^k denotes the coordinate of NS's center and Ω_{NS}^j is a vector related to the spinning motion of the NS. An empirical relation between Ω_{NS}^j and the dimensionless spin of the NS χ_{NS}^i can be found and is here shown in Fig. 4.4

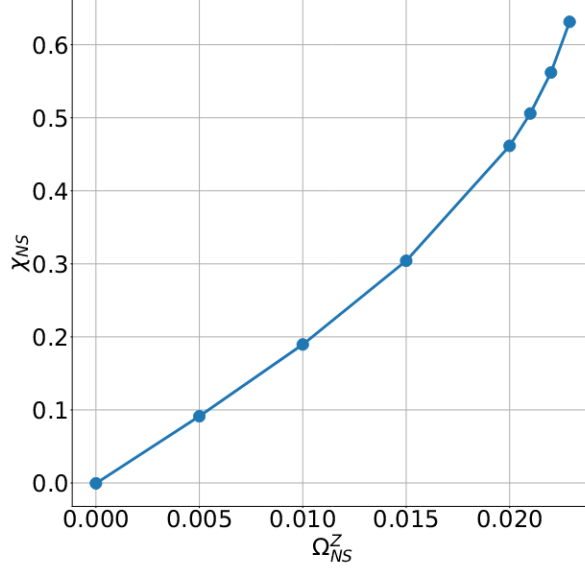


FIGURE 4.4: Dimensionless neutron star spin χ_{NS} as a function of spin-angular velocity parameter Ω_{NS}^z . Here, $\chi_{\text{BH}} = 0$, $M_{\text{irr}} = 5.2$, $M_{\text{B}} = 1.4$, and the EOS is polytropic with $K = 92.12$ and $\Gamma = 2$. The maximum χ_{NS} we can achieve is 0.63. The breakup spin for an NS is approximately 0.7 (see, e.g., Lo et al., 2011).

From Rashti et al., 2022

We now summarize the iterative scheme used by `Elliptica` for each resolution in a step-by-step style (for the case of a BHNS system). The workflow of the code is close to the one of `SGRID`. A direct comparison can be done just by referring to Sec. 4.1.1.

1. Solve the Elliptic PDEs.
2. Update the fields being solved using a relaxation scheme.
3. Adjust the BH angular velocity parameter Ω_{BH}^i and the BH radius.
4. Find Euler's equation constant C to fix the NS baryonic mass.
5. Adjust the system's center of mass \vec{r}_{CM} (ADM linear momenta $\rightarrow 0$).
6. Update the enthalpy with a relaxation method.
7. If desired, use the force balance to adjust the angular velocity of the system, Ω_{BHNS} .

8. Extrapolate matter fields to the outside of the NS.
9. Shift the matter to keep the NS's center fixed.
10. Find the new location of NS surface.
11. If needed, create a new grid and interpolate the values of the fields.

4.2 Evolution Codes

After finalizing the description of how ID are produced we are ready to evolve the physical system we have designed, simulating the behavior of the compact objects at exam. The evolution of spacetime domains, containing compact objects, has been studied extensively in the past fifty years. Many different numerical codes have been developed through the years to address this problem, each of them addressing or including different aspects of the matter at hand and/or different physical properties. For reference we list some of the most important evolution code in the literature: the `Einstein Toolkit` (see Brandt et al., 2021), a public modular code for the evolution of complex spacetimes; the `Spritz` code (see Cipolletta et al., 2020), successor of the `Whisky` code (see Giacomazzo et al., 2007), a public fully GRMHD code based on the Einstein Toolkit; the Spectral Einstein Code (`SpEC`), a flexible infrastructure for solving partial differential equations using multi-domain spectral methods (see Kidder et al., 2000); `WhiskyTHC`, a high-order finite-difference code for GRHD (see Radice et al., 2012). In the following we will focus on the description of the `BAM` code, listing the key feature of its implementation.

4.2.1 BAM

The main code on which this work is based in the numerical code Bifunctional Adaptive Mesh `BAM` developed in Jena by B. Brügmann and later refined also by collaborators in Brügmann, 1996; Brügmann, 1999; Brügmann et al., 2004; Brügmann et al., 2008; Thierfelder et al., 2011a; Dietrich et al., 2015. Originally the code was designed to simulate Binary Black Hole systems (BBH) but has evolved to include BNS and BHNS as well as single compact objects. The modular implementation allows different users to add their personal modules without affecting the general structure of the code, and to make use of a different combination of modules for a single run.

Grid Structure

The basic structure of the code employs a multi-grid box-in-box structure, together with a pseudo-adaptive mesh refinement functionality: the innermost boxes can be separated into smaller boxes that move together with the objects they contain. Contrary to a fully adaptive approach, the number of moving boxes and their resolutions are fixed at the beginning of the run. Cartesian coordinates map the whole domain and the grid is equispaced. A ratio $r = 2$ is imposed between spacings of consequent nested grids: starting from the coarsest box we half the spacing going to the first nested box while keeping the number of points constant. In general the spacing on level l , $dx_l = dx_{l-1}/2$. The time synchronization between levels is done using of *Berger-Oliger* time-stepping from Berger et al., 1984.

Puncture methods

One of the methods for handling BH singularities in evolution codes is the one of **punctures**. This method is widely used in BBH simulations and also simulations involving matter (like BNS and BHNS). It has been shown in fact in Baiotti et al., 2006; Thierfelder et al., 2011b that singularities produced by collapsing matter are naturally handled by the *puncture gauge* without particular treatment beyond standard artificial dissipation for the metric variables.

To define the concept we begin by imagining having to model N black-hole initial data. We adopt the *Brill-Lindquist* wormhole topology (described in Brill et al., 1963) with $N + 1$ asymptotically flat ends. The asymptotically flat ends are compactified and identified with points r_i on \mathbb{R}^3 . The coordinate singularities at the points r_i resulting from compactification are referred to as *punctures*.

Punctures have been developed in the context of initial data, as a treatment of the singularity in the constraint equations as in Dain, 2002. From a physical point of view, the puncture representation of BH ID is particularly appealing because it provides a simple prescription for associating masses, momenta, and spins with any number of black holes. More details about this method can be found in Eichler et al., 1997; Alcubierre et al., 2003; Baker et al., 2006; Campanelli et al., 2006; Gundlach et al., 2006; Battat et al., 2007.

AH finder

The natural choice for the surface of a BH would be to find the **Event Horizon** EH of the BH itself, which is defined as the boundary of the past of future null infinity (boundary of points from which a light ray can escape to infinity). From the definition, it is evident that we would need to integrate for the entirety of the simulation time to get the exact solution. This, of course contrasts with the idea of numerical evolution. It is then preferred numerically to instead look for an **Apparent Horizon** (AH). To define the latter, we first need to introduce *marginally outer trapped surfaces* (MOTS), i.e. smooth closed 2-surfaces whose future-pointing outgoing null geodesics have zero expansion. An apparent horizon is then defined as a MOTS not contained in any other MOTS. An AH is defined locally in time, in a spacelike slice, and depends only on data in that slice. Hence it can be (and usually is) found during the numerical computation. The apparent horizon finder implemented in BAM follows mainly the route of Gundlach, 1998 and Alcubierre et al., 2000.

Overview

Thanks to the definitions in the previous chapters we can summarize BAM's different aspects by pointing to the specific sections:

- **Metric:** BAM allows for either BSSNOK (see Sec. B.2) or Z4c (evolution of the Z4 formulation described in Sec. B.3 introduced in Bernuzzi et al., 2010 and then developed in Ruiz et al., 2011; Weyhausen et al., 2012; Cao et al., 2012; Hilditch et al., 2013) metric formulations to be used in simulations.
- **Gauges:** different gauge choices are allowed as described in Sec. 2.3.
- **Hydro:** matter treatment follows Valencia formulation of GRHD in Sec. 3.1.2.
- **EOS:** ideal gas EOS, polytropes and piecewise-polytropes (see Appendix D) can be adopted by fixing the needed parameters, as well as tabulated EOS.
- **Time Evolution:** different types of Runge-Kutta schemes can be used. (see Runge, 1895; Kutta, 1901 for the original formulation or Shu et al., 1988 for a modern, high-order formulation) as well as the classic Euler time-step.
- **HRSC scheme:** a hand-full of High Resolution Shock Capturing schemes are available in the code (see Shibata, 2015; Rezzolla et al., 2013 for more details), depending on the problem at hand.

- **Con2Prim**: recovery of primitive variables follows the procedure described in Appendix E.
- **Black Hole**: BH are approximated via the puncture treatment described before in Sec. 4.2.1 together with the AH finder described in 4.2.1.
- **ID**: BAM is capable of evolving ID constructed with different ID codes (mainly *SGRID* in Sec. 4.1.1 and *Elliptica* in Sec. 4.1.2). Since different approaches and formulations are used in ID codes with respect to general evolution codes we need to interface ID with BAM's infrastructure (see Sec. 4.2.1).
- **Atmosphere**: an atmosphere treatment is implemented, following Font et al., 2002; Baiotti et al., 2005. A vacuum implementation has also been developed but is still under study (see Poudel et al., 2020).

ID interface

As mentioned before it is necessary to adapt the ID calculated in any ID code to the structure of BAM. Depending on the different ID codes the strategy and the requirements to prepare the data for evolution may vary. In the following, we summarize the procedure used to initialize ID computed with *Elliptica*.

1. in *Elliptica* fields are the same as variables in BAM.
2. *Elliptica* uses a co-rotating frame, so we need a map to obtain a frame that asymptotically behaves like an inertial frame.
3. BH in *Elliptica* are excised while BAM adopts the moving puncture formalism detailed before: we need to fill the interior of the BH accordingly.
4. As for point 3. we need to specify the gauge choices for α and β so that the previously excised region of the BH morphs into a puncture in the first few iterations of the evolution code.

Chapter 5

Results

This chapter is dedicated to describing the results in the context of this thesis work. The different sections of the chapter, although not always related, outline the different projects and contributions of the author. Each individual section point to the respective theoretical description in the preceding chapters. More specifically in Sec. 5.1, we describe the study of the thermodynamics conditions leading to the decoupling of different neutrino species ν_i in BNS merger remnants, from Endrizzi et al., 2020; in Sec. 5.2 we outline the efforts done into implementing the first version of a GRMHD formulation in the `BAM` code. Finally, in Sec. 5.3 we go through the work in the context of mixed binary systems (BHNS), following the development of the `Elliptica` code, and that contributed to Rashti et al., 2022, and the most recent results of a follow-up project on the subject.

5.1 Neutrinospheres

A rising interest in the context of NR simulations is put into the study of elements formation and ejecta during the inspiral phase, but mainly in the post-merger phase and the subsequent remnant evolution. In general, the remnant is composed of a central dense object surrounded by a massive disk. While simulating BNS or BHNS system we can point out that irrespective of the nature of the central object, matter description plays a key role in the resolution of the physical phenomena that follow the merger. In particular, the neutron-richness of the ejecta allows for the rapid synthesis of heavy elements via neutron capture (the so-called *r-processes*, where *r* stands for *rapid*) whose following radioactive decay creates the peculiar signal, spanning different EM bands, that has been called *Kilonova signal* (for more details refer to Li et al., 1998; Kulkarni, 2005; Metzger, 2017). This connects to the early theory regarding BNS mergers being candidates for the emission of fast and bright gamma-ray

bursts, called Short Gamma-ray Bursts (SGRB), recently confirmed by the detection of GW170817 (see Abbott et al., 2017a). The Kilonova emission is characterized by an early UV+visible emission, moving to the Near Infra-Red (NIR) as time passes. The early emission could be linked to low photon opacity in specific matter regions which, in turn, could depend on the prominent contribution by neutrino radiation. Also if the effect is such that the electron fraction $Y_e \geq 0.25$ we can have suppression of some r-process' peaks. Neutrinos are, in fact, produced in large numbers, thanks to the high temperatures reached by matter during the merger (~ 100 MeV Perego et al., 2019) and the high densities $\rho \geq 10^{12}$ g/cm³ contributes to the formation of trapped neutrino regions, in equilibrium with the plasma. When densities decrease to $\rho \sim 10^{11}$ g/cm³ or lower, the radiation decouples from the matter and streams out.

Even if free streaming neutrinos are still able to transfer energy to a low-density region of the expanding ejecta's matter it is still important to identify the regions where this decoupling occurs (usually called **Neutrinospheres**). We can also define another type of neutrinosphere which describes the region in which neutrino radiation decouples from the background medium, i.e. weak and thermal equilibrium freezes out, due to the gradual decrease of the effectiveness of absorption and inelastic scattering. We label these surfaces as **diffusion surfaces** (the former) and **equilibrium surfaces** (the latter). Between these two surfaces, neutrinos are still able to diffuse, thanks to the quasi-elastic scattering of baryons. The location of these surfaces strongly depends on the neutrino species and their energy.

In this work, we present a quantitative post-processing method to identify different types of neutrinospheres in the post-merger phase of BNS simulations. A key feature of the analysis is the evaluation of the optical depth of neutrinos at any point of the domain. The optical depth τ represents the average number of interactions that radiation particles experience along a given path γ . In formulas, we can write

$$\tau_{\gamma:A \rightarrow B} = \int_{\gamma:A \rightarrow B} \kappa(s) ds, \quad (5.1)$$

where $\kappa(s)$ is the **opacity** (which corresponds to the inverse of the local mean free path) and $ds = g_{ij} dx^i dx^j$ is an infinitesimal displacement along the chosen path.

To evaluate this integral we need to think about the behavior of radiation, in particular neutrino radiation, passing from high-density to low-density regions. Although radiation is often produced isotropically, interaction with matter can affect its propagation, especially in regions where the mean free path is shorter.

To study the global behavior of neutrino radiation we adopt a more statistical approach. We also identify any point of the domain as the starting point A of the path γ , while B represents now all the points lying on the domain's outer boundaries. Among all the possible paths connecting A to the boundary B , the most likely ways for radiation to escape are the paths that minimize the optical depth, i.e.

$$\tau(x) = \min_{\gamma|\gamma:x \rightarrow x_b} \int_{\gamma} \kappa(s) ds, \quad (5.2)$$

where x is any point inside the domain and x_b is any point of the boundary from which radiation escapes freely. The surface where radiation decouples from matter is defined as the region where $\tau \sim 1$ and it is referred to as the neutrino surface. If its curvature is not very pronounced, the Eddington approximation applies and a neutrino surface is often referred to as the surface where $\tau = 2/3$.

The best practice to calculate the optical depths in Eq. (5.2) numerically would be to evaluate the discretized path that minimized the summation of the opacities towards the boundary. Clearly, such a path depends on the physical characteristic of the region traversed at a given time and will not be a straight line. A post-processing code like MODA, described in Perego et al., 2014b, makes use of this exact approach, evaluating all the possible paths possible for the evaluation of the optical depth. As expected, this approach, although more precise, is computationally expensive. The scheme we developed instead, being focused on a faster evaluation of the neutrinospheres, chooses 17 directions, corresponding to 5 on-axis directions

$$x^+, x^-, y^+, y^-, z^+,$$

(we disregard all z - directions since all simulations considered in this work are performed using a reflection symmetry along the z -axis), 8 planar diagonals

$$x^+y^+, x^+y^-, x^-y^+, x^-y^-, x^+z^+, x^-z^+, y^+z^+, y^-z^+,$$

and 4 full diagonals

$$x^+y^+z^+, x^+y^-z^+, x^-y^+z^+, x^-y^-z^+.$$

A representation of the directions in a Cartesian grid is given by Fig. 5.1. This common approach to effectively evaluate the optical depth, selecting a certain number of directions moving away from the point has been already used in the past for Newtonian simulations, using cylindrical coordinates and from 3 to 7 directions (see e.g., Rosswog

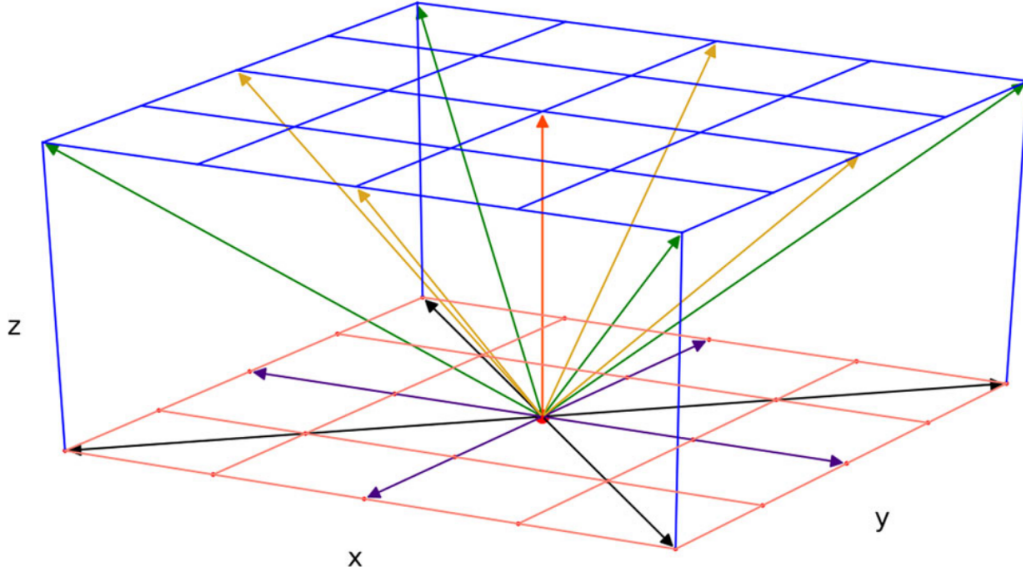


FIGURE 5.1: Visual representation of the 17 direction chosen for the evaluation of the optical depth, relative to any domain inner points, here a the center of the representation.
From Endrizzi et al., 2020

et al., 2003; Perego et al., 2014a). Our method represents an extension of this approach (making, in total, more directions per single point) although maintaining a low computational cost. This is done by reducing the analyzed region to a smaller volume centered around the remnant, where we expect to find the neutrino surfaces. This is supported by the fact that the contribution to the optical depth given by very low-density matter, usually found further away from the remnant, is negligible. In order to select this region, we define the characteristic length of the system l_C as $l_C = 5r_{11}$, with r_{11} being the average radius of a density isosurface at $\rho_{th} = 2 \times 10^{11} g/cm^3$. In the simulations presented in this work $r_{11} \sim 30 km$. To test our approximation, we have computed τ with $l_C = 5 r_{11}, 6 r_{11}, 8 r_{11}$ for a few selected cases, without finding significant differences in the thermodynamic properties of the decoupling region.

To calculate neutrino opacities it is necessary to account for the neutrino flavors (in this work we consider only 3 species, i.e. electron neutrinos ν_e , electron antineutrinos $\bar{\nu}_e$ and a collection of the remaining flavors, muon (anti)neutrinos ν_μ and tau (anti)neutrinos ν_τ in a single species ν_x), the matter properties (described by the EOS) and neutrino energies. The relevant neutrino-matter reactions considered in this work are listed in Table 5.1. Since we aim to identify two different types of neutrinospheres,

TABLE 5.1: Weak reactions providing the neutrino opacities used in this work and references for their implementation. $\nu \in \{\nu_e, \bar{\nu}_e, \nu_x\}$ denotes a neutrino species with ν_x referring to any heavy-lepton neutrino species. $N \in \{n, p\}$ denotes a nucleon, A a generic nucleus (including α particles), e^\pm electrons and positrons.

Reaction	Ref.
$\nu_e + n \rightarrow p + e^-$	Burrows et al., 2006; Horowitz, 2002
$\bar{\nu}_e + p \rightarrow n + e^+$	Burrows et al., 2006; Horowitz, 2002
$\nu + \bar{\nu} \rightarrow e^+ + e^-$	Bruenn, 1985; Mezzacappa et al., 1993
$N + N + \nu + \bar{\nu} \rightarrow N + N$	Hannestad et al., 1998
$\nu + N \rightarrow \nu + N$	Burrows et al., 2006
$\nu + A \rightarrow \nu + A$	Burrows et al., 2006

we divide the calculation of opacities in κ_{diff} and κ_{eq} , using the formulas

$$\kappa_{\text{diff}} = \sum_r \kappa_{ab,r} + \sum_r \kappa_{sc,s}, \quad (5.3)$$

$$\kappa_{eq} = \sqrt{\left(\sum_r \kappa_{ab,r}\right) \kappa_{\text{diff}}}, \quad (5.4)$$

where the indices r and s run over all the considered absorption ab and scattering sc reactions, respectively. Since only a subset of reactions are effective in keeping the neutrino field in thermal and weak equilibrium with the plasma, we defined the equilibrium opacity as the geometrical mean between the diffusion opacity and the opacity only due to absorption processes (see Shapiro et al., 1983; Raffelt, 2001 for analogous expressions).

Since to calculate κ_{eq} we use a subset of the interaction described in Table 5.1, it is always true that $\kappa_{\text{diff}} \geq \kappa_{eq}$ so equilibrium surfaces are inside of diffusion ones.

For the simulations performed in this work we made use of the `WhiskyTHC` code described in Radice et al., 2012 complemented by a leakage scheme to account for compositional and energy changes in the matter due to weak reactions involving ν_e , $\bar{\nu}_e$, and ν_x . Free-streaming neutrinos are emitted at average energy and then evolved according to the M0 scheme introduced in Radice et al., 2016; Radice et al., 2018. The post-processing tool developed here is also effective for simulations performed with an energy integrated (*gray*) M1 scheme, as in Foucart et al., 2016; Foucart et al., 2015. For a brief introduction about the schemes for the radiative transport of neutrinos

mentioned before, we point the reader to Sec. 3.3.

The initial data were computed with the `LORENE` code and evolved using two different EOS, i.e. DD2 introduced in Typel et al., 2010; Hempel et al., 2010 and SLy, introduced in Schneider et al., 2017. Neutrino opacities have a significant dependence on the energy of the incoming neutrino. Numerical simulations of BNS mergers including neutrino radiation provide values for the average energies of the neutrinos escaping to infinity. Despite the large variety of approximated schemes employed in these analyses, reported values usually agree within 10 – 20% as in e.g. Foucart et al., 2015; Perego et al., 2016; Foucart et al., 2016.

The approaches followed in this work are then the following. We determine the thermodynamic conditions of matter (density, temperature, and electron fraction) at the neutrino surfaces and use them to characterize the typical conditions at which the largest fraction of neutrinos decouples from matter. In our discretized domain, we identify the neutrino surface as the region where $0.5 \leq \tau \leq 0.85$. For each extracted quantity q we compute the volumetric mean q_{mean} and to give an estimate of its distribution around the mean value we compute the corresponding standard deviation as:

- we fix the neutrino energies to the following set of values compatible with the cited results, with the assumption that neutrino spectrum at infinity is mainly determined by the spectrum emerging from the neutrino surfaces: $\langle E_{\nu_e} \rangle \approx 9.34$ MeV, $\langle E_{\bar{\nu}_e} \rangle \approx 15.16$ MeV, and $\langle E_{\nu_x} \rangle \approx 23.98$ MeV;
- we compute optical depths and neutrino surfaces for a large set of neutrino energies spanning in the range 3 – 88.67 MeV;
- we compute optical depths using energy integrated opacities, assuming the distribution of neutrinos coupled to matter in weak and thermal equilibrium follows

$$f_\nu(E_\nu) = \left(e^{(E_\nu - \mu_\nu)/k_b T} \right), \quad (5.5)$$

which is a *Fermi-Dirac* distribution with E_ν the neutrino energy, μ_ν the neutrino chemical potential, k_b the Boltzmann constant and T the temperature of the fluid at the absorption/scattering point. Chemical potentials at equilibrium are taken

as

$$\mu_{\nu_e} = \mu_p + \mu_e - \mu_n, \quad (5.6)$$

$$\mu_{\bar{\nu}_e} = -\mu_{\nu_e}, \quad (5.7)$$

$$\mu_{\nu_x} = 0, \quad (5.8)$$

where μ_p , μ_e and μ_n are the relativistic proton, electron and neutron chemical potentials. Finally the spectrum averaged opacity is defined as:

$$\tilde{\kappa}_\nu = \frac{\int_0^\infty f_\nu(E) \kappa_\nu(E) E^2 dE}{\int_0^\infty f_\nu(E) E^2 dE}, \quad (5.9)$$

which accounts for neutrinos at equilibrium, diffusing from optically thick to optically thin regions, so more in line for the calculation of τ_{eq} .

In the following we summarize the results obtained showing as examples the diffusion and equilibrium surfaces calculated for the DD2 EOS model in Fig. 5.2 and Fig. 5.3, as well as the equilibrium and diffusion optical depths in Fig. 5.4 and Fig. 5.5. In short, we observed that the rest mass density and the neutrino energies are the most relevant quantities in determining the location of the decoupling surfaces and, consequently, the relevant thermodynamical conditions at decoupling for ν_e and $\bar{\nu}_e$, thanks to the dominant role of quasi-elastic scattering and charged-current absorption reactions on free nucleons. For heavy-flavor neutrinos, weak and thermal equilibrium is guaranteed by pair processes, like inverse nucleon-nucleon bremsstrahlung and $\nu - \bar{\nu}$ annihilation. Due to the strong dependence of the target and incident particle densities on matter temperature, the latter becomes a relevant thermodynamic quantity as well.

The diffusion decoupling surfaces of mean energy neutrinos are characterized by similar conditions among the different neutrino species in all the models, as a consequence of a compensation effect between the larger mean energy associated with heavy-flavor neutrinos ($k_{\text{scat}} \propto E_\nu^2$) and the larger abundance of absorbing neutrons relevant for ν_e . Temperatures can significantly differ based on the properties of the underlying nuclear EOS: softer EOSs, like SLy4, produce hotter remnants than stiffer ones, like DD2. For SLy the transition from diffusion to free-streaming regimes for mean energy neutrinos happens between 4 and 5 MeV, while for DD2 it happens between 3 and 4 MeV.

For equilibrium surfaces for mean energy neutrinos, we have, on the one hand, that thermodynamics conditions at the equilibrium and diffusion surfaces are very close for the ν_e . On the other hand, the relatively less favorable proton-absorption moves

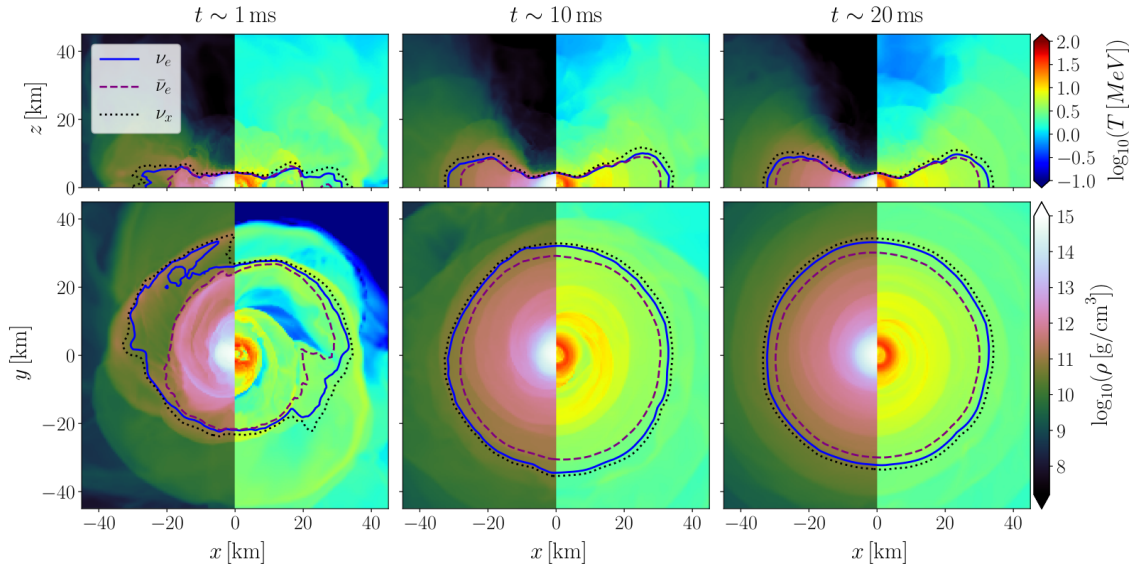


FIGURE 5.2: Evolution of diffusion neutrino surfaces for the mean neutrino energies at different stages of the post-merger of the DD2 model. The color map represents rest mass density (left side) and temperature (right side) in logarithmic scale in both meridional (top row) and equatorial (bottom row) plane. The three snapshots are taken at the closest iteration to, respectively, 1 (left column), 10 (middle column) and 20 (right column) ms after merger. Diffusion surfaces for neutrinos of the three considered species are highlighted by solid blue (ν_e), dashed magenta ($\bar{\nu}_e$) and dotted black (ν_x) contours.

From Endrizzi et al., 2020

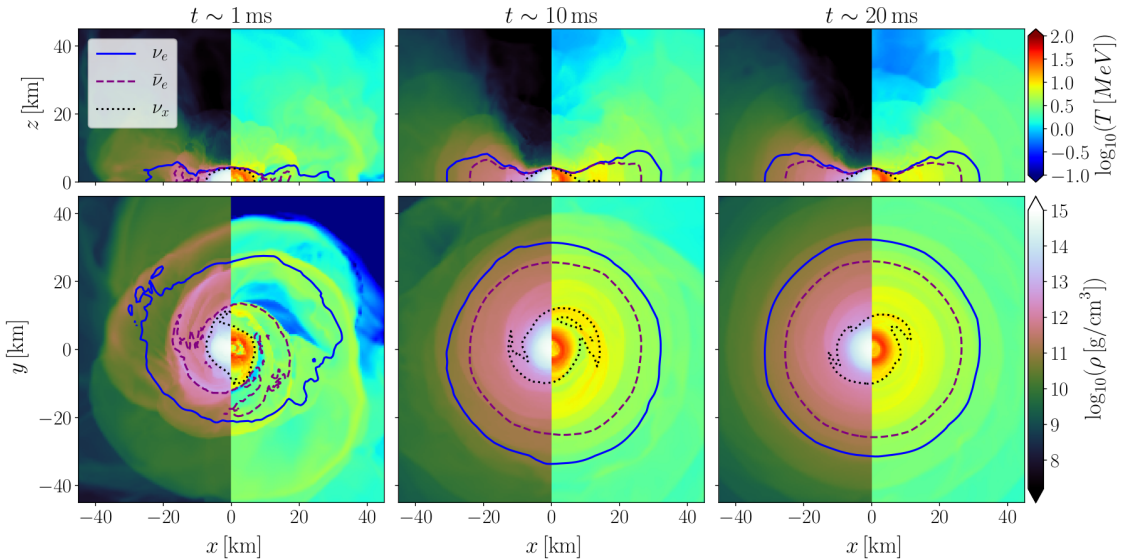


FIGURE 5.3: Same as Fig. 5.2 for the equilibrium neutrino surfaces for the mean neutrino energies at different stages of the post-merger of the DD2 model. From Endrizzi et al., 2020

the equilibrium surfaces of the $\bar{\nu}_e$ deeper inside the remnant. Consequently, the $\bar{\nu}_e$ equilibrium decoupling temperature increases to 5 MeV in the DD2 case and to 6 MeV in the SLy4 case. For heavy-flavor neutrinos, matter temperature becomes the most relevant quantity and the equilibrium decoupling happens around 10 MeV.

Our results for the equilibrium decoupling temperatures broadly satisfy the expected *blackbody* emission relation, i.e. $E_\nu \sim 3.15T$, with a closing agreement in the case of the stiff EOS model DD2. Deviations from it largely depend on the neutrino emission coming from the volume outside the neutrino surfaces (which is in fact more relevant for hotter remnants). We also notice that in the case of softer EOS differences between ν_e and $\bar{\nu}_e$ equilibrium decoupling temperatures reduce (as reported in Sekiguchi et al., 2016).

While considering neutrinos with energies between 3 and 88 MeV (i.e. covering the most relevant part of the emitted spectrum), we found that due to the strong dependence on E_ν of all cross-sections, such a large energy range translates into broad ranges of decoupling radii and thermodynamic conditions. The corresponding decoupling temperatures cover one order of magnitude, moving from ~ 2 to ~ 10 MeV. Similar trends are observed also for electron (anti)neutrinos in the case of equilibrium surfaces, just for densities and temperatures larger by a factor of a few and 10 – 15%, respectively. Qualitatively different behavior is observed for the equilibrium decoupling of heavy-flavor neutrinos ν_x , for which temperatures in the range 5 – 12 MeV are observed, usually increasing the equilibrium decoupling density by one order of magnitude. All the results of this work are robust with respect to the optical depth calculation algorithm and to the grid resolution but depend strongly on the approximate neutrino transport scheme used for the simulations. While the present leakage+M0 treatment is expected to capture the dominant cooling features of neutrino emission, the lack of explicit modeling of trapped neutrinos and uncertainties in the challenging radiation transport can more significantly affect the electron fraction inside the remnant. Thus, we expect the values of the density and temperature at the decoupling surfaces to be more robust than the ones of the electron fraction. Improving the treatment of neutrino transport would reflect in an increase in the robustness of the results for Y_e .

For a more detailed presentation of the results, we refer the reader directly to the paper Endrizzi et al., 2020.

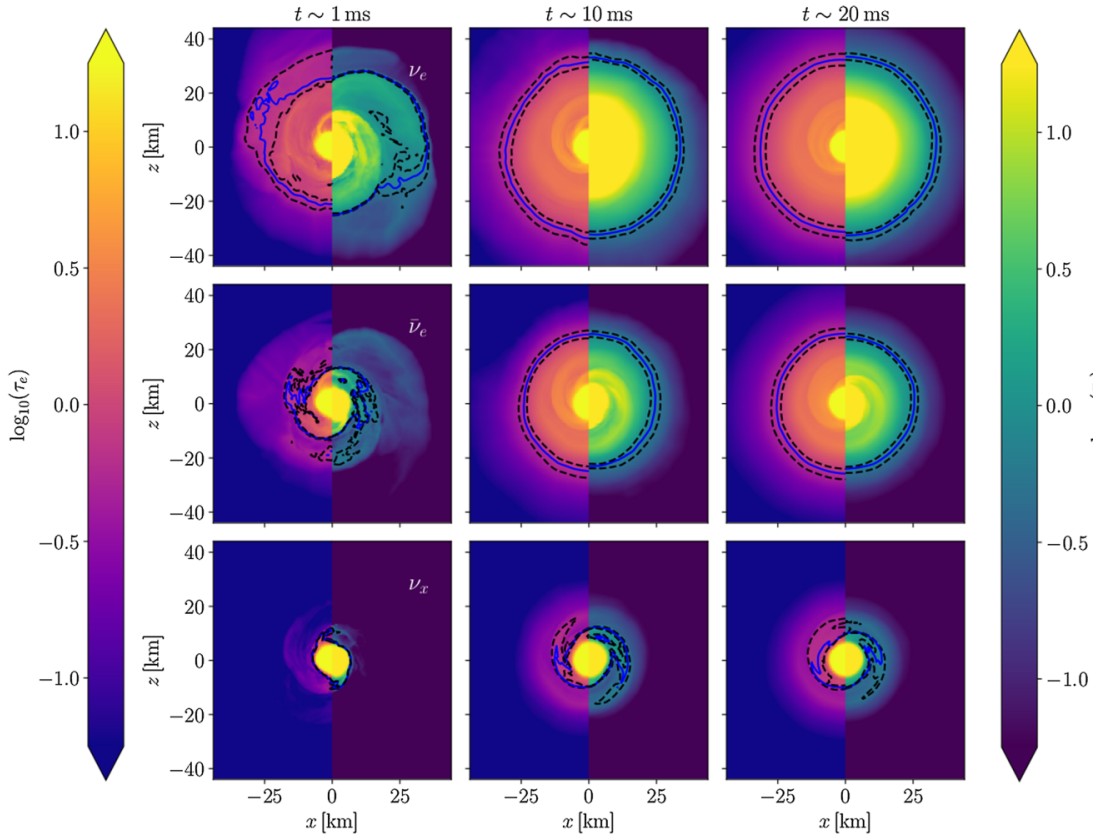


FIGURE 5.4: Equilibrium optical depth for the DD2 model at 20 ms after merger, evaluated with energy-dependent (left side) and energy-integrated (right side) opacities for each neutrino species (ν_e , top; $\bar{\nu}_e$, middle; ν_x , bottom) on the equatorial plane. The energy-dependent opacities are evaluated at the mean neutrino energies at infinity. The solid blue contours represent the surface where τ_{eq} ($\bar{\tau}_{eq}$) = 2/3, while the black dashed lines are the boundaries of the regions where $0.5 < \tau_{eq}$ ($\bar{\tau}_{eq}$) < 0.85.

From Endrizzi et al., 2020

5.2 BAM GRMHD implementation

As a separate project, led by our collaborator Prof. Tim Dietrich, we implemented a new module in BAM capable of evolving the classical hydrodynamics system with the addition of magnetic fields in full GRMHD fashion. For this project we make use of all the definitions in Sec. 3.2 and in general we follow the implementations in the work of Anton et al., 2006; Giacomazzo et al., 2007; Liebling et al., 2010; Penner, 2011.

The aim of this work is to extend the capabilities of the BAM code to include more and more aspects of the physical treatments of compact objects' evolution, extending the potentialities of the code towards simulations of ejecta and element production.

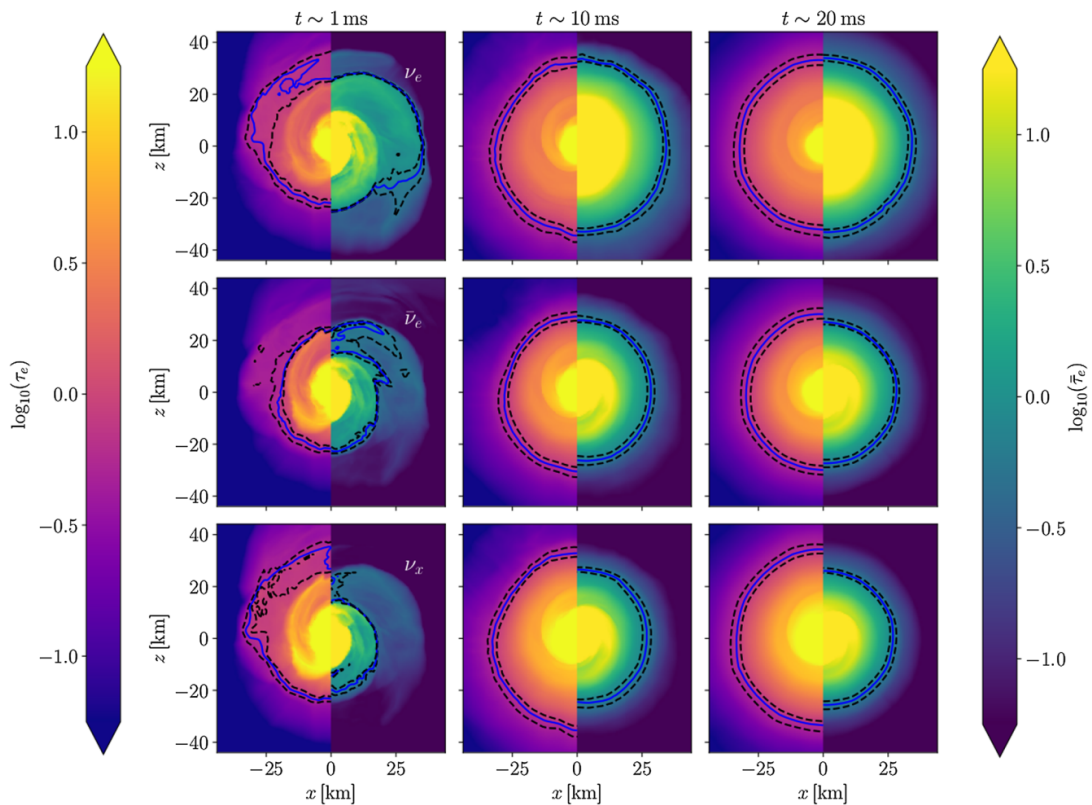


FIGURE 5.5: Same as Fig. 5.4 for the diffusion optical depths τ_{diff} (left side) and $\bar{\tau}_{\text{diff}}$ (right side).

From Endrizzi et al., 2020

As already mentioned in the previous section, a rising interest in the analysis of post-merger compact binary objects remnants has developed in recent years. The reasons for this are multiple but the driving arguments follow the detectability of EM signals, to corroborate the detection of GWs from the advanced LIGO and advanced *Virgo* interferometers. In particular, the possibility of SGRBs being prompted by a specific configuration of the magnetic field in the remnant has been extensively discussed (e.g. see Price et al., 2006; Kiuchi et al., 2015 for magnetic field amplifications and Rezzolla et al., 2011; Paschalidis et al., 2015; Sun et al., 2022 for the launch of a jet) but as of today the mechanism to prompt the emission of such ejecta has not yet been proven, although the follow-up EM detections to GW170817 have confirmed the relation between BNS and SGRB. The importance of adding improved matter and hydrodynamics treatments to our code is then clear: despite the state-of-the-art results of the code in the field of BNS we want to be able to further explore the parameter space of BNS properties.

In the following, we are going to describe the basic aspects of the GRMHD implementation used in Sec. 5.2.1 and the results obtained in Sec. 5.2.2.

5.2.1 Implementation

As stated before we follow the work of Anton et al., 2006; Giacomazzo et al., 2007; Liebling et al., 2010; Penner, 2011 and we are going to outline the main choices done in this context in the following. The main challenge in the choice of implementation is to adapt the new module to the underlying BAM infrastructure.

Divergence Cleaning

One of the major problems in the implementation of GRMHD equations in a numerical code is the treatment of the *divergence-free* condition $\nabla \cdot B = 0$ also expressed in Eq. (3.58). For this work we use the **divergence cleaning** approach first described in Dedner et al., 2002 for MHD and better developed for GR in Liebling et al., 2010; Penner, 2011. Divergence cleaning enforces the divergence-free constraint by adding an additional field ψ and an appropriate evolution equation which serves the purpose of imposing the constraint and damping possible violations arising during the evolution. Although divergence cleaning is known not to be the better performing method in GRMHD codes we deemed it to be best suited to BAM to produce a first working implementation. We are not going to discuss other possible method to enforce the divergence-free constraint here but we refer to other works for the so-called *Constrained Transport* (CT) method first described in Evans et al., 1988 and later developments in Balsara et al., 1999; Tóth, 2000 and the *Vector Potential* evolution, first introduced in Etienne et al., 2012; Etienne et al., 2010 and used, for example, in the `WhiskyMHD` code (as in Giacomazzo et al., 2007) and the `Spritz` code in Cipelletta et al., 2020. As a last comment, these more modern methods rely on a *staggered grid* implementation (see Fig. 5.6), and would had required a modification of the grid structure of BAM (see Sec. 4.2.1) that we are leaving for future developments. We can rewrite Eq. (3.31) for the case of GRMHD specifically in integral form using Eq. (3.61), Eq. (3.62) and Eq. (3.63).

We have then to introduce an evolution equation for ψ , which represents an auxiliary field, introduced precisely for the divergence-free condition

$$\nabla_{\mu} (*F^{\mu\nu} + g^{\mu\nu}\psi) = \kappa n^{\nu}\psi, \quad (5.10)$$

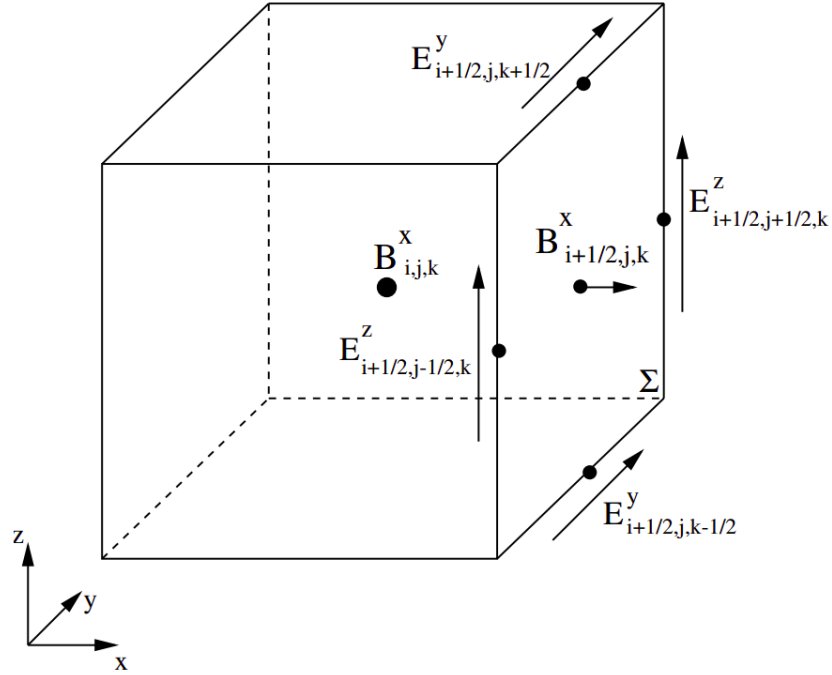


FIGURE 5.6: Schematic diagram of the staggered grid and relative position of the data needed for the CT scheme. The evolution of $B_{i+1/2,j,k}^x$ is determined by the values of the electric field \vec{E} at the edges of the surface Σ located at $(i + 1/2, j, k)$.

From Giacomazzo et al., 2007

which just comes from Eq. (3.47).

The parameter κ is there as a damping parameter to drive to 0 any violations to the divergence-free constraint.

From this, we arrive at:

$$\partial_t \psi + \partial_i \left(\frac{\alpha B^i}{\sqrt{\gamma}} - \psi \beta^i \right) = \psi (-\kappa \alpha - \partial_i \beta^i) + B^i \partial_i \left(\frac{\alpha}{\sqrt{\gamma}} \right). \quad (5.11)$$

This leads to a modification of the evolution equation for \tilde{B}^i first expressed in Eq. (3.59)

$$\partial_t \tilde{B}^j + \partial_i \left[(\alpha v^i - \beta^i) \tilde{B}^j - \alpha v^j \tilde{B}^i + \alpha \sqrt{\gamma} \gamma^{ij} \zeta \right] = \quad (5.12)$$

$$= -\tilde{B}^i \partial_i \beta^j + \zeta \partial_i (\alpha \sqrt{\gamma} \gamma^{ij}) = \quad (5.13)$$

$$= -\tilde{B}^i \partial_i \beta^j + \zeta \sqrt{\gamma} \gamma^{ij} \partial_i \alpha + \zeta \alpha \sqrt{\gamma} \left(\frac{1}{2} \gamma^{ij} \gamma^{kl} \partial_i \gamma_{kl} - \gamma^{jk} \gamma^{il} \partial_i \gamma_{kl} \right). \quad (5.14)$$

Energy Momentum Tensor

The energy momentum tensor is defined as in Eq.(3.60):

$$T^{\mu\nu} = (\rho h + b^2) u^\mu u^\nu + \left(p + \frac{b^2}{2} \right) g^{\mu\nu} - b^\mu b^\nu. \quad (5.15)$$

For the implementation in BAM we make use of the definition already introduced in Eq. (3.67) together with an additional definition for η :

$$\tilde{V}^i = v^i - \beta^i / \alpha, \quad (5.16)$$

$$\eta = W^2(\rho + \rho\epsilon + p + b^2) = \frac{W^2}{\rho} \left(1 + \epsilon + \frac{(p + b^2)}{\rho} \right), \quad (5.17)$$

and we also have defined new extended quantities in the context of GRMHD, for the sake of compactness of the equations

$$p^* = p + p_{\text{mag}} = p + b^2/2, \quad (5.18)$$

$$h^* = 1 + \epsilon + (p + b^2)/\rho, \quad (5.19)$$

that leads to a rewriting of the energy-momentum tensor as

$$T^{\mu\nu} = h^* u^\mu u^\nu + p^* g^{\mu\nu} - b^\mu b^\nu, \quad (5.20)$$

the components of which can be now written as

$$T^{00} = (\eta - p - \frac{1}{2}b^2)/\alpha^2 - (b^0)^2, \quad (5.21)$$

$$T^{0i} = \eta \frac{\tilde{V}^i}{\alpha} + p^* \frac{\beta^i}{\alpha^2}, \quad (5.22)$$

$$T^{ij} = \eta \tilde{V}^i \tilde{V}^j + p^* (g^{ij} - \beta^i \beta^j / \alpha^2) - b^i b^j, \quad (5.23)$$

where now $\eta = \frac{W^2 h^*}{\rho}$.

Con2Prim Routine

The importance of converting conservative variables back to their relative primitive counterparts has been already stressed in Sec. 3.1.2 but for more details, we point the reader to Appendix E. In the context of GRMHD, the additional magnetic field variables increase the complexity of the reconstruction of primitive variables. For this

reason, for the implementation of such a routine, we referred to the work by Siegel et al., 2018, focused specifically on the analysis of different reconstruction schemes in GRMHD, of which we implemented a 1D conservative-to-primitive reconstruction scheme from Neilsen et al., 2014; Palenzuela et al., 2015 described in the following. We begin by defining the variable $x = hW$ and write the equation

$$f(x) = x - \hat{h}\hat{W} = (1 + \hat{\epsilon} + \frac{\hat{p}}{\hat{\rho}})\hat{W}. \quad (5.24)$$

Here we solve for x using the Newton-Raphson root finder. We know that x is bound within $1 + q - s < x < 2 + 2q - s$.

We then define the additional quantities:

$$q = \frac{\tau}{D}, \quad r = \frac{S^2}{D^2}, \quad (5.25)$$

$$s = \frac{B^2}{D}, \quad t = \frac{B_i S^i}{D^{3/2}}. \quad (5.26)$$

The quantities labeled with $\hat{\cdot}$ are obtained at every iteration step from x . We can derive the Lorentz factor W from

$$W^{-2} = 1 - \frac{x^2 r + (2x + s)t^2}{x^2(x + s)^2}. \quad (5.27)$$

Additionally, we can write

$$\epsilon = -1 + \frac{x}{W} (1 - W^2) + W \left(1 + q - s + \frac{1}{2} \left(\frac{t^2}{x^2} + \frac{s}{W^2} \right) \right). \quad (5.28)$$

Finally, we do get the density from $\rho = D/W$, the pressure p from the EOS and we can compute the velocity from:

$$v^i = \frac{\gamma^{ij} S_j}{z + B^2} + \frac{(B^j S_j) B^i}{z(z + B^2)}, \quad (5.29)$$

with $z = x\rho W$.

We have also started testing different schemes described in Siegel et al., 2018 like the 2D scheme from Noble et al., 2006 but these implementations did not yield substantial results to prompt further investigations.

Eigenvalues

For the calculation of the eigenvalues needed by the HRSCS we refer to Gammie et al., 2003 and Anton et al., 2006. Computing the eigenvalues used in the Flux formula is more difficult than in the pure GRHD case and also computationally much more expensive since it involves the solution of a quartic equation as described at the end of Sec. 3.2. There are in general two possible approaches: an exact solution for the eigenvalues and an approximate one, described in the following.

Depending on the type of HRSCS we employ we might only rely on the highest propagation speed among the ones coming from the wave decomposition. Thus, we remind the relation between the eigenvalues coming from the GRMHD system, already described in Fig. 3.1:

$$\lambda_{f-}^i \leq \lambda_{a-}^i \leq \lambda_{s-}^i \leq \lambda_e^i \leq \lambda_{s+}^i \leq \lambda_{a+}^i \leq \lambda_{f+}^i, \quad (5.30)$$

where again the labels refer to, respectively, f = fast magnetosonic waves, a = Alfvén waves, s = slow magnetosonic waves, e = entropy or matter wave.

Exact Eigenvalues To compute the exact solution for the eigenvalues we employ a Newton-Raphson scheme, where we first evaluate the known expressions of the eigenvalues corresponding to the entropy wave and the Alfvén waves, as in Eq. (3.68) and Eq. (3.69).

As in Sec. 3.2 we know that there are four additional (two fast $\lambda_{f\pm}^i$, two slow $\lambda_{s\pm}^i$) magnetosonic waves which come from the solution of the quartic equation Eq. (3.70). To solve the quartic equation we approach the problem numerically and use a Newton-Raphson solver to obtain the solutions.

On top of this, we have 2 eigenvalues coming from the divergence cleaning approach whose values are equal to the speed of light c , so the full decomposition looks like

$$\lambda_{dc-} = c \leq \lambda_{f-}^i \leq \lambda_{a-}^i \leq \lambda_{s-}^i \leq \lambda_e^i \leq \lambda_{s+}^i \leq \lambda_{a+}^i \leq \lambda_{f+}^i \leq \lambda_{dc+} = c. \quad (5.31)$$

Once we have obtained the full decomposition, in the case of an HLL-type solver, we want to consider the highest propagation speeds. We can then use, for a generic direction i

$$\lambda_+^i = \max(0, \lambda_{f+,L}^i, \lambda_{f+,R}^i), \quad (5.32)$$

$$\lambda_-^i = \max(0, \lambda_{f-,L}^i, \lambda_{f-,R}^i), \quad (5.33)$$

where L, R refer to the left and right state of a given interface and $-, +$ to the wave propagating towards, respectively, the left and right direction.

Since the divergence cleaning eigenspace is equal to c , we could also simply pass to the HLL solver the latter, skipping the calculation of the eigenvalues. This approach has not proven effective in our tests.

Approximate Eigenvalues Since the exact computation of the eigenvalues could significantly slow down numerical runs, we also introduced an approximate eigenvalues solver, following Gammie et al., 2003. In the approximate case, we instead use the entropy wave as in the exact case, an approximate Alfvén wave solution as

$$\lambda_A = \sqrt{b^2/(\rho h^*)}. \quad (5.34)$$

We further define

$$V \equiv \lambda_A^2 + c_s^2(1 - \lambda_A^2), \quad (5.35)$$

$$\tilde{V} \equiv \lambda_e/\alpha, \quad (5.36)$$

where λ_e is defined in (3.68), and

$$a = W^2(V - 1)V, \quad (5.37)$$

$$b = \alpha W^2 \tilde{V}(V - 1) + V\beta^i, \quad (5.38)$$

$$c = (\alpha W \tilde{V})^2(V - 1) + V(\alpha^2 g^{ii} - \beta^i \beta^i), \quad (5.39)$$

again without summation over repeated indices. The final eigenvalues are then:

$$\lambda_+ = (b + \sqrt{b^2 - ac})/a, \quad (5.40)$$

$$\lambda_- = (b - \sqrt{b^2 - ac})/a. \quad (5.41)$$

Additionally, we could also use the analytically given Alfvén wave results from the exact solution.

Initial Data

The initial data (ID) problem for GRMHD represents a peculiar case in the implementation of numerical codes: solving the constraint equations for ID incorporating

magnetic field represents a complex problem that still hasn't been solved. As a solution, we compute the ID for NS systems (BHNS and BNS or single stars), since the magnetic fields are tied to matter, and then we “attach” the selected magnetic field configuration to the system during the initialization of the ID. At the time $t = 0$ a magnetic field is then superimposed to the star/stars together with appropriate gauge and boundary conditions to limit the constraint violation.

In our treatment, we decided to express the ID as a poloidal field, in terms of the 4-potential A^μ . This is defined in relativistic electrodynamics as

$$A^\mu = (\phi, \vec{A}), \quad (5.42)$$

where ϕ is the electric potential and \vec{A} is the 3D magnetic vector potential, that is defined so that its curl is equal to the magnetic field \vec{B} , $\nabla \times \vec{A} = \vec{B}$.

We put ourselves in cylindrical coordinates so that we only have to provide the component A_ϕ :

$$A^\mu = (0, \vec{A}) = (0, A_\rho, A_\phi, A_z) = (0, 0, A_\phi, 0), \quad (5.43)$$

where

$$A_\phi = A_b \rho^2 \max(P - P_{cut}, 0)^{n_b}. \quad (5.44)$$

Here n_b is the order of differentiability of the pressure ($n_b = 2$), P_{cut} is a cutoff to limit the B field inside the star (1% of P_{max}), A_b is a scalar determining the strength of the B field.

Now we need to calculate B^i in Cartesian coordinates:

$$\begin{aligned} B^i &= \epsilon^{ijk} \nabla_j A_k = \left(\frac{\partial A_z}{\partial y} - \frac{\partial A_y}{\partial z} \right) \hat{x} + \left(\frac{\partial A_x}{\partial z} - \frac{\partial A_z}{\partial x} \right) \hat{y} + \left(\frac{\partial A_y}{\partial x} - \frac{\partial A_x}{\partial y} \right) \hat{z} \\ &= \left(-\frac{\partial A_y}{\partial z} \right) \hat{x} + \left(\frac{\partial A_x}{\partial z} \right) \hat{y} + \left(\frac{\partial A_y}{\partial x} - \frac{\partial A_x}{\partial y} \right) \hat{z}, \end{aligned} \quad (5.45)$$

$$A_z = 0. \quad (5.46)$$

We need now to express A_ϕ in Cartesian coordinates:

$$\bar{A}_i = \frac{\partial x^j}{\partial x^i} A_j, \quad (5.47)$$

$$\begin{aligned} A_i &= \left(\frac{\partial \phi}{\partial x} \delta_i^x + \frac{\partial \phi}{\partial y} \delta_i^y \right) A_\phi = \left(\frac{\partial \arctg(\frac{y}{x})}{\partial x} \delta_i^x + \frac{\partial \arctg(\frac{y}{x})}{\partial y} \delta_i^y \right) A_\phi \\ &= \left(\frac{-y}{x^2} \frac{1}{\sqrt{1 + \frac{y^2}{x^2}}} \delta_i^x + \frac{1}{x \sqrt{1 + \frac{y^2}{x^2}}} \delta_i^y \right) A_\phi \\ &= \left(-\frac{y}{\rho^2} \delta_i^x + \frac{x}{\rho^2} \delta_i^y \right) A_\phi. \end{aligned} \quad (5.48)$$

Now using

$$P_{max} \equiv \max(P - P_{cut}, 0), \quad (5.49)$$

we then get

$$B^x = -\frac{\partial A_y}{\partial z} = \frac{\partial}{\partial z} \left(\frac{x}{\rho^2} A_\phi \right) = -2A_b x P_{max} \frac{\partial P_{max}}{\partial z}, \quad (5.50)$$

$$B^y = \frac{\partial A_x}{\partial z} = \frac{\partial}{\partial z} \left(-\frac{y}{\rho^2} A_\phi \right) = -2A_b y P_{max} \frac{\partial P_{max}}{\partial z}, \quad (5.51)$$

$$\begin{aligned} B^z &= \frac{\partial A_y}{\partial z} = \frac{\partial A_y}{\partial x} - \frac{\partial A_x}{\partial y} = A_\phi \frac{\partial}{\partial x} \left(\frac{x}{\rho^2} \right) + A_\phi \frac{\partial}{\partial y} \left(\frac{y}{\rho^2} \right) + \frac{x}{\rho^2} \frac{\partial A_\phi}{\partial x} + \frac{y}{\rho^2} \frac{\partial A_\phi}{\partial y} \\ &= A_\phi \left[\frac{2}{\rho^2} - \frac{2x}{\rho^4} - \frac{2y}{\rho^4} \right] + \frac{x}{\rho^2} A_b \left(2x P_{max} + 2\rho^2 P_{max}^2 \frac{\partial P_{max}}{\partial x} \right) \\ &\quad + \frac{y}{\rho^2} A_b \left(2y P_{max} + 2\rho^2 P_{max}^2 \frac{\partial P_{max}}{\partial x} \right) \\ &= \left(\frac{2x^2}{\rho^2} + \frac{2y^2}{\rho^2} \right) A_b P_{max}^2 + 2A_b P_{max} \left(x \frac{\partial P_{max}}{\partial x} + y \frac{\partial P_{max}}{\partial y} \right) \\ &= 2A_b P_{max} \left[P_{max} + \left(x \frac{\partial P_{max}}{\partial x} + y \frac{\partial P_{max}}{\partial y} \right) \right], \end{aligned} \quad (5.52)$$

that can be written in a more readable way as

$$B^x = -2A_b x P_{max} \frac{\partial P_{max}}{\partial z}, \quad (5.53)$$

$$B^y = -2A_b y P_{max} \frac{\partial P_{max}}{\partial z}, \quad (5.54)$$

$$B^z = +2A_b P_{max} \left[P_{max} + \left(x \frac{\partial P_{max}}{\partial x} + y \frac{\partial P_{max}}{\partial y} \right) \right]. \quad (5.55)$$

As a comparison, we report here a different implementation of magnetic ID, commonly used in the *Whisky* code (Giacomazzo et al., 2007) and in its successor, the *Spritz* code (Cipolletta et al., 2020), which instead relies on a first-order in pressure implementation.

$$B^x = -x A_b \rho^2 \frac{\partial P_{max}}{\partial z}, \quad (5.56)$$

$$B^y = -y A_b \rho^2 \frac{\partial P_{max}}{\partial z}, \quad (5.57)$$

$$B^z = +A_b \rho^2 \left(4P_{max} + x \frac{\partial P_{max}}{\partial x} + y \frac{\partial P_{max}}{\partial y} \right). \quad (5.58)$$

An example of ID produced in with this implementation can be seen in Fig. 5.7.

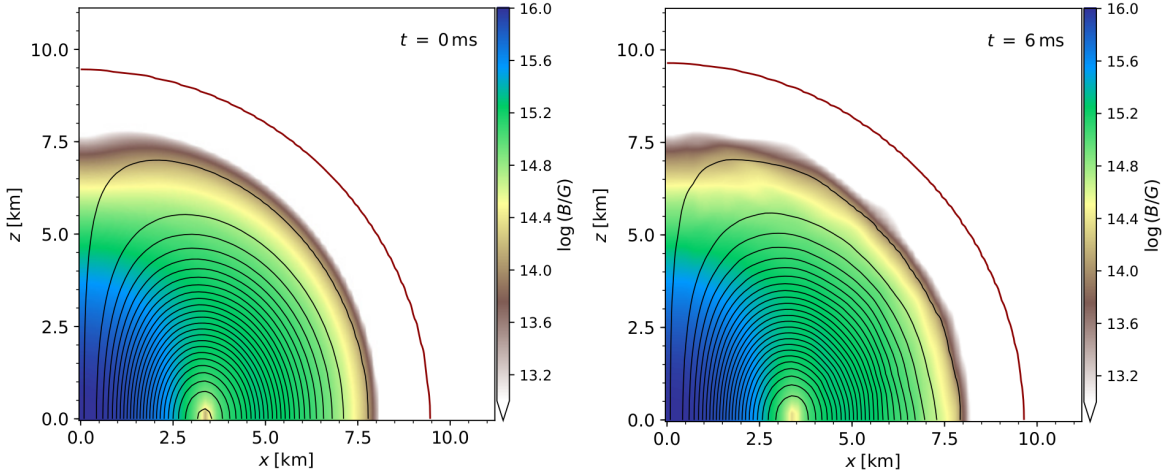


FIGURE 5.7: Examples of TOV simulations with poloidal magnetic field computed with the GRMHD code *Spritz* introduced in Cipolletta et al., 2020. Black lines represent isocontours of the ϕ -component of the vector potential, while the red line corresponds to $\rho \sim 3 \times 10^{12} \text{g/cm}^3$.

From Cipolletta et al., 2021.

5.2.2 Results

In this section, we present the results of the different tests done to verify the correctness of the implementation. To date, the implementation is not yet complete and more effort is needed in order to produce a stable release of the module. Nevertheless, we can produce and show the meaningful results obtained so far in this context.

TABLE 5.2: Initial values of the density ρ , the pressure p , the velocity v_i and the magnetic field B_i components, $i = x, y, z$ for the five Balsara tests described in Balsara, 2008 along the x direction. For each test we present the Left (L) and Right (R) states with respect to a shock front initially set in $X = 0$.

Test	ρ	p	v_x	v_y	v_z	B_y	B_z	B_x
1,L	1.0	1.0	0.0	0.0	0.0	1.0	0.0	0.5
1,R	0.125	0.1	0.0	0.0	0.0	-1.0	0.0	0.5
2,L	1.0	30.0	0.0	0.0	0.0	6.0	6.0	5.0
2,R	1.0	1.0	0.0	0.0	0.0	0.7	0.7	5.0
3,L	1.0	1000	0.0	0.0	0.0	7.0	7.0	10.0
3,R	1.0	0.1	0.0	0.0	0.0	0.7	0.7	10.0
4,L	1.0	0.1	0.999	0.0	0.0	7.0	7.0	10.0
4,R	1.0	0.1	-0.999	0.0	0.0	-7.0	-7.0	10.0
5,L	1.08	0.95	0.4	0.3	0.2	0.3	0.3	2.0
5,R	1.0	1.0	-0.45	-0.2	0.2	-0.7	0.5	2.0

1D

As standard 1D tests, we performed the *Balsara* shock-tube tests described in Balsara, 2008 and whose exact solutions were computed in Giacomazzo et al., 2006. The five different shock-tube tests each stress different aspects of a GRMHD code, such as high velocities (close to c , speed of light), high pressure, or high magnetic fields.

In Fig. 5.8, Fig. 5.9, Fig. 5.10 and Fig. 5.11 we present the Balsara tests performed with our implementation. The initial values of the physical quantities of the fluid per each test are listed in Table. 5.2 We found consistency between our results and the exact solution for Balsara Test 1, employing also different limiters like the LINTVD limiter, based on *minmod* and *monotonized centered* slope limiters (see Toro, 2013; Harten, 1997), the third-order convex-essentially-non-oscillatory (CENO3) algorithm (see Liu et al., 1998; Zanna et al., 2002), and the fifth-order weighted-essentially-non-oscillatory finite difference schemes (WENOZ) (see Borges et al., 2008), as can be seen in Fig. 5.8 and Fig. 5.9. For more robustness, we used the low order scheme LINTVD as default for our tests. Balsara Test 2 was conclusive in the same way, showing how increasing resolution would result in a profile closer to the exact solution (see Fig. 5.10). From these tests, we saw how moderate discontinuities in the pressure p , the density ρ , and the magnetic field components B_i are well handled by the code. Balsara Tests 3 and 4 proved not to be conclusive, with the first one not able to produce meaningful results and the second one showing curves which are detached from the

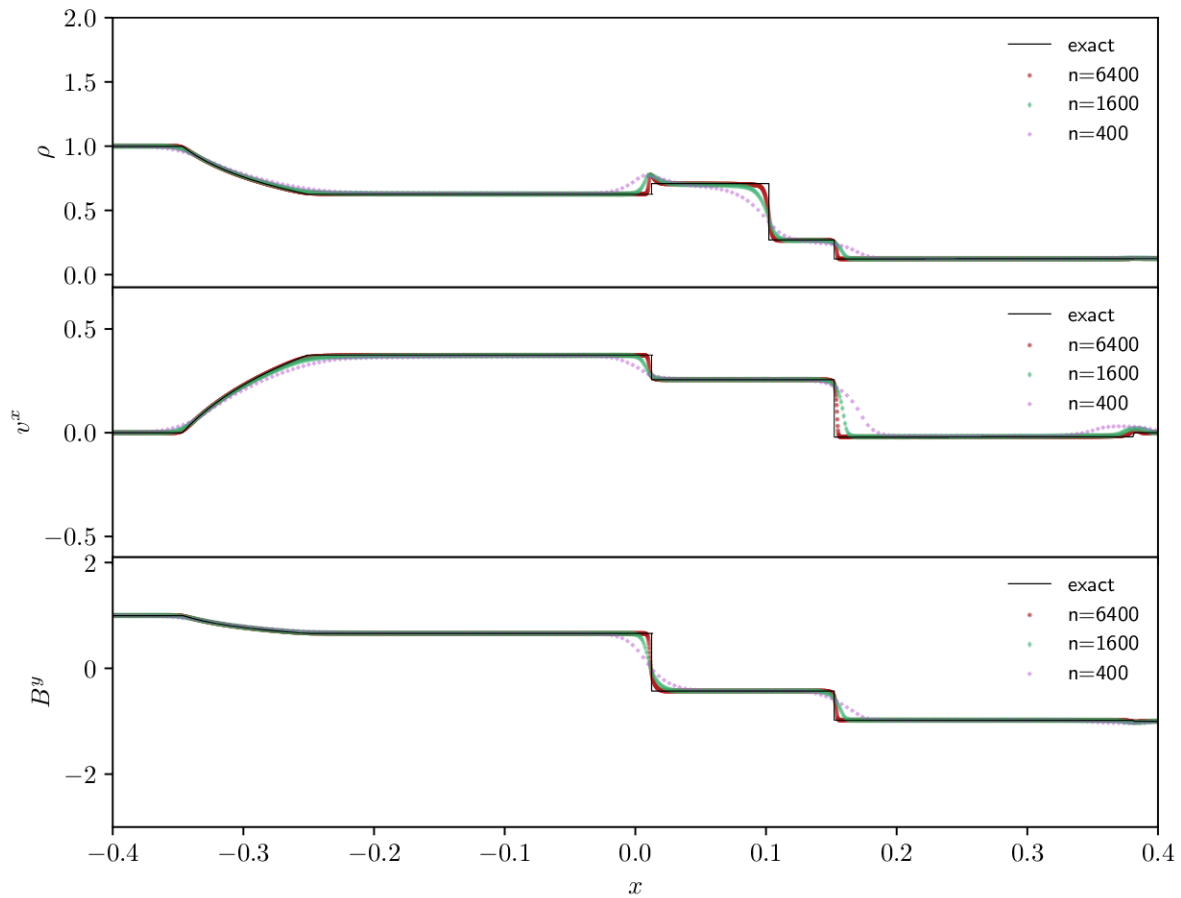
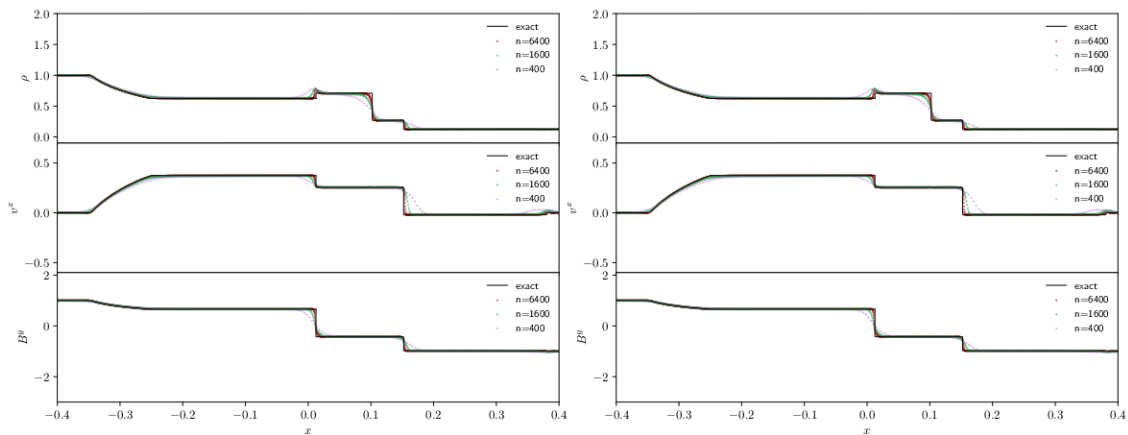


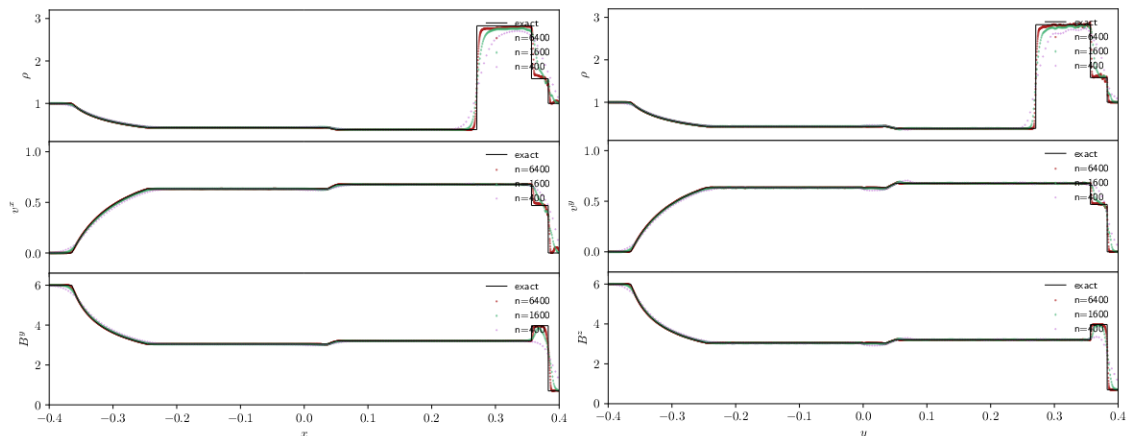
FIGURE 5.8: Results for Balsara Test 1 along the x direction using a TVD limiter. In the plot we compare the results obtained for different resolutions, $n = 400, 1600, 6400$ points with the exact solution obtained from Giacomazzo et al., 2006.



(A) Same as Fig. 5.8 but for CENO3 limiter (B) Same as Fig. 5.8 but for WENOZ limiter.

FIGURE 5.9: Comparison of results for Balsara Test 1 of TVD limiter with the CENO3 limiter.

exact solution, proving to be far from the desired result (see Fig. 5.11a). This identifies a problem in the handling of extreme discontinuities in the pressure p and the velocity. We suspect a problem is lying in the `con2prim` routine, invoked at every evolution step to calculate the primitive variables from the conserved ones. Different routines have been tested in this context without proving to be effective, as mentioned in the previous section. Balsara Test 5 has given mixed results, depending on the `con2prim`



(A) Results for Balsara Test 2 along the x direction. (B) Results for Balsara Test 2 along the y direction.

FIGURE 5.10: Comparison of results for Balsara Test 2 along the x and y directions. In the plot we compare the results obtained for different resolutions, $n = 400, 1600, 6400$ points with the exact solution obtained from Giacomazzo et al., 2006.

routine and the flux routine adopted. In Fig. 5.11b we show an example of results for a run with the HLL flux scheme and we see the result to be in agreement with the analytical solution in Giacomazzo et al., 2006. Other `con2prim` routines or flux schemes (like LLF) produce results that match the analytical solution but only for the coarsest resolution (i.e. 400 points). For more details regarding different types of flux schemes, please point the reader to Shibata, 2015; Rezzolla et al., 2013.

TOV

We tested our code on a single stable NS (TOV), to prove the functionality of the superimposition of the magnetic field onto the NS at $t = 0$ and the stability of the star itself. To study this case, we evolved a stable TOV of $M_b^{NS} = 1.35$ and modeled using a simple polytropic EOS with $K = 100$ and $\Gamma = 2$. For this case, a LINTVD limiter has been used. In this case, a poloidal magnetic field with maximum intensity along the z -axis $B^z = 10^{13}$ G has been applied to the ID at $t = 0$, before the evolution starts,

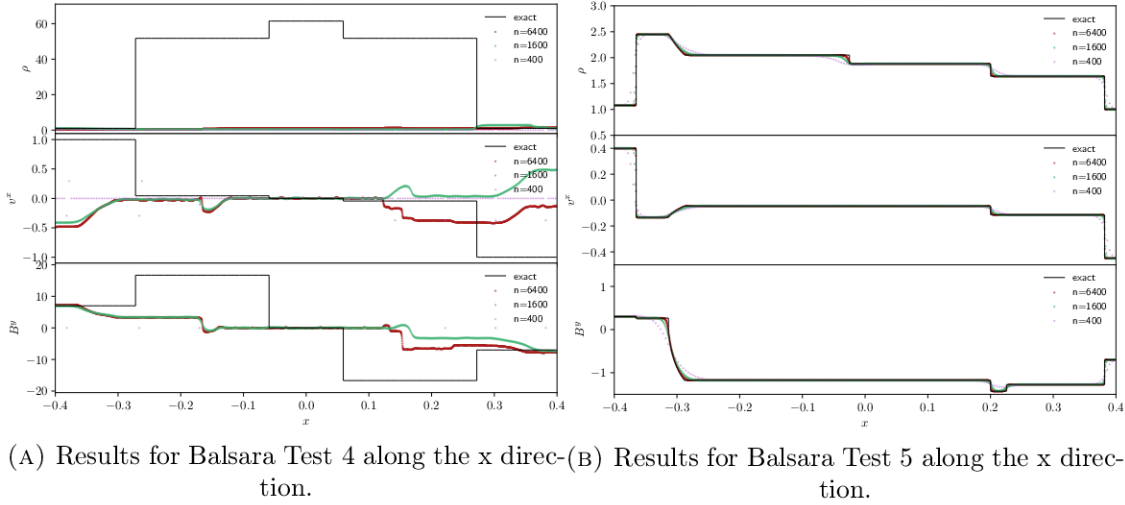


FIGURE 5.11: Comparison of results for Balsara Test 4 and Test 5 along the x direction. In the plot we compare the results obtained for different resolutions, $n = 400, 1600, 6400$ points with the exact solution obtained from Giacomazzo et al., 2006.

as described in Sec. 5.2.1. From the results in Fig. 5.12 and Fig. 5.13, we can see how the TOV at the start of the run present a poloidal field configuration as expected. Comparing Fig. 5.13 with Fig. 5.7 we can see how the magnetic field configuration in the xz -plane is consistent in the two plots.

The evolution poses an additional level of complexity with respect to the simple ID superimposition. Depending on the `con2prim` routine at hand or the limiter used, nonphysical behavior like drifts or oscillation can occur. The surface of the NS already poses a computational problem alone in this context. In Fig. 5.14 basic quantities related to the TOV evolution are shown. It is worth mentioning that the Hamiltonian constraint presents a very high spike initially: this is expected and it is due to the way magnetic ID are handled and added to the system after the data from the ID solver are loaded into the evolution code. At the time $t = 0$ a routine is called to add a specific configuration of the magnetic field (as for example described in Sec.5.2.1) on the star or, more in general, to any density profile evolved. This addition creates an initial violation of the constraints, which is subsequently damped out with the progress of the evolution.

BNS

We briefly report the first tests regarding magnetized BNS. As expected from the previous uncertainty, the test was not successful: the evolution arrived at a halt after

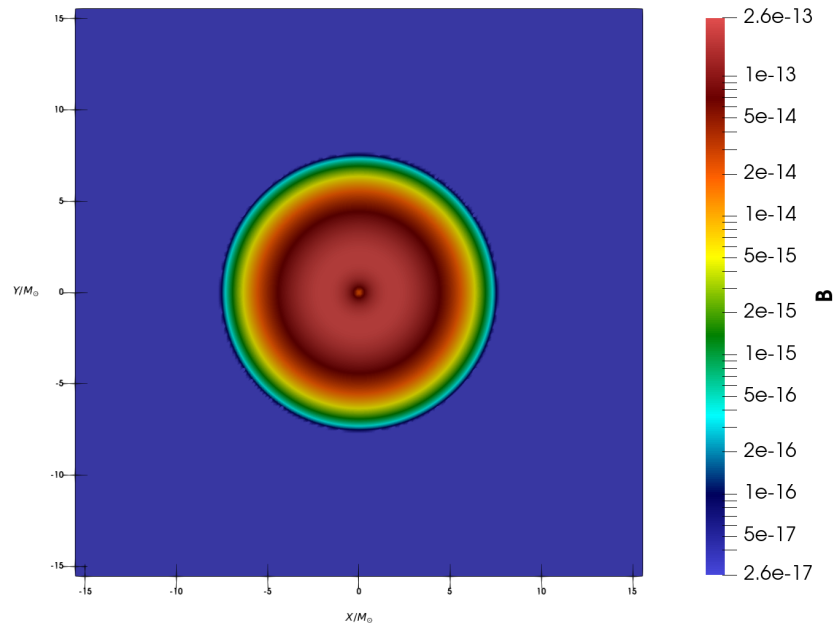


FIGURE 5.12: Magnetic field B configuration for a NS with Poloidal magnetic field initial data. View along the xy -plane. The colorbar shows the magnetic field \mathbf{B} in code's units ($= 10^{20}$ Gauss)

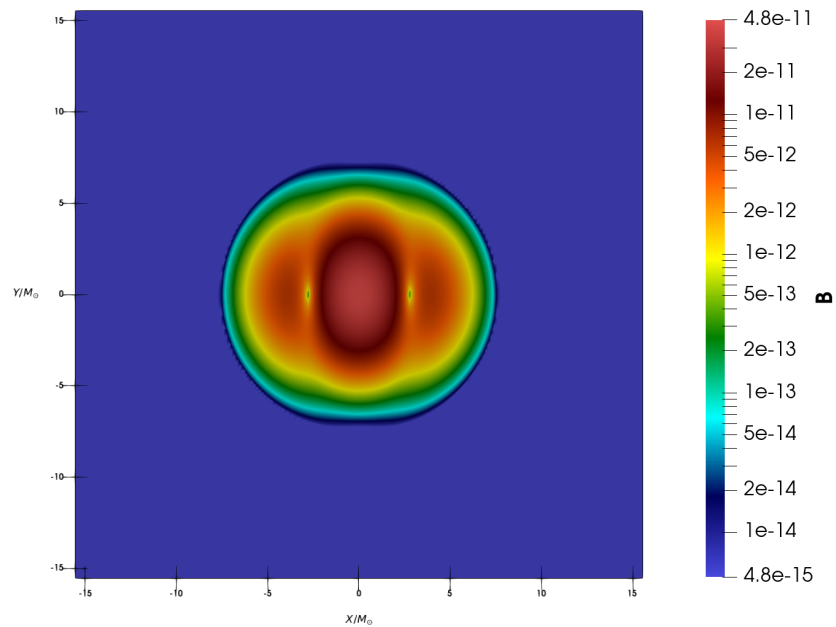


FIGURE 5.13: Magnetic field B configuration for a NS with Poloidal magnetic field initial data. View along the xz -plane. The colorbar shows the magnetic field \mathbf{B} in code's units ($= 10^{20}$ Gauss)

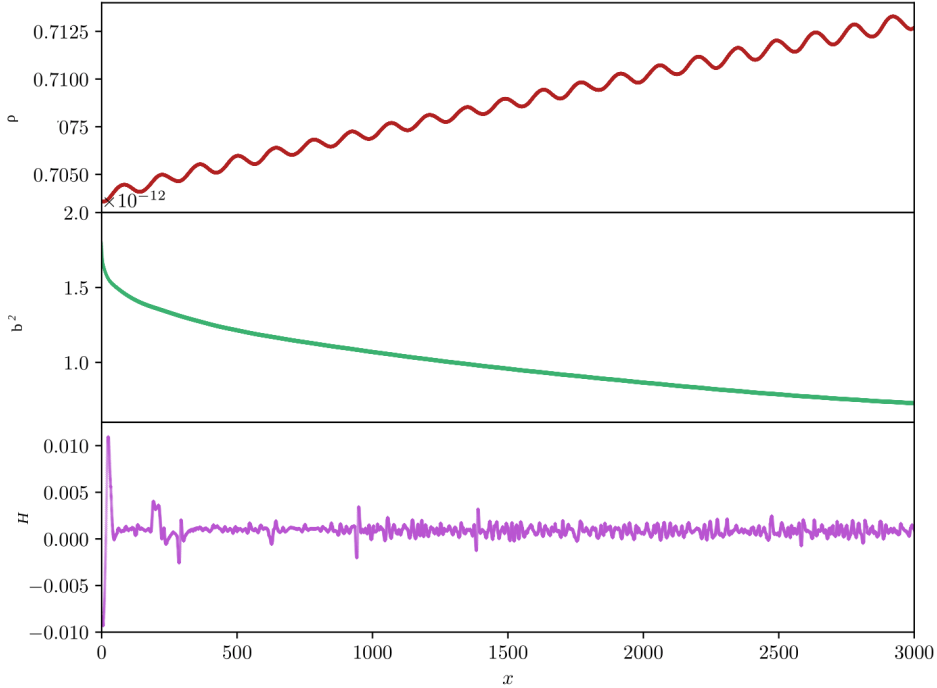


FIGURE 5.14: Density fluctuation ρ , magnetic field variable b^2 and Hamiltonian constraint H for a magnetized TOV. The initial spike in the Hamiltonian constraint is due to the superimposition of the magnetic field to the star.

hundreds of M_\odot of evolution, showing a misplacement of the magnetic field with respect to the NS matter in both stars. More efforts are needed in order to tackle the root of the problem, also reflected in previous tests.

5.3 Mixed Binaries

The first detection of a mixed binary merged dated January 2020, by the LIGO-VIRGO detector network was confirmed with the release of Collaboration et al., 2021. These represent the first confident detections to date of BHNS binaries via any observational means. The two events, carrying the full designations GW200105_162426 and GW200115_042309 and abbreviated henceforth as GW200105 and GW200115, were detected on 2020 January 5 at 16:24:26 UTC and 2020 January 15 at 04:23:10 UTC, respectively. Mixed binaries stand as the system with the highest uncertainty among binary compact systems.

The complexity is represented by uncertainties in their formation channels and in the distribution of the mass ratio of the system (in this work we adopt the convention $q = M_{BH}/M_{NS}$). While there have been predictions of black hole-neutron star

(BHNS) systems before, accounting for their non-detection as well as future possibilities of detection in, e.g., Sigurdsson, 2003; Clausen et al., 2014; Chattopadhyay et al., 2021; Broekgaarden et al., 2021, the two events previously mentioned provide the perfect opportunity to test the global understanding about such mergers. The two BHNS gravitational-wave observations also inspire some fundamental questions about their formation scenario. In Broekgaarden et al., 2021 for example, it has been shown that the masses and merger rates inferred from GW200105 and GW200115 are consistent with formation through isolated binary evolution. In particular, after exploring a large set of binary evolution models, it has been found that low kick velocities or relatively high common envelope efficiencies are preferred to simultaneously match the properties of double NS and double BH systems. To further study this system, more detections and observational data are needed, and, in turn, more accurate simulations. In light of this, we decided to investigate such systems, testing different configurations and exploring the parameter space, specifically for spin, mass ratio, EOS, and orientations.

The first step that needs to be taken for the simulation of compact objects, as already stressed out in Sec. 4.1, is the construction of ID. In light of the great results obtained with the ID code `SGRID`, already described in Sec. 4.1.1, in the context of BNS, the multipurpose ID code `Elliptica` (see Sec. 4.1.2) was developed by Alireza Rashti and Prof. Wolfgang Tichy. The code, even if capable to compute ID for single objects and BNS is intended to add the functionality of computing BHNS ID. Thanks to this great effort we have now in our hands a powerful tool that opens up the possibility of evolving mixed binary systems, with arbitrary spin orientations. It is important to mention that `BAM` has already been proven capable of evolving BHNS ID computed via the `LORENE` code, and produced the results shown in Chaurasia et al., 2021. However, `Elliptica` further extends the capabilities of the `LORENE` codes, for example by allowing arbitrary spin direction, and therefore, widens the part of the parameter space that we are able to explore.

In order to fully present the capability of the code, we performed various tests, centered on bench-marking and stress-testing the main functionalities. We began by showing the self-convergence of the code by showing the decrease in the Hamiltonian and Momentum (defined in Eq. (B.1) and Eq. (B.2)) constraints with increasing resolution in Fig. 5.15. The data reported in the cited plots are summarized in Tab. 5.3 and will be used later for the evolution runs via the `BAM` code. As a second test, we performed a separate batch of ID runs, accounting for the effect of different BH spins

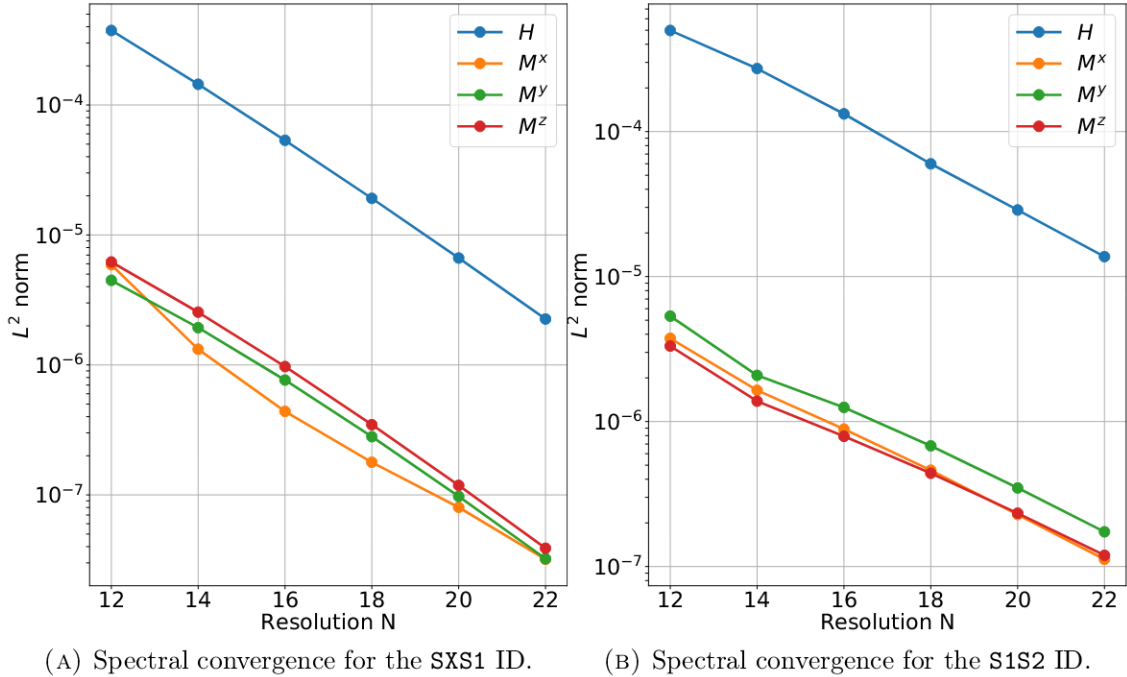


FIGURE 5.15: Comparison of spectral convergence for the Hamiltonian and Momentum constraints for two different ID (see Tab. 5.3), with respect to resolution. The vertical axis shows the L^2 norm of each constraint. The horizontal axis shows the number of points used in each direction inside each cubed sphere patch.

From Rashti et al., 2022

(in both magnitude and direction), and comparing the result with PN curves: we use the 3.5 post-Newtonian (PN) approximation from Blanchet, 2014 plus the next-to-next-to-leading order correction of spin-orbit (SO) interaction from Blanchet, 2014. In Fig. 5.16 we show the results of this comparison, where we obtained good agreement between our results and the PN curves. As a third test, we stressed the capability of the code into computing ID for highly spinning compact objects. We ran a batch of ID runs, keeping one of the two components as spinless and linearly increasing the Omega parameter for the NS (see Eq. (4.39) and Fig. 4.4) or the dimensionless spin χ_{BH} , to increase the spin of the object, up to the highest achievable spin. The separation of the objects, the baryonic mass of the NS, and the irreducible mass of the BH were kept constant for each of the two sets of runs. In Fig. 5.17 we show the consequent increase in the E_{ADM} of the system, resulting from the spin increase.

As already shown in Fig. 4.4 the maximum achievable spin for the NS χ_{NS} is 0.63, in the case of a polytropic EOS with $K = 92.12$ and $\Gamma = 2$, while for the BH the maximum achievable spin χ_{BH} is 0.83. Following these initial tests, we evolved different sets of ID with the code BAM. Despite the range of tests that can be performed on

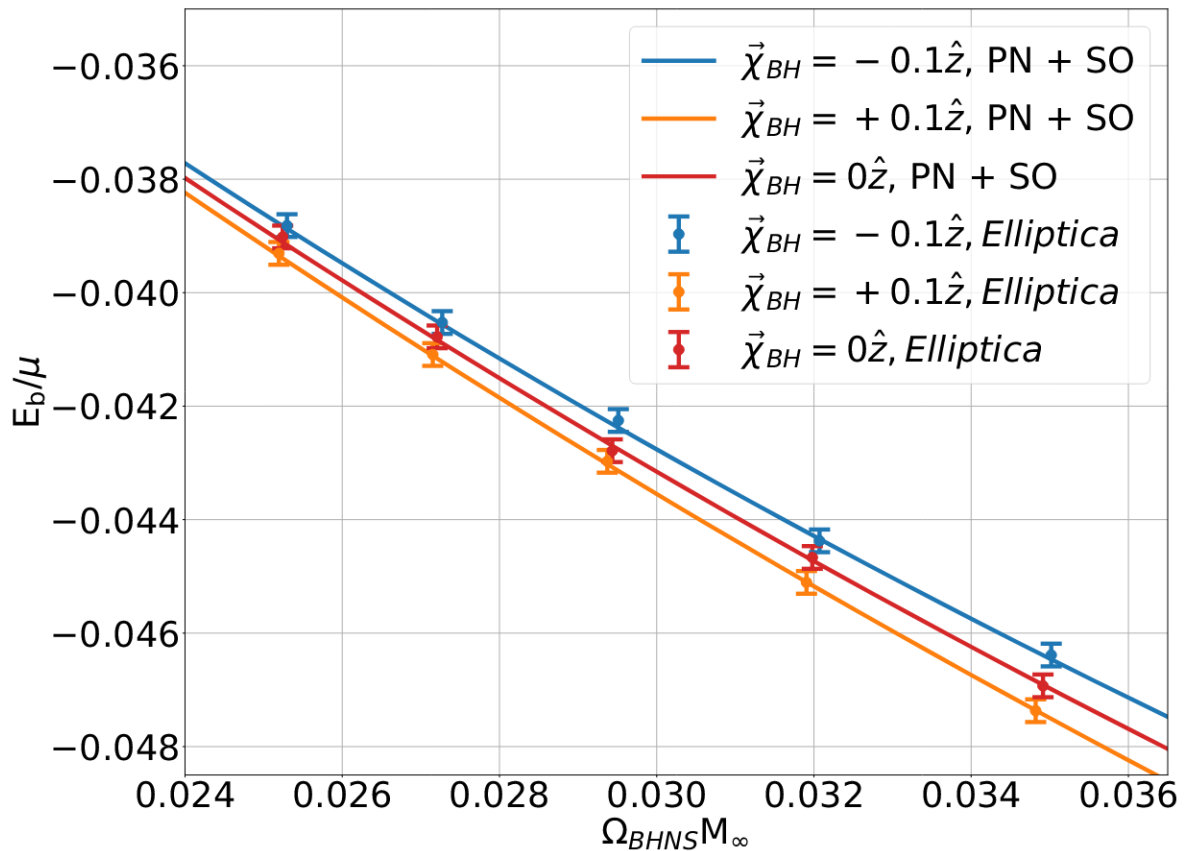


FIGURE 5.16: The binding energy (E_b) of a BHNS system versus orbital angular velocity (Ω_{BHNS}), where the NS spin is zero and $\vec{\chi}_{\text{BH}} = \pm 0.1\hat{z}$. Here, $M_\infty = M_{\text{Chr}} + M_{\text{NS}}$ and $\mu = \frac{M_{\text{Chr}}M_{\text{NS}}}{M_\infty}$. The small vertical bar is the error in the computation of the ADM Mass M_{ADM} , estimated by setting analytical ID for a Schwarzschild BH and then using the formula from Gourgoulhon, 2011 to numerically find M_{ADM} . The difference between this numerical value and the known ADM mass yields the error.

From Rashti et al., 2022

the ID alone, the best way to verify the accuracy of the data produced is to evolve the latter, making use of an evolution code and then compare the stability and the physical quantities obtained from the evolution with the known results. We have chosen to evolve the ID described in Tab. 5.3. In particular, we evolve **SXS1**, which has the same physical parameters as the first run in the SXS collaboration catalog *SXS Gravitational Waveform Database* n.d. (i.e., SXS:BHNS:0001), so that we can directly compare the GW signal obtained with the one present in the database (see Fig. 5.18 for the comparison). In order to evolve quasi-circular orbits for the **SXS1** inspiral, we perform three eccentricity-reduction steps as in Tichy et al., 2019 to obtain the target eccentricity $\lesssim 10^{-3}$. Fig. 5.19 shows the results of this *eccentricity reduction* algorithm for each step. Reducing the eccentricity of the system to acceptable levels

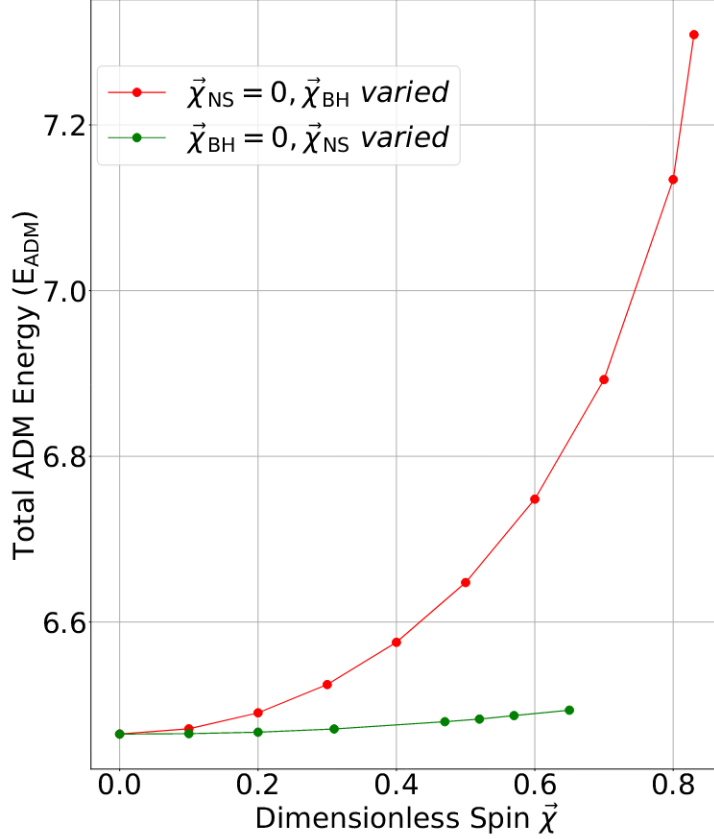


FIGURE 5.17: Total ADM energy E_{ADM} versus the dimensionless spin χ of the spinning object. **Red:** NS spin is kept equal to 0, while the BH spin is increased up to maximum achievable spin. **Green:** BH spin is kept equal to 0, while the NS spin is increased up to break-up spin. Here the BH has irreducible mass $M_{\text{BH}} = 5.2M_{\odot}$ and its dimensionless spin is either $\chi_{\text{BH}} = 0$ or increased in the range $\chi_{\text{BH}} = 0 \div 0.83$, while the NS has baryonic mass $M_{\text{NS}} = 1.4M_{\odot}$ and its dimensionless spin is either $\chi_{\text{NS}} = 0$ or increased in the range $\chi_{\text{NS}} = 0 \div 0.63$. The initial separation is kept constant for all cases at $d = 82M_{\odot}$

is important to remove the imprints of this effect from the GW signal of the inspiral.

The system presents a mass ratio of ~ 6 , which is towards the higher end in the literature range of NR BHNS simulations as, for example, in Kyutoku et al., 2011; Kyutoku et al., 2015. The trajectories of the two objects can be seen in Fig. 5.20. As mentioned in Sec. 4.2.1, to interface the ID produced with `Elliptica` for the evolution we adjust the gauges for the lapse and shift. This adjustment causes oscillations in the constraints and an initial straight motion for both objects, the latter of which is

TABLE 5.3: ID evolved via the BAM code. We have listed the irreducible mass M_{irr} , baryonic mass M_{B} , the mass ratio of the binary q , the initial coordinate distance s , and the total dimensionless spin of each object χ_{BH} , χ_{NS} . For both runs the EOS is a polytropic EOS with $K = 92.12$ and $\Gamma = 2$. The S1S2 ID has $\vec{\chi}_{\text{BH}} = (-0.46, -0.46, -0.46)$ and $\vec{\chi}_{\text{NS}} = (0., 0.32, 0.32)$.

Name	M_{irr}	M_{B}	q	s	χ_{BH}	χ_{NS}
SXS1	8.4	1.4	6.5	82	0.0	0.0
S1S2	5.2	1.4	4	56	0.8	0.45

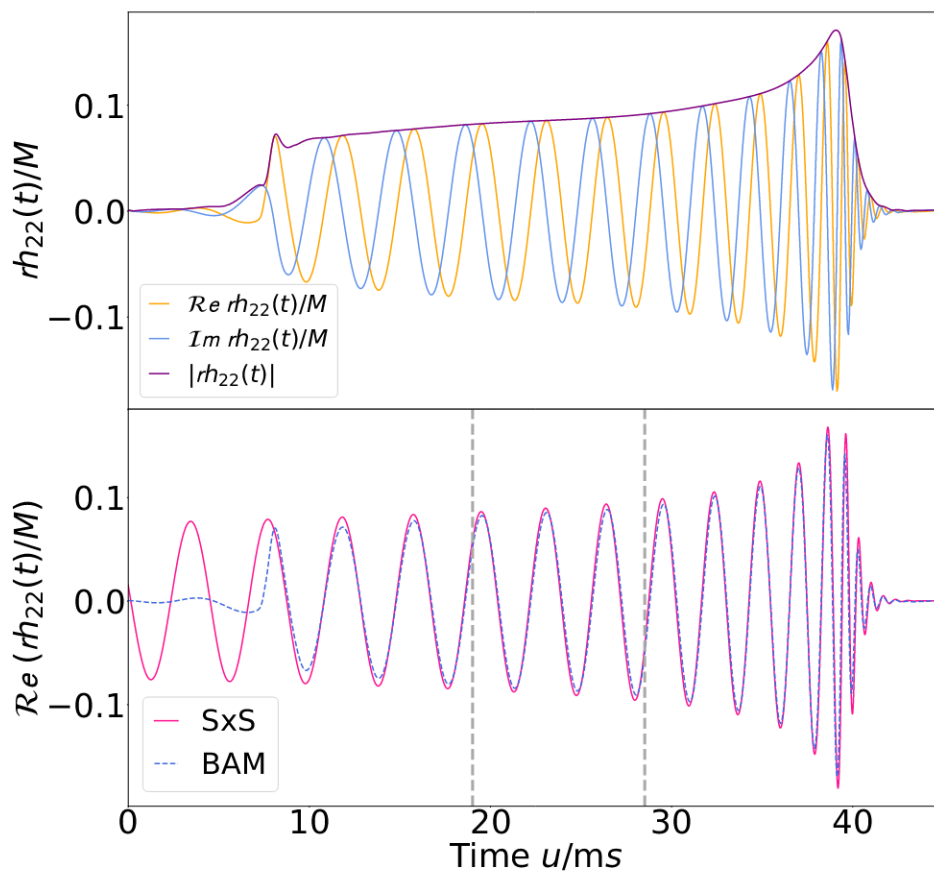


FIGURE 5.18: *Top*: Extracted gravitational wave strains (rh_{22}) for the $l = m = 2$ mode of the SXS1 system from table 5.3. *Bottom*: Comparison of rh_{22} between the SXS:BHNS:0001 system from *SXS Gravitational Waveform Database* n.d. (solid line) and the SXS1 system (dashed line). For visual clarity, only the real part of both strains ($\mathcal{R}e(rh_{22})$) is shown in the plot. The alignment interval is marked with the vertical dashed line. Waveforms in both panels are plotted against the retarded time u defined at Eq. (5.59) and M is the sum of the isolated BH and NS’s masses.

From Rashti et al., 2022

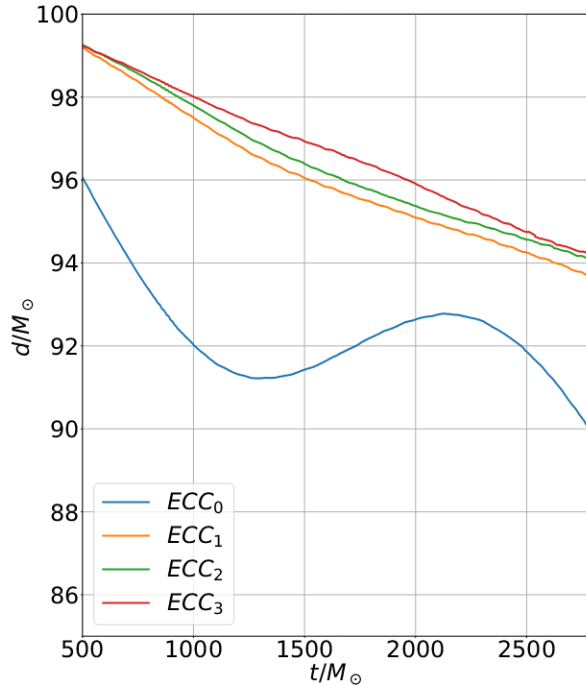


FIGURE 5.19: Proper distance (d) between BH and NS versus time (t) of the SXS1 system for different Ω_{BHNS} . After evolving for about 3 orbits the eccentricity reduction algorithm in Tichy et al., 2019 was used to adjust the angular velocity of the system Ω_{BHNS} and v_r . The eccentricity of each curve is as follows: $ECC_0 = 3.1 \times 10^{-2}$, $ECC_1 = 3.8 \times 10^{-3}$, $ECC_2 = 3.4 \times 10^{-3}$, and $ECC_3 = 9.0 \times 10^{-4}$. For the reduction we exclude the first $500M_\odot$ so that the required fits are not affected by the initial gauge adjustments.

From Rashti et al., 2022

visible in the plot. Moreover, the small wiggles around merger time are mostly due to the minimum of the lapse no longer being an appropriate indicator for the center of the NS within the routine tracking of the center of the compact objects (for better visualization of what happens around the time of the merger, see Fig. 5.21). The previously mentioned adjustment of the gauges is needed to transition between the excised BH, used in *Elliptica*, to the puncture approximation used in *BAM*. These effects can be seen in the plots in Fig. 5.22 and Fig. 5.23, where the violations of the Hamiltonian constraint, induced by excision are confined to the inner part of the BH and collapse in time towards the puncture, at the center of the BH itself. These plots, shaped on the line of Fig.4 in Chaurasia et al., 2021, are especially useful to verify that the violations of the Hamiltonian constraint do not propagate outwards, to the rest of the domain, from the inner BH region. At last, in Fig. 5.21, we show the last phases of the inspiral, up to the merger. In the plot, we show the different density profiles of the NS and the lapse for the BH only, as well as the corresponding AH found by the

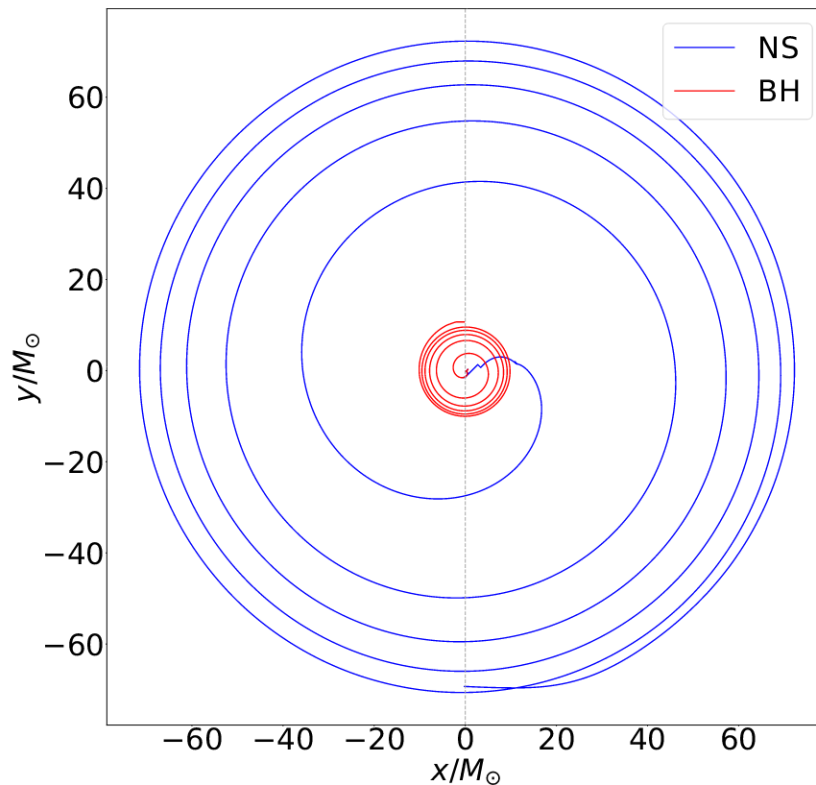


FIGURE 5.20: Trajectories of the NS (Blue trajectory) and the BH (Red trajectory) up until merger. The objects start their evolution aligned on the $x = 0$ axis (dashed line), as computed from `Elliptica`. The tracks follow the evolution of the minimum of the lapse relative to each object. The straight motion at the beginning of each trajectory is due to gauge adjustments.

From Rashti et al., 2022

code. To compare with the SXS collaboration catalog, we extracted the GW strain rh_{22} for the $l = m = 2$ mode and plotted it against the strain from the database in Fig. 5.18.

The waveforms in Fig.5.18 are plotted against the retarded time u calculated as

$$u = t - r_* = t - r_{extr} - 2M \ln(r_{extr}/2M - 1), \quad (5.59)$$

where r_{extr} is the extraction radius, set to $\sim 1500 M_\odot$, and M is the sum of the isolated BH and NS's masses. The plot shows good agreement between the aligned GW strains in the bottom plot, proving the accuracy of the evolution run.

Having proven the basic properties of the ID produced with `Elliptica` and validated the evolution of a relatively simple BHNS system, we move to a more complex system, in order to stress the capabilities of the ID code. We evolve the system `S1S2`,

where we have a lower mass ratio with respect to the previous test and a fully misaligned spin configuration for both objects, i.e. $\vec{\chi}_{BH} = (-0.46, -0.46, -0.46)$ and $\vec{\chi}_{NS} = (0., 0.32, 0.32)$. The high spin, in magnitude, of the two objects, together with the arbitrary direction, represents a challenge in terms of ID construction. The BH has spin of magnitude $\chi_{BH} = 0.8$ which is close to the maximum obtainable spin via `Elliptica`, and the NS has relatively high spin ($\chi_{NS} = 0.45$), since the break-up spin for NS is $\chi_{NS} \sim 0.7$. This system would theoretically lead to precessing orbits, where we would see the inclination of the orbital plane during the inspiral. In Fig. 5.24 we show the inspiral of the system in 2 and 3 dimensions to better visualize the precession, as well as the precessing cone, described by the precession motion (plus the nutation motion on top of that) of the orbital angular momentum L , perpendicular to the orbital plane. As expected, the run shows a precession motion of the orbital plane, due to the high spin of the two components. In general, we expect the BH spin to be the leading cause of the precession, due to the difference in mass between the objects, but the choice of a lower mass ratio, with respect to the `SXS1` test, grants that the contribution of the NS spin is not negligible.

The results shown above confirm the capability of the newly developed ID code on computing highly spinning compact objects with arbitrary orientations. The interest in similar systems is well known for BBH systems, due to the impact of precession on the GW signal (see, for example, Babak et al., 2017). Lately, this study has been extended to BNS mergers, exploring the parameter space in terms of different orientations, alignment with the orbital angular momentum, the magnitude of the spins, and the specific characteristics of the stars. With respect to BBH, the presence of detectable matter in NS poses an additional degree of freedom and opens up discussion about the effect of the NS composition on the two objects' interaction. Additionally, the fact that the NS mass distribution leads to a restricted range of possible mass ratios for the BNS system, ensures that in the case of two highly spinning components the effect of the two spins is considered co-dominant, and the orientation of the spins themselves plays a major role in the final outcome.

In light of this, we collaborated in the work of Chaurasia et al., 2020 about precessing the BNS system. In this work we simulated 7 different configurations, using multiple resolutions, stressing out the role of different orientations of NS spins. Due to the particular choice of the setups, five configurations have shown precession effects, developing, in particular, specific motions of two different types: a precession (*wobbling*)

of the orbital plane and a *bobbing* motion, i.e., no precession of the orbital angular momentum, while the orbital plane moves along the orbital angular momentum axis. This could be better visualized in Fig. 5.25, where the orbital dynamics and the GW emissions of the evolved setups are shown.

On the subject of the ejection of mass, we found that precessing systems can have an anisotropic mass ejection, which could lead to a final remnant kick of $\sim 40\text{km/s}$ (velocity that could be also due to GW emission) for the studied systems. Furthermore, for the chosen configurations, antialigned spins lead to larger mass ejecta than aligned spins, so brighter electromagnetic counterparts could be expected for these configurations. The effect on the ejecta poses a big question at the moment, and further studies on this topic might establish a distinct connection of the two phenomena, especially if and when supported by a joint detection of GW and EM counterparts. As a natural follow-up, extending this study now to BHNS systems is possible via the use of `Elliptica` for ID. As hinted already, BHNS systems differ from BNS systems, having a wide range of available mass ratios. Bounding systems to the low-end of the range allows the study of systems with properties similar to BNS systems. From the point of view of GW signal detection it is, in fact, already difficult to discern between the two systems in case of a low mass ratio BHNS: the behavior during the inspiral is comparable up to a certain precision, to the one of BNSs and a clear distinction is possible only after more detailed studies. We plan, for the near future, to further expand on the topic with more on-point results, possibly proposing a similar study to Chaurasia et al., 2020 for BHNS systems and expanding on the effects on the post-merger remnant.

As a next step into the analysis of compact binary mergers, we decided to make use of the resources developed so far to investigate the phenomenon of **Tidal Disruption**. Depending on the mass ratio of the binary components, BNS systems could present an extreme tidal deformation of the lighter of the two components, leading to the break-up of its structure and to a gradual accretion onto the more massive component. This phenomenon, known as tidal disruption, is much more common in BHNS binaries, where the variety of mass ratios is wider and the BH is the natural candidate for the disruption of the secondary. The onset of this phenomenon is represented by the *mass-shedding limit*, namely when the tidal force exerted by the BH overcomes the self-gravity of the NS at the inner edge of the stellar surface and mass starts to be accreted onto the BH (see for example Kyutoku et al., 2021 for more

details on the subject). To date, no clear-cut way of defining the tidal disruption limit has been found. Looking into different characteristics of the merger, it is possible to define a tidal disruption limit from the point of view of the GW signal: tidal modes are excited during the post-merger phase and are visible in the extracted GW strain. Another approach instead relies on Newtonian estimations and compares two critical scales of the BHNS system, i.e. the tidal separation or radius r_{tidal} and the radius of the Innermost Stable Circular Orbit (ISCO) around the BH r_{isco} (and dependent only on the properties of the latter). We then claim that a NS undergoes tidal disruption during the inspiral of a BHNS system if

$$r_{\text{tidal}} \gtrsim r_{\text{isco}}, \quad (5.60)$$

i.e. we have the onset of the disruption before entering the ISCO. This approach, developed in Foucart, 2012, can be also applied to GW signals by deriving the tidal frequency f_{tidal} from r_{tidal} and comparing it with f_{isco} , as in Pannarale et al., 2015. The expression for r_{tidal} can be derived from Newtonian's estimates of the mass shedding limit as

$$\frac{M_{NS}}{R_{NS}^2} \sim \frac{3M_{BH}}{r_{\text{tidal}}^3} R_{NS}, \quad (5.61)$$

from which we simply get

$$r_{\text{tidal}} \sim R_{NS} \left(\frac{3M_{BH}}{M_{NS}} \right)^{1/3} = R_{NS} (3q)^{1/3} \quad (5.62)$$

where $q = M_{BH}/M_{NS}$ is the mass ratio of the BHNS system.

Looking at the formulas so introduced, it is straightforward to deduce that disruption will be favored in the BHNS system with

1. low-mass BHs M_{BH} ;
2. BH spin aligned with the total orbital angular momentum;
3. large NS radii R_{NS} .

The ISCO radius r_{isco} can be calculated as in Bardeen et al., 1972, using

$$Z_1 = 1 + (1 - \chi_{BH}^2)^{1/3} [(1 + \chi_{BH})^{1/3} + (1 - \chi_{BH})^{1/3}], \quad (5.63)$$

$$Z_2 = \sqrt{3\chi_{BH}^2 + Z_1}, \quad (5.64)$$

$$r_{\text{isco}} = M_{BH} \left(3 + Z_2 - \text{sign}(\chi_{BH}) \sqrt{(3 - Z_1)(3 + Z_1 + 2Z_2)} \right). \quad (5.65)$$

We also define the normalized ISCO radius \hat{r}_{isco} and the normalized tidal radius \hat{r}_{tidal} as

$$\hat{r}_{\text{isco}} = \frac{r_{\text{isco}}}{M_{BH}}, \quad \hat{r}_{\text{tidal}} = \frac{r_{\text{tidal}}}{R_{NS}}, \quad (5.66)$$

that will be helpful in the following.

From the formula introduced before a model for the mass left gravitating around the BH in the form of a disk after the merger \hat{M}_{rem} has been developed in Foucart, 2012, and later modified and improved in Foucart et al., 2018b and in Foucart, 2020:

$$\hat{M}_{\text{rem}} = \frac{M_{\text{rem}}}{M_{NS}^b} = \left[\max \left(\alpha \frac{1 - 2C_{NS}}{\eta^{1/3}} - \beta \hat{r}_{\text{isco}} \frac{C_{NS}}{\eta} + \gamma, 0 \right) \right]^\delta, \quad (5.67)$$

where M_{NS}^b is the baryon mass of the NS and $C_{NS} = M_{NS}/R_{NS}$ is the compactness of the NS, which depends on the internal structure of the star determined by the EOS. The first term in Eq. (5.67) is proportional to the normalized tidal radius, defined in Eq. (5.66), multiplied by $(1 - 2C_{NS})$ to account for the fact that a BH cannot be tidally disrupted, i.e. has $C_{BH} = 1/2$. The second term in Eq. (5.67) scales as r_{isco}/R_{NS} as the mass ratio $q \rightarrow \infty$. Lastly, in Eq. (5.67), $(\alpha, \beta, \gamma, \delta)$ are free parameters determined by a global fit whose estimated values are

$$\alpha = 0.406, \quad \beta = 0.139, \quad \gamma = 0.255, \quad \delta = 1.761 \quad (5.68)$$

(see Foucart et al., 2018b).

By imposing $\hat{M}_{\text{rem}} \leq 0$ we ask for the remnant BH to have no disk around it, i.e. implying a direct plunge of the NS inside the BH. A $\hat{M}_{\text{rem}} \gtrsim 0$ would instead imply a tidal disruption.

In all the formulas introduced the variables at play are C_{NS} and \hat{r}_{isco} so, in turn, all the dependence is on χ_{BH} and M_{BH} , for the BH, and C_{NS} , which is dependent solely on the EOS for the NS.

To expand our knowledge on the topic, we decided to study the effect of NS spin χ_{NS}

on the system. In particular, we use Eq. (5.67) as a discriminant to study the effect of the NS spin on the tidal disruption, designing a set of runs whose parameters fulfill the relation $\hat{M}_{\text{rem}} = 0$, i.e. at the limit between tidal disruption and direct plunge, and then add aligned or anti-aligned spin to the NS to evaluate its effect. More concretely, we expect to see a deviation from the system lying on the line of constant mass ratio in Fig. 5.26, induced by the addition of NS spin to the system. In general, we know the spin of the NS to be a subdominant component in the characteristic of a BHNS system, in particular, because of the BH being the more massive component (apart from very extreme mass ratios, i.e. $q \lesssim 1$) and having a dominant role in terms of spin. The new tool developed for us will however allow more accurate studies, pushing the NS spin to the break-up limit, and evaluating the effect in case of zero spinning BH and/or low mass ratio. The effect of NS spin has only been partially studied in the literature, limited to a few cases of misaligned spin and a very low number of simulations, in general, exploring this part of the parameter space (see, e.g., Taniguchi et al., 2005; Ruiz et al., 2020).

We expect that the addition of even a small NS spin to a threshold case of BHNS inspiral will push the system distinctively towards one of the two types of mergers. To verify this we have computed different ID configurations with `Elliptica`, listed in Tab. 5.4, all respecting the condition $\hat{M}_{\text{rem}} \approx 0$. Each set of ID is characterized by a fixed EOS and then three cases, where the NS is either spinless, with aligned spin, or anti-aligned spin. We then evolved these systems with `BAM` and study the moment of merger for the different configurations. In Fig. 5.27 we show the trajectories for each of the runs in Tab. 5.4 up to the merger. We can see how the addition of spin already modifies the trajectory of the objects and the number of orbits during the inspiral. In particular, how anti-aligned spin relates to faster inspiral with respect to the spinless and aligned case.

A key feature of this work is to establish a way to distinguish between a tidal disruption and a direct plunge, even for threshold cases. In light of this, we studied the transfer of mass between the NS and BH at the latest stages of the merger. In particular, in Fig. 5.28 we show the baryon mass content M_b inside spheres of different radii, centered on the center of the NS (identified by the minimum of the lapse). As expected, the smaller the radius of the sphere, the smaller the fraction of the total NS mass contained inside of it. We can then observe how mass is transferred to the BH during the final stages of the merger, depending on how/when the mass contained inside spheres of different radius changes. For example, if the mass transfer is abrupt we can rule in

TABLE 5.4: Different systems evolved in the context of this project. For each run we fixed the irreducible BH mass $M_{BH} = 4.05$ and the irrotational NS gravitational mass to $M_{NS} = 1.35$, so that the mass ratio is $q = 3$. In order we have the BH dimensionless spin χ_{BH} , the NS dimensionless spin χ_{NS} , the NS spin parameter Ω_{NS} , the NS baryonic mass M_{NS}^b in M_{\odot} units, and the initial separation d in M_{\odot} units

EOS	χ_{BH}	χ_{NS}	Ω_{NS}	M_{NS}^b	d
Alf2	-0.0466	0.0	0.0	1.48768	50
Alf2	-0.0466	+0.189	+0.01	1.48768	50
Alf2	-0.0466	-0.192	-0.01	1.48768	50
H4	-0.3	+0.0	+0.0	1.46868	45
H4	-0.3	+0.211	+0.01	1.46868	45
H4	-0.3	-0.215	-0.01	1.46868	45
MS1b	-0.4	+0.0	+0.0	1.4675	50
MS1b	-0.4	+0.113	+0.005	1.4675	50
MS1b	-0.4	-0.117	-0.005	1.4675	50
SLy	+0.128	+0.0	+0.0	1.4946	35
SLy	+0.128	+0.156	+0.01	1.4946	35
SLy	+0.128	-0.161	-0.01	1.4946	35

favor of a direct plunge.

These results are parts of a work still in progress. We hope to more details about the topic at hand soon, possibly expanding the set of runs or studying more extreme cases.

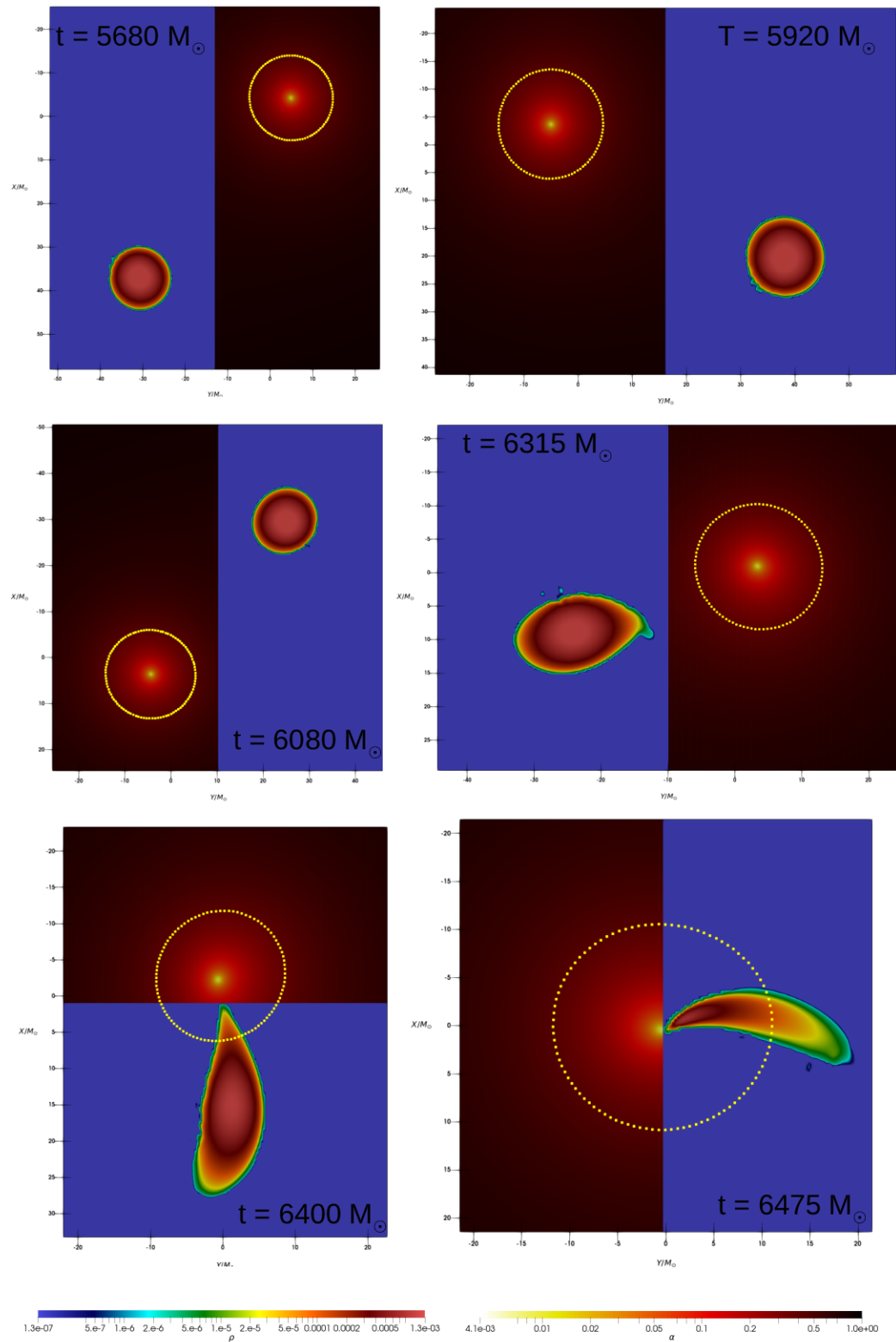


FIGURE 5.21: Snapshot of the last stages of the inspiral at different times. The plots are divided in order to show both objects at the same time: the NS represented by the density profiles, while the BH via the lapse, both expressed in logscale. The dotted line in Yellow represents the AH surrounding the BH.

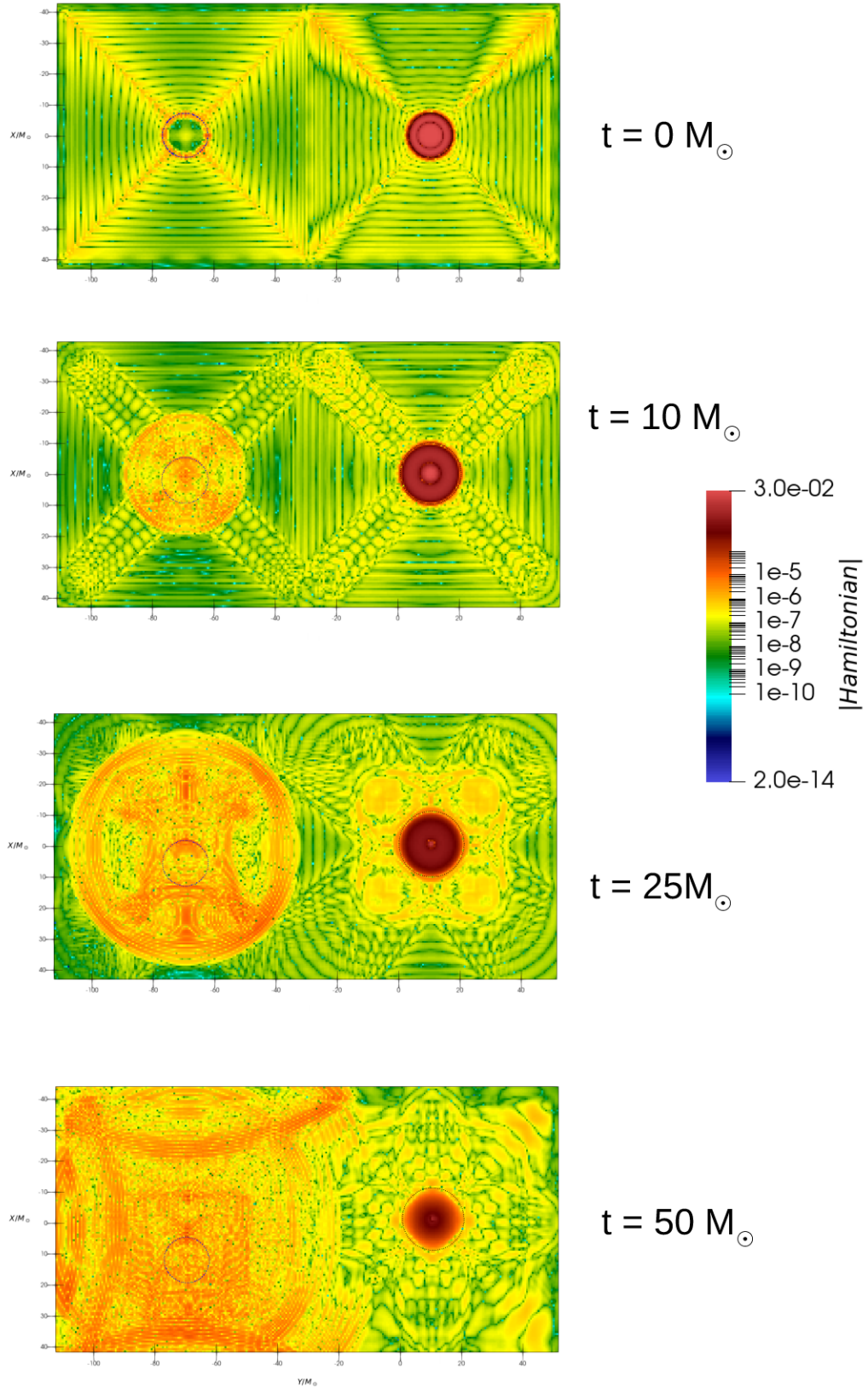


FIGURE 5.22: Hamiltonian constraint in log scale for the SXS1 system at different times in the first $50M_{\odot}$ of the run. The dotted black line (on the right) represent the AH of the BH and the dotted blue line (on the left) the NS surface.

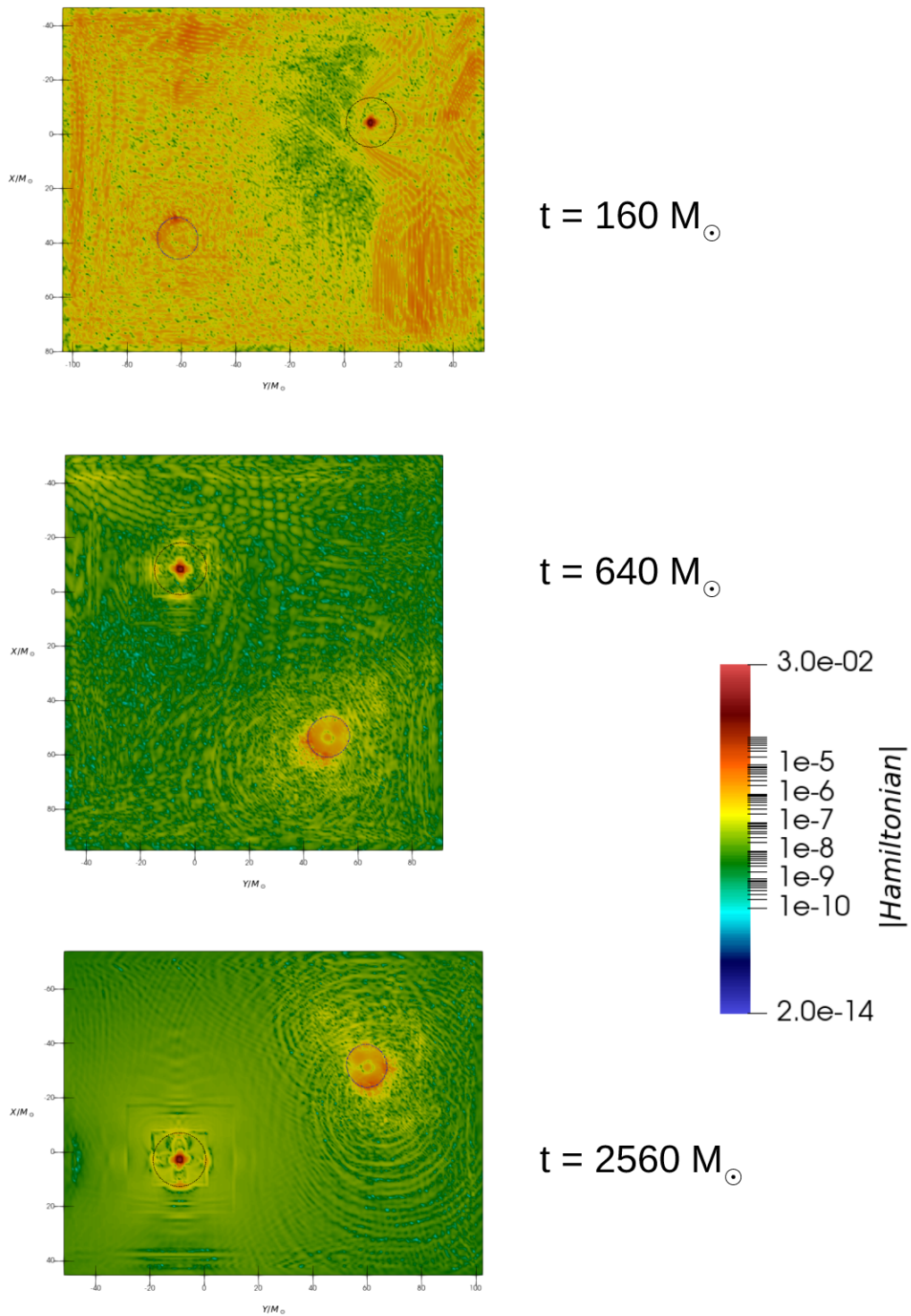
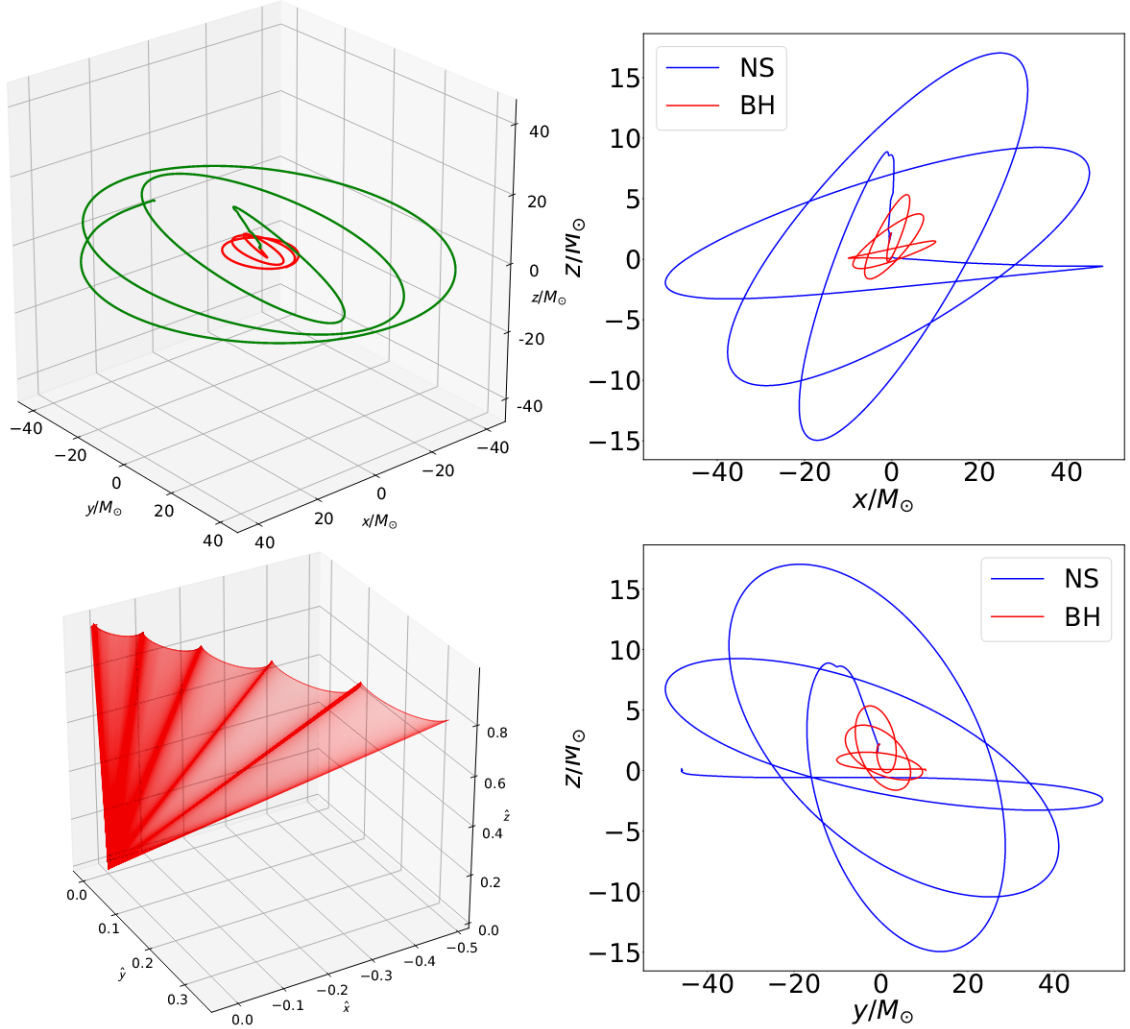


FIGURE 5.23: Same as Fig. 5.22 for different times, later in the run



(A) (*Top*) 3-D trajectories for the NS (Green trajectory) and the BH (Red trajectory). (*Bottom*) Precession cone, defined by the motion of the orbital angular momentum L . The oscillation visible at the edge of the cone describe the nutation motion. From Rashti et al., 2022

(B) 2-D trajectories for the NS (Blue trajectory) and the BH (Red trajectory) in the xz plane (*Top*) and in the yz plane (*Bottom*). Note that the ratio between the z -axis and the other axis is different from 1 in order to emphasize the precessing orbits.

FIGURE 5.24: 2-D and 3-D inspiraling and precessing trajectories of the NS and BH for the initial data S1S2. Here, $\vec{\chi}_{BH} = (-0.46, -0.46, -0.46)$ and $\vec{\chi}_{NS} = (0, 0.32, 0.32)$. From Rashti et al., 2022

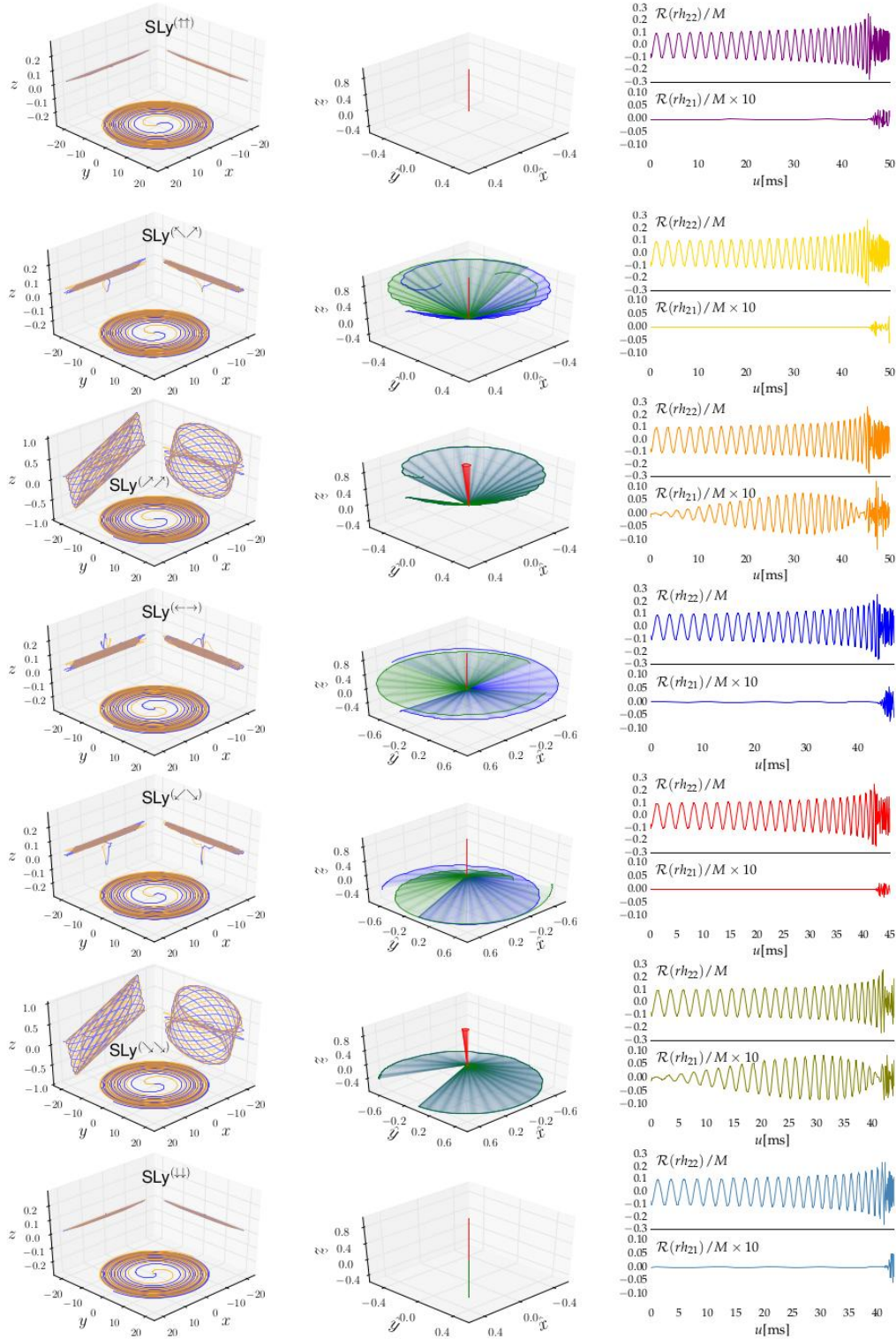


FIGURE 5.25: Orbital dynamics and GW emission for various NS spin configurations in BNS systems. **Column 1:** coordinate tracks of each NS in the binary. **Column 2:** precession cones of each binary. The spin evolution of the individual stars, in **Blue** and in **Green**, and the orbital angular momentum of the system, in **Red** are shown here. **Column 3:** (2,2)- and (2,1)-modes of the GW strain rh .

From Chaurasia et al., 2020

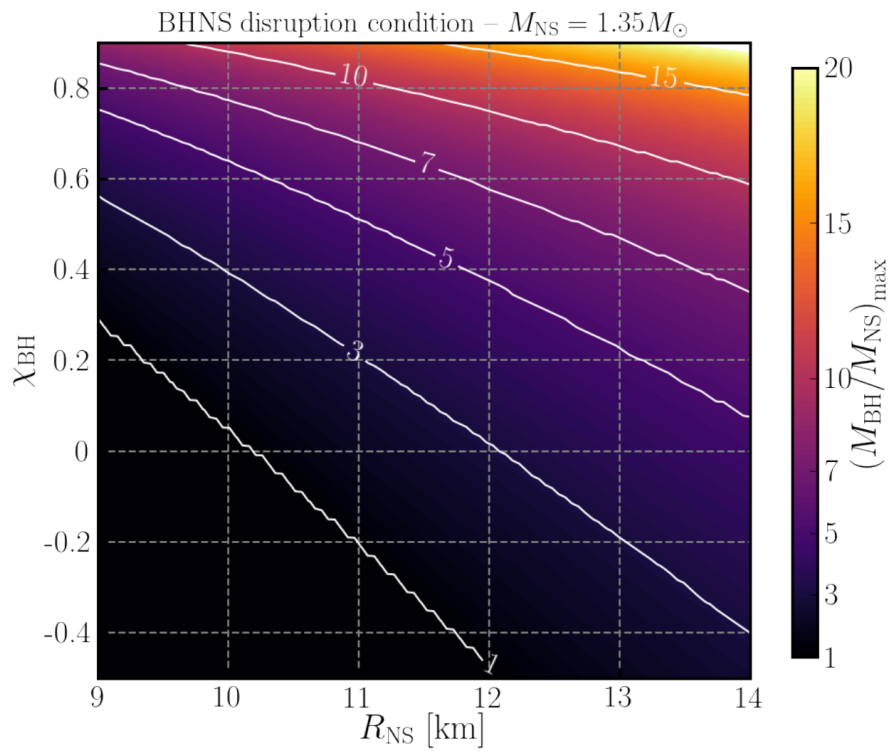


FIGURE 5.26: Maximum value of the mass ratio $M_{\text{BH}}/M_{\text{NS}}$ for which a BHNS system will disrupt as a function of the NS radius R_{NS} and aligned component of the dimensionless BH spin χ_{BH} , assuming $M_{\text{NS}} = 1.35M_{\odot}$ (from the study in Foucart et al., 2018b).
From Foucart, 2020

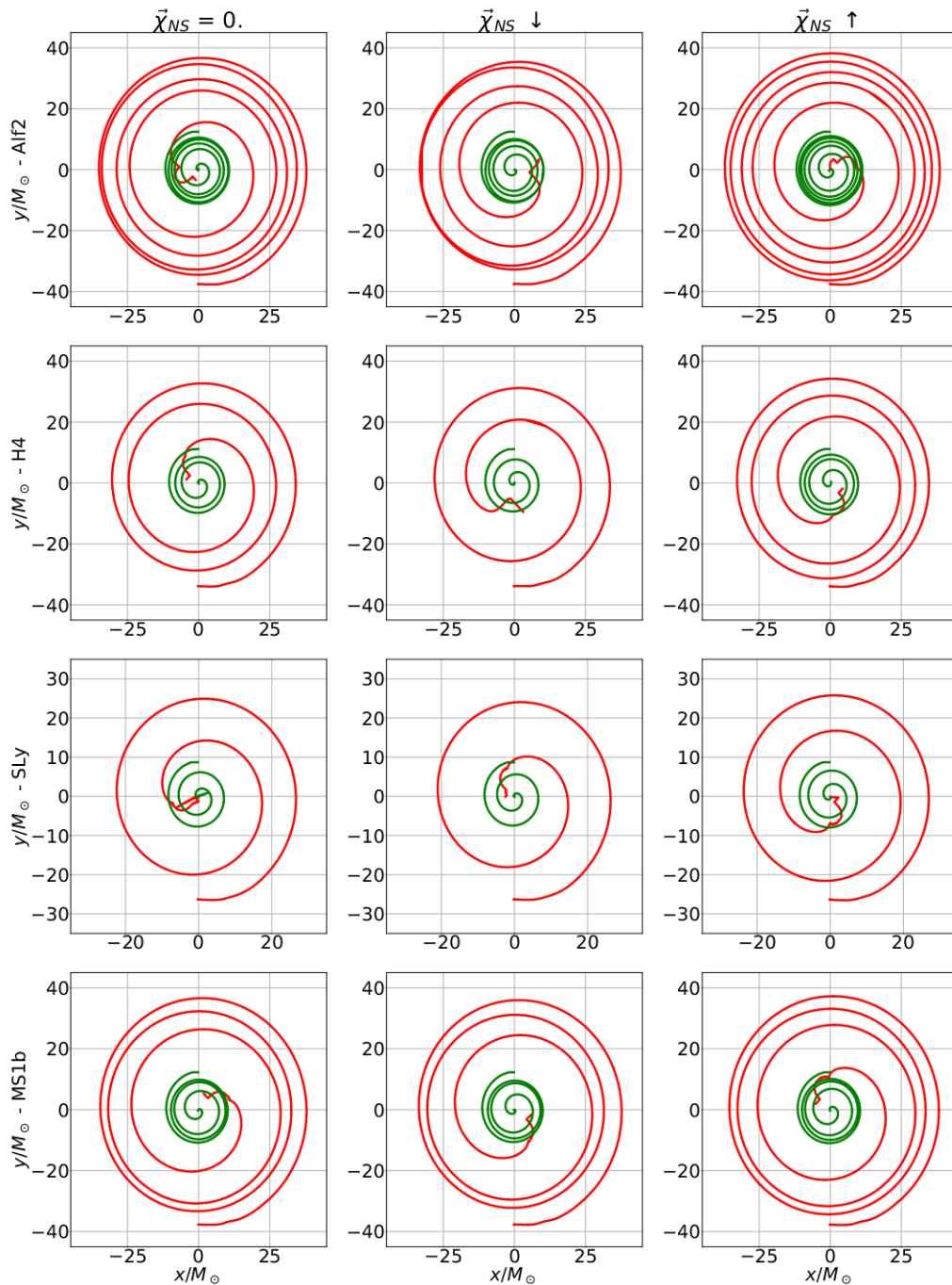


FIGURE 5.27: Trajectories of the inspiral of the runs in Tab. 5.4, grouped per EOS and NS spin (three cases: spinless $\vec{\chi} = 0.$, aligned spin $\vec{\chi} = \uparrow$, and anti-aligned spin $\vec{\chi} = \downarrow$). In **Green** the trajectories for the BH, and in **Red** the trajectories for the NS. The wiggling motion at the end of the inspiral is due to the minimum of the lapse no longer being an appropriate indicator for the center of the NS while this is being absorbed by the BH.

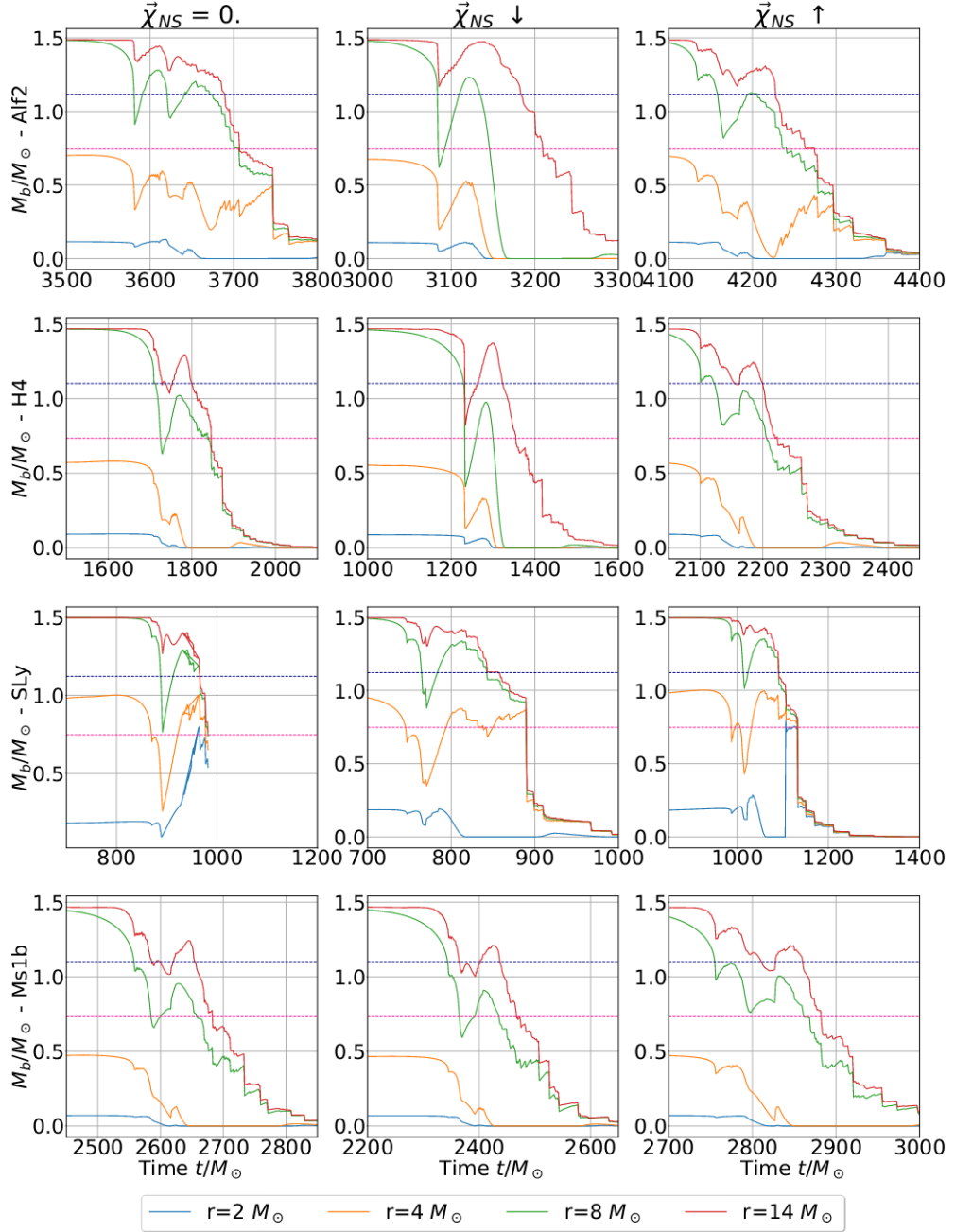


FIGURE 5.28: Baryonic mass contained inside spheres of fixed radii (in specific $r = 2, 4, 8, 14 M_{\odot}$), centered on the NS. The horizontal dashed lines represent 75% and 50% of the initial NS mass.

Chapter 6

Conclusions

In this thesis work, we have described different aspects of compact object simulations, from the effect of different physical aspects to the actual simulation of complex mixed binaries. We began by studying how to model the propagation of neutrinos, ejected during the merger of BNS systems. We developed a post-analysis tool able to evaluate the different properties of neutrino propagation from a hot remnant starting, in particular, from the temperature T of the matter in/around the remnant and the electron fraction Y_e , dependent on the matter properties described by the EOS.

We distinguished between two different optical depths, i.e. diffusion opacity κ_{diff} and equilibrium opacity κ_{eq} , each characterizing regions with different neutrino properties. By choosing 17 directions for each point of the domain outside the remnant (after filtering out the lowest density regions), we performed an approximate calculation of the opacities along the different paths from each point to the outer boundary. This way, we are able to set appropriate thresholds on the optical depth, to define two separate surfaces i.e. the diffusion surface and the equilibrium surface. Neutrinos enter the free-streaming regime after leaving the diffusion surfaces as they decouple from the background medium while leaving the equilibrium surfaces. By defining these different surfaces we are able to describe the behavior of neutrinos in the dynamical regions so obtained and infer the possible influence on the matter surrounding the remnant. Since the matter and EM ejecta are deeply influenced by weak interactions and r-processes, estimating the effect of neutrinos plays a key role in quantitative estimates of the emissions. Via the use of two different EOS, we were able to see how the neutrinospheres form and evolve, depending on the properties of the remnants. By distinguishing between three neutrino species (light neutrinos $\nu_e, \bar{\nu}_e$ and heavy neutrinos ν_x) we were able to determine the impact regions of different reactions around the remnant and the relative evolution of the latter. As a trend, we saw how diffusion surface relative to heavy neutrinos ν_x encapsulate the others. This relation is reversed

in the case of equilibrium surfaces. In general, diffusion surfaces form outside of equilibrium surfaces (when they are not approximately coincident), marking in-between regions where neutrinos diffuse for non-elastic scattering. For better visualization of the results and of the relative position of the regions described before, we point the reader to the plots in Sec 5.1. A clear dependency of the results on the choice of the energy estimate for the neutrinos and of the temperature T on the EOS is shown.

From a strictly computational point of view, we then worked on the backend of the **BAM** code, with the aim of extending its functionality to the inclusion of the treatment of magnetic fields. The final objective was to add a separate module, capable of handling the evolution of the full set of Ideal MagnetoHydroDynamic equations (i.e. GRMHD), which represent the extension of Maxwell's law for EM fields to GR with the ideal assumption of infinite conductivity $\sigma \rightarrow \infty$. In this approximation we can express the electric field \vec{E} in terms of the magnetic field \vec{B} , using it as the only EM variable. The key to implementation is the choice of the formulation to assure the vanishing of the divergence of the magnetic field $\nabla \cdot B$. We decided to adopt the *divergence cleaning* approach, a standard formulation that does not require modifications in the already present computational grid of **BAM**. Even if not considered the most performing approach, divergence cleaning grants results in simulating systems of single stars and binaries.

The results obtained in the context of this work are promising in the sense of the capability of integrating the equations with the already present **BAM** infrastructure and producing some standard example runs and tests. More work is needed to perfect the module and solve the computational problems still present in the code.

Lastly, we dived into the topic of mixed binary mergers, i.e. BHNS. These binary systems represent the latest addition to the list of GW detections by the **LIGO-VIRGO** Collaborations and raise interest in their peculiar physical properties. We discuss here the newly introduced **Elliptica** code, a multi-purpose pseudo-spectral code for the computation of compact objects ID. Great effort has been put into the development of the latter by our collaborators Alireza Rashti and Prof. Wolfgang Tichy. We developed a series of tests to evaluate all the different capabilities of the code, giving specific attention to the computation of mixed binary ID, BHNS, and notable extension of the code with respect to its predecessor (the **SGRID** code). We have then verified the convergence of the code itself across different resolutions and evolved sets

of ID with extreme configurations in terms of spin and orientations of the objects. In particular, we have pushed the runs up to the code's maximum capabilities in terms of spin, obtaining values close to the break-up spin for the NS, and relatively high values for the BH. To validate the spin treatment we have compared the data from the ID with 3.5 post-Newtonian (PN) approximation plus the next-to-next-to-leading order correction of spin-orbit (SO), finding good agreement. Before evolving the ID produced, we have also tested the compatibility of `Elliptica` on different machines and its adaptability to different architectures. Evolving then specific sets of ID, we compared the results obtained for a long inspiral with the SXS:BHNS:0001 example from the SXS collaboration's catalog, showing nice agreement in the GW signal of the inspiral+merger. In a separate test, we instead designed a system with a misaligned spin for both components, obtaining a precessing evolution of the binary as a priori expected.

As a follow-up project, based on the ID produced with `Elliptica` for `BAM` we decided to investigate the limit between tidal disruption and direct plunge in BHNS merger. In particular, we can see that from the literature a clear-cut way to discriminate between these two cases has yet to be found. Approximate formulas, based on parameters fit on catalogs of BHNS runs, have been developed but the quantities at play are only the (dimensionless) spin χ_{BH} , the BH mass M_{BH} and the compactness of the NS C_{NS} . We decided to investigate the effect of the NS spin on such formulas, studying any modification on the disruption/plunge behavior of the system after the addition of aligned/anti-aligned NS spin.

This project is a work in progress but promising results are presented in the text for the different sets of ID evolved.

Future Prospects

The results of the different works on the compact merger will benefit from further studies on the topic. In particular, we expect future efforts to address the following topics:

- `BAM`'s GRMHD implementation: the first priority is going to be the resolution of the present problems, possibly adopting a different `con2prim` routine. With that closure in mind, additional 1D and 2D stress tests can be implemented. The possibility of a different grid configuration, i.e. a staggered grid as in Giacomazzo et al., 2007, has already been discussed and could present an improvement in future stability and performance. Once the module has seen its completion,

reproducing BNS and BHNS merger runs already present in the literature will represent the needed step before exploring new physics.

- **Neutrinospheres:** to further test the capability of the code, an extended analysis of BNS runs, using a wider variety of EOSs and initial setups should be considered. Ejecta analysis codes can be linked to the post-analysis tools developed and further assess the impact of neutrinos on the post-merger matter/EM emissions.
- **Elliptica:** future works on the code will be directed into improving the spin treatment of compact objects, increasing the parallelization and overall reducing the runtime of the code, and the addition of the Kerr-Schild metric, better suited for spinning objects. With the latter, we hope to push the limits of the achievable BH spin to $\chi \sim 0.99$.
- **Mixed binaries - precession:** as described in Sec. 5.3 the development of the **Elliptica** code allows for expanded studies for BHNS precessing binaries. In particular, applying methods of study already conducted on BNS systems to BHNS systems seems a natural next step. Further exploring the parameter space, in terms of mass ratio and spin orientation will help understand the processes around the merger of such dense objects and the possible ejecta emissions.
- **Mixed binaries - tidal disruption:** although this work is still ongoing we are confident in the quality of the results already obtained and the oncoming ones. A future extension to the project would include the addition of different EOSs and, in general, the study of different setups, in terms of the BH dimensionless spin χ_{BH} and the mass ratio q . Pursuing a more in depth study of tidal disruption represents an interesting topic too. Deepening the understanding of this aspect via NS deformation's and NS mass distribution's study during the inspiral could enlarge our view on this complicated and debated point.

Appendix A

General notions about PDEs

A.1 Well-posedness

The concept of **well-posedness** was first introduced by Jacques Hadamard in Hadamard, 1902 and then largely applied for systems of PDEs. In general, considering an *Initial-Value Problem* (IVP) or *Cauchy problem* for which we have a PDE and appropriate boundary conditions (BCs), we say that the problem is well-posed if

1. A solution exists.
2. That solution exists.
3. The solution changes continuously with changes in data.

If we assume the first two conditions for a given IVP we can concentrate on the third requirements and its implications. For example if we take a system of PDEs of the form

$$\partial_t u = Pu, \tag{A.1}$$

with u n -dimensional vector and P an $n \times n$ matrix then if we can define a norm $\|\cdot\|$ for which

$$\|u(t, x)\| \leq Ae^{Bt}\|u(0, x)\|, \tag{A.2}$$

with A and B constant independent from initial data, then we show a limit in the growth of the solution itself and ensure well-posedness.

A.2 Character of PDEs

Establishing the character of a system of PDEs is important to get a quick understanding of its basic properties. To define such character we resort to the analysis

of the *principal symbol* of a PDE i.e. the highest order partial derivative terms of a polynomial form of the differential operator (*symbol*).

More rigorously let's take a linear differential operator of order m

$$P(x, D) = \sum_{|\alpha| \leq m} a_\alpha(x) D^\alpha, \quad (\text{A.3})$$

with $D_j = \frac{1}{i} \partial_{x^j}$, $X, Y = \mathbb{R}^n$, $n \in \mathbb{Z}_+$, $a_\alpha(x) \in C^\infty(X)$, α, β multi-indices and P diffeomorfism of order m on X . It is easy to extend this definition to a Riemannian manifolds defining similar concepts in local coordinates and check that the definitions are coordinate invariant.

We define the *symbol* of P as

$$\sigma(P)(x, \xi) \equiv \sum_{|\alpha| \leq m} a_\alpha(x) \xi^\alpha. \quad (\text{A.4})$$

This is a bijective mapping from differential operators to the polynomials of ξ with smooth coefficients. The *principal symbol* is now

$$\sigma_m(P)(x, \xi) \equiv \sum_{|\alpha|=m} a_\alpha(x) D^\alpha, \quad (\text{A.5})$$

so it corresponds to the higher order terms of $\sigma(P)$.

Thanks to this definition we can move on and describe the character of a system of PDEs as:

1. The system is **Elliptic** if $\sigma(P)$ is positive-definite i.e. the eigenvalues of $\sigma(P)$ are all non-zero and of same sign.
2. The system is **Parabolic** if $\sigma(P)$ is positive semi-definite i.e. the eigenvalues of $\sigma(P)$ are all non-zero but one and of same sign. In addition the rank of $\sigma(P)$ is equal to n .
3. The system is **Hyperbolic** if $\sigma(P)$ has all non-zero eigenvalues and $n - 1$ of the same sign.

For a simplified take on the problem, we can cast a general in-homogeneous second-order PDEs in the form

$$A(x, y)u_{xx} + 2B(x, y)u_{xy} + C(x, y)u_{yy} + D(x, y)u_x + E(x, y)u_y + F(x, y) = G(x, y), \quad (\text{A.6})$$

that is written in a form analogous to a quadratic formula. We can then study the character of the PDEs simply looking at the determinant:

$$\begin{aligned} B^2 - AC < 0 & \quad \mathbf{Elliptic} \rightarrow \text{e.g. Laplace equation,} \\ B^2 - AC = 0 & \quad \mathbf{Parabolic} \rightarrow \text{e.g. Wave equation,} \\ B^2 - AC > 0 & \quad \mathbf{Hyperbolic} \rightarrow \text{e.g. Heat equation.} \end{aligned}$$

These classifications greatly helps to visualize the behavior of complex PDEs systems: once the character is known we can model the key properties of the system comparing it with simpler examples of PDEs of the same character (like the one in the example before). In a more descriptive way we can say that Elliptic equations generally arise from a physical problem that involves a diffusion process that has reached equilibrium. Hyperbolic equations arise in connection with mechanical oscillators, such as a vibrating string, or in convection-driven transport problems and are able to support solutions with discontinuities like shock waves. Parabolic PDEs serve as a transition from the hyperbolic PDEs to the elliptic PDEs: they tend to arise in time-dependent diffusion problems, such as the transient flow of heat.

A.2.1 Hyperbolicity

Since the formulation in exam in this work are mainly of the hyperbolic character we are expanding on this notion. We can define additional properties of an hyperbolic system of PDEs P simply looking at the set of eigenvalues/eigenvectors of its principal symbol $\sigma_m(P)$. In particular the system P is said to be

1. **Weakly Hyperbolic** if $\sigma_m(P)$ has real eigenvalues but not a complete set of eigenvectors.
2. **Strongly Hyperbolic** if $\sigma_m(P)$ has real eigenvalues and a complete set of eigenvectors:

$$\sigma_m(P)e_i = \lambda_i e_i, \quad (\text{A.7})$$

with $i = 1, \dots, n$, e_i complete set of eigenvalues and λ_i the corresponding eigenvectors.

Additionally, we can distinguish two sub-classifications of strongly hyperbolic systems:

- (a) **Strictly Hyperbolic:** the eigenvalues of the principal symbol σ_m are not only real but are also distinct.

- (b) **Symmetric Hyperbolic:** if all the coefficient matrix a_α of σ_m are symmetric.

Both sub-cases imply strong hyperbolicity but not vice versa.

An important property of a strongly hyperbolic system that we are not demonstrating here, is that strong hyperbolic systems of PDEs are all also well-posed. This feature will prove important in our discussion on different formulations.

Appendix B

3+1 Evolution Equations

B.1 ADM Formalism

The first formalism historically developed is the **ADM formalism** (named after the authors R. Arnowitt, S. Deser, C.W. Misner) Arnowitt et al., 2008. The evolution equations that we will show in the following, and that were historically used more for simulations are the non-trivial rewriting of J. W. York York, 1979. The original ADM formulation comes in fact from the Hamiltonian formulation of general relativity and started from the field equations written in terms of the Einstein tensor $G_{\mu\nu}$ instead of $R_{\mu\nu}$.

From Eq. (2.57) and Eq. (2.58) we can derive the decomposition of Einstein equations (2.26) that represent the *ADM formulation of General Relativity*: skipping the calculations we obtain the set of equations

$${}^{(3)}R + K^2 - K_{ij}K^{ij} = 16\pi E, \quad (\text{B.1})$$

$$D_j(K^{ij} - \gamma^{ij}K) = 8\pi S^i, \quad (\text{B.2})$$

$$\partial_t \gamma_{ij} = -2\alpha K_{ij} + D_i \beta_j + D_j \beta_i, \quad (\text{B.3})$$

$$\begin{aligned} \partial_t K_{ij} = & -D_i D_j \alpha + \beta^k \partial_k K_{ij} + K_{ik} \partial_j \beta^k + K_{jk} \partial_i \beta^k + \\ & + \alpha ({}^{(3)}R_{ij} + K K_{ij} - 2K_{ik} K_j^k) + 4\pi \alpha (\gamma_{ij}(S - E) - 2S_{ij}), \end{aligned} \quad (\text{B.4})$$

with

$$S_{\mu\nu} = P_\mu^\alpha P_\nu^\beta T_{\alpha\beta}, \quad (\text{B.5})$$

$$S_\mu = -P_\mu^\alpha n^\beta T_{\alpha\beta}, \quad (\text{B.6})$$

$$S = \gamma^{\mu\nu} S_{\mu\nu}, \quad (\text{B.7})$$

$$E = n^\mu n^\nu T_{\mu\nu}, \quad (\text{B.8})$$

where $S_{\mu\nu}$ is the spatial stress tensor, S_μ is the momentum density, and E is the local energy density as measured by an Eulerian observer.

Let's briefly confront this set of equations with the original Einstein equations: Eq. (2.26) are a set of 10 equations for the components of $g_{\mu\nu}$. It is meaningful to split this set into two different parts. The first part is composed by Eq. (B.1) and Eq. (B.2). These 4 equations are called *constraints* because they do not contain time derivatives. Specifically we call Eq. (B.1) the **Hamiltonian constraint** and Eq. (B.2) the **Momentum constraint**.

The second part is instead composed by 6 equations, Eq. (B.4), and describes the evolution of the extrinsic curvature K_{ij} with a first-order expression, thanks to the relation in Eq. (B.3) between the first time derivative of the metric and the extrinsic curvature itself. It is important to notice that the time derivative of the lapse function α and shift functions β^a do not appear in the equations and for this reason, they're not dynamical variables but what is commonly called as *gauge variables*, associated with the choice of coordinates.

Although substantially important as a first result in terms of decomposition of the Einstein equations and the first simulations of Black Holes spacetimes, the ADM formalism has proven not to be stable nor robust for more long or complex simulations. It has been seen that oscillations of increasing amplitude start developing during the simulations. This behavior is due to the fact that ADM formulation is only *weakly hyperbolic* in terms of PDEs systems and in general *ill-posed*. For more details about well-posedness and hyperbolicity refer to Appendix A and in particular Sec. A.2.1. Depending on the choice of Gauge conditions the ADM formulation is written as well-posed. We refer to Sec. 2.3 for the possible Gauge choices. In the following, we are going to describe alternative 3 + 1 formulations which show better properties in terms of numerical simulations and are used up to the present day.

B.2 BSSNOK Formalism

From the difference between the original ADM formalism and the successive York formulation, it is clear that the 3 + 1 foliation of the spacetime is not unique but can be expressed by varying the form of the evolution equations by the addition of multiples of the constraint, without losing validity. The idea of this formalism was introduced first by Nakamura, Oohara, and Kojima (Nakamura et al., 1987) while the most used

version is based on the work of Shibata and Nakamura (Shibata et al., 1995), after being re-analyzed later by Baumgarte and Shapiro (Baumgarte et al., 1998a). The full name of the formulation is taken from the name of all the authors that contributed to it during the years but was initially referred to as "BSSN" or "conformal ADM" (more on this later). The aim was to develop a 3 + 1 decomposition that was more robust in terms of numerical computation (in fact is the most widely used formalism for Numerical Relativity). To do so new degrees of freedom were introduced, together with their evolution equations, to ensure stability to the new system of equations.

The main idea in this formulation (used also for other formulations like Bona-Maso or NOR) is to introduce three new independent quantities related to contractions of the connection or Christoffel symbols and then to modify the evolution equations for these quantities using the momentum constraints (B.2). The first thing we consider is a conformal rescaling of the spatial metric of the form

$$\hat{\gamma}_{ij} = \psi^{-4} \gamma_{ij}, \quad (\text{B.9})$$

where ψ is the conformal factor that can be chosen in a number of different ways (like *puncture method* for black holes or the introduction of an evolution equation for the scalar function that represents ψ initially).

Imposing now that the conformal metric has a unit determinant

$$\det(\hat{\gamma}_{ij}) = \hat{\gamma} = 1, \quad (\text{B.10})$$

we get

$$\hat{\gamma} = (\psi^{-4})^3 \gamma = 1, \quad (\text{B.11})$$

from which

$$\Rightarrow \psi = \gamma^{\frac{1}{12}}. \quad (\text{B.12})$$

We can also introduce ϕ as

$$\phi = \ln(\psi) = \frac{1}{12} \ln(\gamma). \quad (\text{B.13})$$

Then I have to separate the extrinsic curvature in a traceless part K and its trace

$$A_{ij} = K_{ij} - \frac{1}{3} \gamma_{ij} K, \quad (\text{B.14})$$

and its conformal rescaling

$$B_{ij} = \psi^{-4} A_{ij} = e^{-4\phi} A_{ij}. \quad (\text{B.15})$$

The crucial point is now to introduce three new variables called **conformal connection functions**

$$\hat{\Gamma}^i = \hat{\gamma}^{jk} \Gamma_{jk}^i = -\partial_j \hat{\gamma}^{ij}, \quad (\text{B.16})$$

where $\hat{\Gamma}_{jk}^i$ are the Christoffel symbols expressed in terms of $\hat{\gamma}_{ij}$.

At this point, we can underline that

$$\begin{aligned} \text{ADM} &\implies \gamma, K_{ij} \implies 12 \text{ variables} \\ \text{BSSNOK} &\implies \phi, \hat{\Gamma}, K, \hat{\gamma}, B_{ij} \implies 17 \text{ variables} \end{aligned}$$

Generally, in numerical computations the constraint

$$B = 0 \quad (\text{B.17})$$

is used to ensure more stability for simulations but here we present the full formulation with all 17 variables.

Now making use of the quantities that we redefined from the ADM formulation we get for the evolution equations

$$\frac{d}{dt} \hat{\gamma}_{ij} = -2\alpha B_{ij}, \quad (\text{B.18})$$

$$\frac{d}{dt} \phi = -\frac{1}{6} \alpha K, \quad (\text{B.19})$$

$$\frac{d}{dt} K = -D_i D^i \alpha + \alpha (B_{ij} B^{ij} + \frac{1}{3} K^2) + 4\pi \alpha (S + E), \quad (\text{B.20})$$

$$\begin{aligned} \frac{d}{dt} B_{ij} = e^{-4\phi} &\left[-D_i D_j \alpha + \alpha^{(3)} R_{ij} + 4\pi \alpha [\gamma_{ij} (S - E) - 2S_{ij}] \right]^{TF} \\ &+ \alpha (K B_{ij} - 2B_{ik} B_j^k), \end{aligned} \quad (\text{B.21})$$

$$\begin{aligned} \frac{d}{dt} \hat{\Gamma}^i = \hat{\gamma}^{jk} \partial_j \partial_k \beta^i &+ \frac{1}{3} \hat{\gamma}^{ij} \partial_j \partial_k \beta^k - 2B^{ij} \partial_j \alpha + \\ &+ 2\alpha (\hat{\Gamma}_{jk}^i B^{jk} + 6B^{ij} \partial_j \phi - \frac{2}{3} \hat{\gamma}^{ij} \partial_j K - 8\pi e^{4\phi} S^i), \end{aligned} \quad (\text{B.22})$$

that compose the **BSSNOK formulation**. Here TF stands for the Trace-Free part and we used the notation

$$\frac{d}{dt} \equiv \partial_t - \mathcal{L}_{\vec{\beta}}. \quad (\text{B.23})$$

The key element to obtain Eq. (B.22) is the use of momentum constraints to modify the evolution equations for $\hat{\Gamma}^i$. To complete the set of equations of BSSNOK we have to add the set of constraints of the ADM formulation (B.1) and (B.2).

We need to express the Ricci tensor associated with the new choice of metric as

$${}^{(3)}R_{ij} = {}^{(3)}\hat{R}_{ij} + {}^{(3)}R_{ij}^\phi, \quad (\text{B.24})$$

where \hat{R}_{ij} is the part of the Ricci tensor associated with the conformal metric $\hat{\gamma}_{ij}$ and R_{ij}^ϕ the additional terms of R that depend on ϕ , both expressed in the following

$$\begin{aligned} {}^{(3)}\hat{R}_{ij} = & -\frac{1}{2}\hat{\gamma}^{lm}\partial_l\partial_m\hat{\gamma}_{ij} + \frac{1}{2}(\hat{\gamma}_{ki}\partial_j\hat{\Gamma}^k + \hat{\gamma}_{kj}\partial_i\hat{\Gamma}^k) \\ & + \frac{1}{2}(\hat{\Gamma}^k\hat{\Gamma}_{ijk} + \hat{\Gamma}^k\hat{\Gamma}_{jik}) + \hat{\gamma}^{lm}(\hat{\Gamma}_{li}^k\hat{\Gamma}_{jkm} + \hat{\Gamma}_{lj}^k\hat{\Gamma}_{ikm} + \hat{\Gamma}_{im}^k\hat{\Gamma}_{klj}), \end{aligned} \quad (\text{B.25})$$

$${}^{(3)}R_{ij}^\phi = -2\hat{D}_i\hat{D}_j\phi - 2\hat{\gamma}_{ij}\hat{D}^k\hat{D}_k\phi + 4\hat{D}_i\phi\hat{D}_j\phi - 4\hat{\gamma}_{ij}\hat{D}^k\phi\hat{D}_k\phi, \quad (\text{B.26})$$

where \hat{D}_i is the covariant derivative associated with the conformal metric.

It is important to point out that the Lie derivatives in Eq. (B.23), computed along $\vec{\beta}$, are used on so-called *tensor densities* i.e. tensors multiplied by powers of the determinant of the metric γ .

If we multiply a tensor for $\gamma^{n/2}$ we obtain what we define as a tensor density of weight n . The Lie derivative of such object is given by

$$\mathcal{L}_{\vec{\beta}}T = \mathcal{L}_{\vec{\beta}}T|_{n=0} + nT\partial_i\beta^i. \quad (\text{B.27})$$

In our formulation we have

$$\begin{aligned} \psi & \implies n = 1/6, \\ \hat{\gamma}_{ij} & \implies n = -2/3, \\ B_{ij} & \implies n = -2/3, \end{aligned}$$

and

$$\mathcal{L}_{\vec{\beta}}\phi = \beta^k\partial_k\phi + \frac{1}{6}\partial_k\beta^k, \quad (\text{B.28})$$

$$\mathcal{L}_{\vec{\beta}}\hat{\gamma} = \beta^k\partial_k\hat{\gamma}_{ij} + \hat{\gamma}_{ik}\partial_j\beta^k + \hat{\gamma}_{jk}\partial_i\beta^k - \frac{2}{3}\hat{\gamma}_{ij}\partial_k\beta^k. \quad (\text{B.29})$$

Finally, we need to mention that we can add a parametric term in the momentum constraints to develop different versions of the BSSNOK formulation (the one presented here is just the standard formulation) but we must be careful to not lose the strong hyperbolicity character of the equation. BSSNOK formulation has in fact the advantage, with respect to ADM, to be strongly hyperbolic (refer to Appendix A for a definition), properties that ensure stability during long evolution.

Regardless of its early introduction, the BSSNOK formulations pertains its importance in the community, being one of the mostly used formalisms employed. The BAM code, used for this work and described in Sec. 4.2.1 is employing this formalism.

B.3 Z4 Formalism

Previous formulations of 3+1 decomposition were based on ADM and used momentum constraint to modify evolution equations of new independent quantities. They were introduced using the spatial metric γ_{ij} or its time derivatives.

The Z4 approach was proposed in Bona et al., 2003; Bona et al., 2004 and is based on the introduction of a 4-vector to rewrite Einstein equations like:

$$R_{\mu\nu} + \nabla_{\mu}Z_{\nu} + \nabla_{\nu}Z_{\mu} = 8\pi\left(T_{\mu\nu} - \frac{1}{2}g_{\mu\nu}T\right), \quad (\text{B.30})$$

obtained from (2.26) using the relation between traces:

$$R = -8\pi T. \quad (\text{B.31})$$

To be coherent with the physical formulation we have to assume that Z_{μ} vanishes for every physical solution i.e. we add the constraint:

$$Z_{\mu} = 0. \quad (\text{B.32})$$

Einstein's equations can be written as:

$$\frac{d}{dt}\gamma_{ij} = -2\alpha K_{ij}, \quad (\text{B.33})$$

$$\frac{d}{dt}K_{ij} = -D_i\beta_j + \alpha[{}^{(3)}R_{ij} + D_iZ_j + D_jZ_i - 2K_{im}K_j^m + (K - 2\Theta)K_{ij}], \quad (\text{B.34})$$

$$\frac{d}{dt}\Theta = \frac{\alpha}{2}[{}^{(3)}R + (K - 2\Theta)K - K_{mn}K^{mn} + 2D_mZ^m - 2Z^m\partial_m \ln \alpha], \quad (\text{B.35})$$

$$\frac{d}{dt}Z_i = \alpha[D_mK_i^m - D_iK + \partial_i\Theta - 2K_i^mZ_m - \Theta\partial_i \ln \alpha], \quad (\text{B.36})$$

where we used the notation in (B.23) and we introduced the scalar Θ as the projection of the 4-vector Z_μ along the normal to the hypersurface n^μ

$$\Theta \equiv n_\mu Z^\mu = \alpha Z^0, \quad (\text{B.37})$$

Looking at Eq. (B.33) - (B.36) we see that they compose a set of 10 dynamical equations, with no constraints relation. As a consequence we have the conservation of general covariance in numerical simulations, due to the fact that we need to use all the sets for the evolution of spacetime, leaving no space for free relations.

As constraint, we have the four algebraic relations given by:

$$Z_\mu = 0 \longrightarrow \begin{cases} \Theta = 0 \\ Z_i = 0 \end{cases}. \quad (\text{B.38})$$

Taking the trace of (B.30) we have

$$\nabla_\mu Z^\mu = -\frac{1}{2}R - 4\pi T, \quad (\text{B.39})$$

while taking now the 4-divergence of Eq. (B.30) and using conservation of stress-energy and Einstein tensor we can derive the relation

$$\nabla^\nu \nabla_\nu Z^\mu + R_{\mu\nu}Z^\nu = \square Z_\mu + R_{\mu\nu}Z^\nu = 0, \quad (\text{B.40})$$

which describe the deviation of Eq. (B.30) from (2.26): in particular it shows that any discrepancy propagates through light-cones and puts constraints on the evolution of

the set of initial data:

$$Z_\mu(0, x^i) = 0, \quad (\text{B.41a})$$

$$\partial_t Z_\mu(0, x^i) = 0. \quad (\text{B.41b})$$

Here Eq. (B.41b), together with Eq. (B.35) and (B.36) represent momentum/energy constraints of the previous formulations. To complete the evolution system is mandatory to provide a coordinate condition to fix the kinematic degree of freedom.

The Z4 equation can be reformulated in damped form, in such a way that the general solutions are driven towards Einstein solutions. Introducing the parameters κ_1 κ_2 as free coefficients we have

$$R_{\mu\nu} + \nabla_\mu Z_\nu + \nabla_\nu Z_\mu + \kappa_1 [n_\mu Z_\nu + n_\nu Z_\mu - (1 + \kappa_2) g_{\mu\nu} n_\sigma Z^\sigma] = 8\pi \left(T_{\mu\nu} - \frac{1}{2} g_{\mu\nu} T \right), \quad (\text{B.42})$$

with the constraint-propagation system

$$\nabla^\nu \nabla_\nu Z^\mu + R_{\mu\nu} Z^\nu = -\kappa_1 \nabla^\nu [n_\mu Z_\nu + n_\nu Z_\mu + \kappa_2 g_{\mu\nu} n_\sigma Z^\sigma], \quad (\text{B.43})$$

provided with the conditions for damping

$$\kappa_1 > 0, \quad (\text{B.44})$$

$$\kappa_2 > -1. \quad (\text{B.45})$$

In this way Eq. (B.33) - (B.36) can be rewritten as

$$\frac{d}{dt}\gamma_{ij} = -2\alpha K_{ij} \quad (\text{B.46})$$

$$\begin{aligned} \frac{d}{dt}K_{ij} = & -D_i\beta_j + \alpha[{}^{(3)}R_{ij} + D_iZ_j + D_jZ_i - 2K_{im}K_j^m + \\ & + (K - 2\Theta)K_{ij} - \kappa_1(1 + \kappa_2)\Theta\gamma_{ij}] - \\ & - 8\pi\alpha[S_{ij} - \frac{1}{2}(S - E)\gamma_{ij}], \end{aligned} \quad (\text{B.47})$$

$$\begin{aligned} \frac{d}{dt}\Theta = & \frac{\alpha}{2}[{}^{(3)}R + (K - 2\Theta)K - K_{mn}K^{mn} + \\ & + 2D_mZ^m - 2Z^m\partial_m \ln \alpha - 2\kappa_1(2 + \kappa_2)\Theta - 16\pi E], \end{aligned} \quad (\text{B.48})$$

$$\begin{aligned} \frac{d}{dt}Z_i = & \alpha[D_mK_i^m - D_iK + \partial_i\Theta - 2K_i^mZ_m - \\ & - \Theta\partial_i \ln \alpha - \kappa_1Z_i - 8\pi S_i]. \end{aligned} \quad (\text{B.49})$$

Appendix C

Conservative Formulations

To give an insight into the concept of conservative formulations we first point the reader to the equations introduced in Ch. 3. Let's start by expressing Eq. 3.9 and Eq. 3.10 in a compact matrix-form:

$$\partial_t \vec{U} + \vec{A} \cdot \vec{\nabla} \vec{U} = \vec{S}. \quad (\text{C.1})$$

Moreover \vec{A} is a function of \vec{U} , $\vec{A} = \vec{A}(\vec{U})$, and \vec{S} represents the source terms.

If the system of equations matches the conditions required for hyperbolicity, described in Sec. A.2.1, it represents a suitable set for numerical simulations. Moreover if $\vec{A}(\vec{U})$ is the Jacobian of the flux-vector $\vec{F}(\vec{U})$ with respect to \vec{U} i.e.

$$\vec{A}(\vec{U}) = \frac{\partial \vec{F}}{\partial \vec{U}}, \quad (\text{C.2})$$

then the homogeneous version of Eq. (C.1) can be written in what is defined as a **conservative form**

$$\partial_t \vec{U} + \vec{\nabla} \vec{F}(\vec{U}) = 0, \quad (\text{C.3})$$

where \vec{U} takes now the name of **state vector of conserved variables**.

What are the advantages of using a conservative form?

The answer to this question is simply given by the **Lax-Wendroff Theorem** (see Lax et al., 1960) which states that:

A hyperbolic system of conservation laws, approximated by a numerical scheme, if convergent, do converge to a weak solution of the system.

Weak solutions are particularly important dealing with **Riemann Problems** and discontinuities. Such discontinuities are often due to the formation of shocks, in the context of numerical simulations.

To define a weak solution we take the 1D form of Eq. (C.3)

$$\partial_t \vec{U} + \partial_x \vec{F} = 0, \quad (\text{C.4})$$

and then, by multiplying it for a test function ϕ with a compact support, we can pass to the integral form

$$\int_0^\infty \int_{-\infty}^{+\infty} (\phi \partial_t \vec{U} + \phi \partial_x \vec{F}) dx dt = 0. \quad (\text{C.5})$$

Integrating by part the first term in time and the second in space we get

$$\int_0^\infty \int_{-\infty}^{+\infty} (\vec{U} \partial_t \phi + \vec{F} \partial_x \phi) dx dt = - \int_{-\infty}^{+\infty} \phi(x, 0) \vec{U}(x, 0) dx, \quad (\text{C.6})$$

that is called what is referred to as a **weak formulation**. Now if a function \vec{U} satisfy the relation in Eq. (C.6) for every function ϕ is called a weak solution.

In practice, we obtained an alternative integral formulation in order to rewrite a differential equation in a form that would admit also non-smooth “solutions”, i.e. shocks and discontinuities.

To conclude, the theorem states that if a conservative formulation is used, then we are guaranteed that the numerical solution will converge to the correct one, while if a conservative formulation is not used, we are guaranteed to converge to the incorrect solution in the likely event in which the flow develops a discontinuity (for the latter see Hou et al., 1994). The concept of *convergence* mentioned before can be more extensively expressed. However before getting to conservation we have to define **consistency** and **stability**.

For a generic system of Partial Differential Equation in the form

$$\vec{P}(\vec{U}) = \vec{F}, \quad (\text{C.7})$$

described by a given grid-scheme $(\Delta t, \Delta x)$, such that the system in Eq. (C.7) becomes

$$P_k(U_i^n) = F_k, \quad (\text{C.8})$$

we can say that the scheme is *consistent* if

$$\epsilon_k = \vec{P}(\vec{U}) - P_k(U_i^n) \longrightarrow 0, \quad \text{for} \quad \Delta t, \Delta x \rightarrow 0 \quad (\text{C.9})$$

where ϵ_k is called a truncation error. So basically if the truncation error goes to zero in the limit of vanishing grid-spacing the scheme is said to be consistent and the solutions of the scheme's equation approach the true PDE's solutions.

Using the definition of discretized norm, we get

$$\|f(x, t)\|_p = \left(\frac{1}{b-a} \int_a^b |f(x, t)|^p dx \right)^{\frac{1}{p}} \quad (\text{C.10})$$

for a smooth function $f(x, t)$ in the interval (a, b) .

Now for the scheme $P_k(U_i^n) = 0$, if a constant C exists such as

$$\|U^n\|_2 \leq C \|U^0\|_2, \quad (\text{C.11})$$

for $0 \leq n\Delta t \leq T$, with $\Delta x, \Delta t \rightarrow 0$ then the scheme is said to be **stable**. Stability then ensures that the errors decay during evolution from one time step to the other (if time is the referring dimension).

Finally, we have that if

$$\lim_{\Delta x, \Delta t \rightarrow 0} \vec{U}(x_i, t^n) - U_i^n = \lim_{\Delta x, \Delta t \rightarrow 0} C(\Delta x, \Delta t)^p = 0, \quad (\text{C.12})$$

then the system is said to be **convergent** which ensures the convergence to the true solution of the PDE and p is the *convergence order*. By making use of the concept of stability and consistency we have the **Lax-Richtmyer Theorem** that can be simply expressed by the relation:

$$\text{consistency} + \text{stability} \iff \text{convergence} \quad .$$

Appendix D

Equations of State

Equations of State (EoS) represent a very complex matter in hydrodynamics and, especially, in compact object simulations. In fact, unless we are studying BH, for which we are prevented from modeling the inner part by the presence of an Event Horizon (EH), objects like white dwarfs or neutron stars pose a challenge to nuclear physicists in terms of descriptions of their internal structure (see Fig. D.1). Apart from its fundamental role in describing the matter property of the fluid in exam, we need to specify an equation of state of the form $p = p(\rho_0, \epsilon)$ in order to close the system of hydrodynamic equations.

The simplest choice we can make for an equation of state is to say that the pressure vanishes, i.e. $p = 0$ which represents a **dust fluid**. This is a strong approximation but it becomes helpful in some special cases. This fluid doesn't correspond exactly to the common concept of dust from everyday life. In particular, dust can be used to model a collection of cold collision-less particles, such as a uniform matter distribution in cosmology, the structure of rotating rings or disks of particles, or the collapse of a shell of matter initially at rest. A more precise but still intuitive approximation is the one of an **ideal gas**. It is important to mention that the terms *perfect fluid* and *ideal gas*, though similar, refer in fact to different things. A perfect fluid is defined as one with no viscosity and no heat conduction, but the equation of state can still be very general. An ideal gas, on the other hand, refers to a specific equation of state of the type

$$p = (\gamma - 1)\rho_0, \quad (\text{D.1})$$

where γ is a constant known as the adiabatic index (not to be confused with the determinant of the spatial metric in the text).

$$pV = nkT \quad (\text{D.2})$$

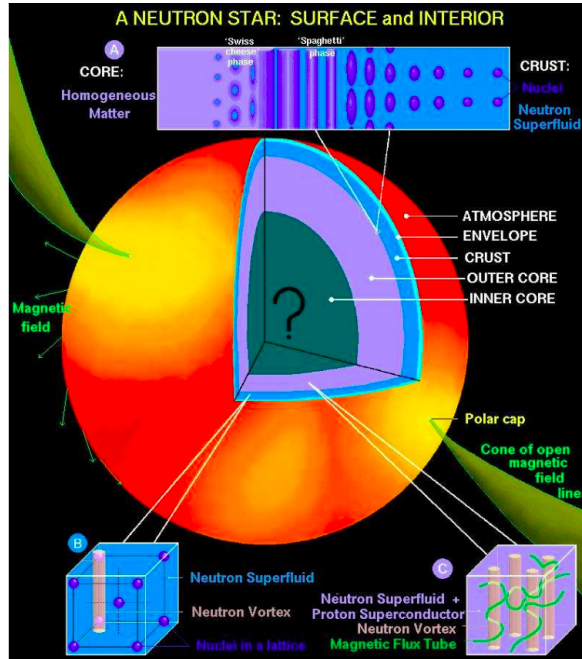


FIGURE D.1: Graphical design describing the interior of a NS and its matter content. The different layers show the change in behavior of the NS matter passing from the better known crust to still unclear composition of the inner core. Art made by Dany Page

where V is the volume, n the number of particles, T the temperature and k the Boltzmann constant. From the definitions of specific heat of a fluid

$$c_p = \frac{1}{M} \left(\frac{dQ}{dt} \right)_p, \quad (\text{D.3})$$

$$c_V = \frac{1}{M} \left(\frac{dQ}{dt} \right)_V, \quad (\text{D.4})$$

we get the definition of γ as

$$\gamma \equiv \frac{c_p}{c_V}. \quad (\text{D.5})$$

Another very common choice that is closely related to the ideal gas case is the so-called **Polytropic Equation of State** that has the form

$$p = K \rho_0^\Gamma \equiv K \rho_0^{1+1/N}, \quad (\text{D.6})$$

where K is a constant and N is called the polytropic index and the parameter $\Gamma \equiv 1 + 1/N$ is called the adiabatic index of the polytrope. However, we must remember that Γ and γ represent the same quantity only in the case of an adiabatic process involving an ideal gas. Nevertheless, polytropic EOS or polytropes are used even when

there is heat exchange, so the two indices are not entirely equivalent and in the general case, Γ will not correspond to the true adiabatic index.

As an example, in the particular case of cold compact objects such as white dwarfs and neutron stars, we can not use the ideal gas equation of state discussed above since it only applies to classical gases and does not describe correctly a highly degenerate Fermi gas. However, we can derive an equation of state for an ideal Fermi gas at zero temperature that reduces to a polytropic form both in the non-relativistic and extremely relativistic limits, with $\gamma = 5/3$ and $4/3$ respectively. More generally, polytropic equations of state with an adiabatic index in the range $1 < \gamma < 3$ can be used as very simple models of NS made of non-ideal Fermi gases. High values of γ result in **stiff** equations of state, and low values in **soft** equations of state. In fact, it can be shown that for a fixed ratio of pressure to density p/ρ_0 , large values of the adiabatic index γ correspond to a large speed of sound (i.e. a *stiff* fluid), while low values of γ correspond to a low speed of sound (i.e. a *soft* fluid). We can picture a NS with a stiff EOS to be harder to squeeze so its radius will be higher than a NS of the same mass but a soft EOS, where the internal structure permits the star to be more compressed. A way to improve the polytropic treatment of the matter is to adopt the so-called **Piecewise-Polytropes** EOS: we split the internal structure inside the NS into different N pieces, each of which has different parameters (K_i, Γ_i) . This allows a more precise approximation of the interior of the neutron star: usually, 3 pieces are used for the split to represent the crust, the mantle, and the core of the NS (see Fig. D.1). Increasing N we also increase the precision of the treatment. We can write the expression of $p(\rho)$ as

$$p(\rho) = K_i \rho^{\Gamma_i}, \quad (\text{D.7})$$

with $i = 0, \dots, N$.

The true equation of state for neutron stars is still largely unknown owing to our lack of knowledge of the interactions of nuclear matter at very high densities.

The NS internal structure represents a great unknown in the field. Several studies are refining models to describe the effect of such high densities on the matter (often called *exotic matter* for having properties going beyond the usually studied systems, see Fig. D.2), accounting for quantum effect and strong force. Deriving more and more reliable approximation for the inner structure is a complex subject and we are not going to enter the details of the matter here. For the sake of complicity we point the reader to results obtained in the context of nuclear physics and the theoretical constraints to the determination of NS's EOS in Fig. D.3 (e.g. Lattimer et al., 1991;

Shen et al., 1998a; Shen et al., 1998b; Shen et al., 2011b; Shen et al., 2011a; Shen et al., 2011c; Hempel et al., 2012; Furusawa et al., 2013).

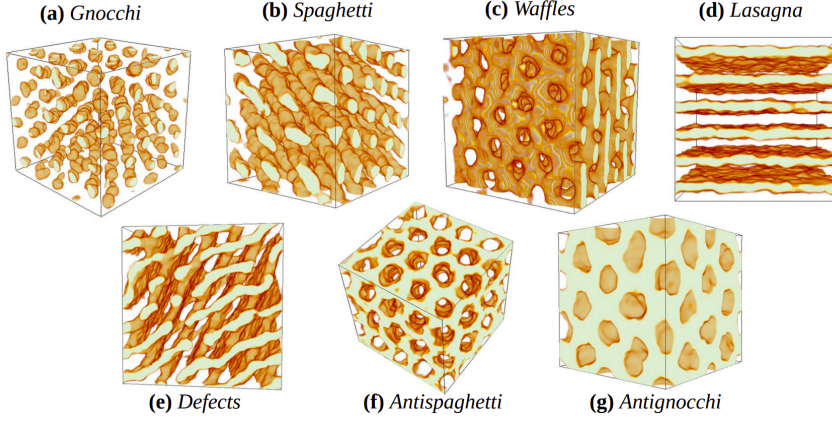


FIGURE D.2: Nuclear pasta configurations produced in molecular dynamic simulations in Caplan et al., 2017 representing the inner composition of a NS. From Caplan et al., 2017

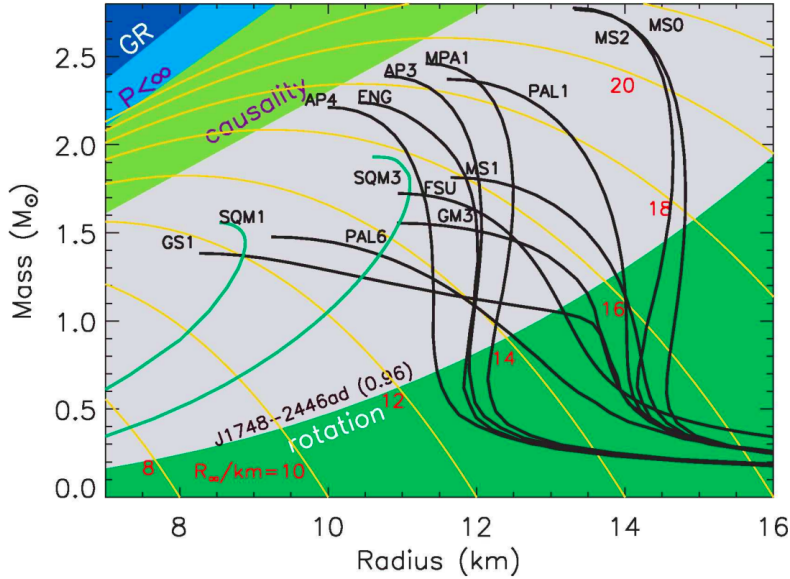


FIGURE D.3: The mass-radius (M-R) plane for NSs including different relations. M-R trajectories for typical EOSs are shown as black curves. Green curves are self-bound quark stars. Orange lines are contours of radiation radius, $R_\infty = R/\sqrt{1 - 2GM/Rc^2}$. The dark blue region is excluded by the GR constraint $R > 2GM/c^2$, the light blue region is excluded by the finite pressure constraint $R > (9/4)GM/c^2$, and the light green region is excluded by causality, $R > 2.9GM/c^2$. The green region in the right-hand corner shows the region $R > R_{max}$ excluded by the 716 Hz pulsar J1748-2446ad. From Paerels et al., 2009

Appendix E

Recovery of Primitive Variables

While the conversion from primitive to conservative variables can be done analytically the opposite conversion is not possible analytically and a numerical solution is needed to obtain the primitive variables from the conserved ones.

In this appendix, we summarize the procedure and the equations to recover the primitive variables from the conservative ones used in **BAM** (see Sec. 4.2.1). The specific algorithm adopted has been developed in a number of previous publications: Font et al., 2000; Pons et al., 1999; Baiotti et al., 2005; Dimmelmeier et al., 2002; Martí et al., 1991.

Specific procedures can be designed once a specific form of EoS is given. The procedure we adopt in the case of cold EoSs is based on an iterative algorithm for ρ . Finally, we describe the modifications introduced to handle the presence of the artificial atmosphere. Following Pons et al., 1999 we start from the definition of conserved variables in Sec. 3.1.2

$$v^i(p) = \frac{S^i}{\tau + D + p}, \quad (\text{E.1})$$

$$W(p) = \frac{\tau + D + p}{\sqrt{(\tau + D + p)^2 - S^2}}, \quad (\text{E.2})$$

$$\epsilon(p) = \frac{1}{D} \sqrt{\sqrt{(\tau + D + p)^2 - S^2} - Wp - D}. \quad (\text{E.3})$$

Since we have expressed everything in terms of the pressure p we can calculate the latter from the EOS as

$$f(p) \equiv p - P(\rho(p), \epsilon(p)) = 0, \quad (\text{E.4})$$

that we solve using a Newton-Raphson method of the type

$$p^{new} = p^{old} - \frac{f(p)}{f'(p)}, \quad (\text{E.5})$$

$$f'(p) = 1 - \chi \frac{\partial \rho}{\partial p} - \kappa \frac{\partial \epsilon}{\partial p}. \quad (\text{E.6})$$

In the case of a one-parameter EOS we have

$$p = p(\rho), \quad (\text{E.7})$$

$$h = h(\rho), \quad (\text{E.8})$$

$$\epsilon = \epsilon(\rho), \quad (\text{E.9})$$

and

$$W = \sqrt{1 + \frac{S^2}{(Dh)^2}}, \quad (\text{E.10})$$

In this case, we solve with a Newton-Raphson the equation

$$g(p) = W(\rho)\rho - D, \quad (\text{E.11})$$

with

$$g'(\rho) = W(\rho) - \rho \frac{S^2 h'(\rho)}{W D^2 h^3}, \quad (\text{E.12})$$

$$h'(\rho) = \epsilon'(\rho) - \frac{p}{\rho^2} + \frac{\chi}{\rho}. \quad (\text{E.13})$$

The recovery procedure for a general EoS can fail at low densities, e.g. in presence of the atmosphere. A reason for this is simply machine accuracy: since typically $p \ll D$, for very low densities the Newton-Raphson algorithm does not converge. A further complication is the spuriously high value of the velocity generated by the artificial atmosphere treatment. To handle these problems both algorithms described above are combined and a set of hierarchic prescriptions are enforced. Specifically

1. when a point reaches a density below the atmosphere threshold density ρ_{th} the code sets atmosphere values both in primitives and conservatives and continues to the next point;
2. if the general EoS algorithm does not converge because the pressure is too low, then atmosphere values are set;

-
3. if it returns unphysical values for ϵ , ρ or p then the code tries the inversion with the algorithm for the cold EoS;
 4. if it returns unphysical values of v^2 then atmosphere values are set;
 5. if the algorithm for the cold EoS does not converge or returns unphysical values not cured in finer grid levels, then the code halts.

Bibliography

- Abbott, B. P. et al. (2017a). “GW170817: Observation of Gravitational Waves from a Binary Neutron Star Inspiral”. In: *Phys. Rev. Lett.* 119.16, p. 161101. DOI: 10.1103/PhysRevLett.119.161101. arXiv: 1710.05832 [gr-qc].
- (2017b). “Multi-messenger Observations of a Binary Neutron Star Merger”. In: *Astrophys. J. Lett.* 848.2, p. L12. DOI: 10.3847/2041-8213/aa91c9. arXiv: 1710.05833 [astro-ph.HE].
- (2016). “Observation of Gravitational Waves from a Binary Black Hole Merger”. In: *Phys. Rev. Lett.* 116.6, p. 061102. DOI: 10.1103/PhysRevLett.116.061102. arXiv: 1602.03837 [gr-qc].
- Alcubierre, M. et al. (May 2001). “Simple excision of a black hole in 3+1 numerical relativity”. In: *Phys. Rev.* 63.10, 104006, p. 104006. DOI: 10.1103/PhysRevD.63.104006. eprint: gr-qc/0008067.
- Alcubierre, M. et al. (2000). “Test-beds and applications for apparent horizon finders in numerical relativity”. In: *Class. Quant. Grav.* 17, pp. 2159–2190. eprint: gr-qc/9809004.
- Alcubierre, Miguel (2008). *Introduction to 3+1 numerical relativity*. International series of monographs on physics. Oxford: Oxford Univ. Press. URL: <https://cds.cern.ch/record/1138167>.
- Alcubierre, Miguel et al. (2003). “Gauge conditions for long-term numerical black hole evolutions without excision”. In: *Phys. Rev. D* 67 (8), p. 084023. DOI: 10.1103/PhysRevD.67.084023. URL: <https://link.aps.org/doi/10.1103/PhysRevD.67.084023>.
- Anile, A. M. (1990). *Relativistic Fluids and Magneto-fluids: With Applications in Astrophysics and Plasma Physics*. Cambridge Monographs on Mathematical Physics. Cambridge University Press. DOI: 10.1017/CB09780511564130.
- Ansorg, Marcus (2005). “A Double-domain spectral method for black hole excision data”. In: *Phys. Rev. D* 72, p. 024018. DOI: 10.1103/PhysRevD.72.024018. arXiv: gr-qc/0505059.

- Ansorg, Marcus et al. (2004). “A Single-domain spectral method for black hole puncture data”. In: *Phys. Rev. D* 70, p. 064011. DOI: 10.1103/PhysRevD.70.064011. arXiv: gr-qc/0404056.
- Anton, Luis et al. (2006). “Numerical 3+1 General Relativistic Magnetohydrodynamics: A Local Characteristic Approach”. In: *The Astrophysical Journal* 637.1, pp. 296–312. DOI: 10.1086/498238. URL: <https://doi.org/10.1086/498238>.
- Arnowitt, R. et al. (1959). “Dynamical Structure and Definition of Energy in General Relativity”. In: *Phys. Rev.* 116 (5), pp. 1322–1330. DOI: 10.1103/PhysRev.116.1322. URL: <https://link.aps.org/doi/10.1103/PhysRev.116.1322>.
- Arnowitt, Richard et al. (2008). “Republication of: The dynamics of general relativity”. In: *General Relativity and Gravitation* 40.9, pp. 1997–2027.
- Assumpcao, Thiago et al. (Nov. 2021). “NRPyElliptic: A Fast Hyperbolic Relaxation Elliptic Solver for Numerical Relativity, I: Conformally Flat, Binary Puncture Initial Data”. In: arXiv: 2111.02424 [gr-qc].
- Babak, Stanislav et al. (2017). “Validating the effective-one-body model of spinning, precessing binary black holes against numerical relativity”. In: *Phys. Rev. D* 95.2, p. 024010. DOI: 10.1103/PhysRevD.95.024010. arXiv: 1607.05661 [gr-qc].
- Baiotti, Luca et al. (2006). “Challenging the Paradigm of Singularity Excision in Gravitational Collapse”. In: *Phys. Rev. Lett.* 97 (14), p. 141101. DOI: 10.1103/PhysRevLett.97.141101. URL: <https://link.aps.org/doi/10.1103/PhysRevLett.97.141101>.
- Baiotti, Luca et al. (2005). “Three-dimensional relativistic simulations of rotating neutron-star collapse to a Kerr black hole”. In: *Phys. Rev. D* 71 (2), p. 024035. DOI: 10.1103/PhysRevD.71.024035. URL: <https://link.aps.org/doi/10.1103/PhysRevD.71.024035>.
- Baker, John G. et al. (2006). “Gravitational-Wave Extraction from an Inspiring Configuration of Merging Black Holes”. In: *Phys. Rev. Lett.* 96 (11), p. 111102. DOI: 10.1103/PhysRevLett.96.111102. URL: <https://link.aps.org/doi/10.1103/PhysRevLett.96.111102>.
- Balsara, Dinshaw (Dec. 2008). “Total Variation Diminishing Scheme for Relativistic Magnetohydrodynamics”. In: *The Astrophysical Journal Supplement Series* 132, p. 83. DOI: 10.1086/318941.

- Balsara, Dinshaw S. et al. (Mar. 1999). “A Staggered Mesh Algorithm Using High Order Godunov Fluxes to Ensure Solenoidal Magnetic Fields in Magnetohydrodynamic Simulations”. In: *Journal of Computational Physics* 149.2, pp. 270–292. DOI: 10.1006/jcph.1998.6153.
- Banyuls, Francesc et al. (Feb. 1997). “Numerical $\{3 + 1\}$ General Relativistic Hydrodynamics: A Local Characteristic Approach”. In: *The Astrophysical Journal* 476.1, pp. 221–231. DOI: 10.1086/303604.
- Bardeen, James M. et al. (Dec. 1972). “Rotating Black Holes: Locally Nonrotating Frames, Energy Extraction, and Scalar Synchrotron Radiation”. In: *The Astrophysical Journal* 178, pp. 347–370. DOI: 10.1086/151796.
- Baron, E. et al. (July 1985). “Supernovae and the nuclear equation of state at high densities”. In: *Nuclear Physics A* 440.4, pp. 744–754. DOI: 10.1016/0375-9474(85)90405-1.
- Battat, James B. R. et al. (2007). “Testing for Lorentz Violation: Constraints on Standard-Model-Extension Parameters via Lunar Laser Ranging”. In: *Phys. Rev. Lett.* 99 (24), p. 241103. DOI: 10.1103/PhysRevLett.99.241103. URL: <https://link.aps.org/doi/10.1103/PhysRevLett.99.241103>.
- Baumgarte, Thomas W. et al. (1998a). “Numerical integration of Einstein’s field equations”. In: *Phys. Rev. D* 59 (2), p. 024007. DOI: 10.1103/PhysRevD.59.024007. URL: <https://link.aps.org/doi/10.1103/PhysRevD.59.024007>.
- (Dec. 1998b). “Numerical integration of Einstein’s field equations”. In: *Phys. Rev. D* 59.2. arXiv:gr-qc/9810065, p. 024007. DOI: 10.1103/PhysRevD.59.024007.
- Berger, Marsha J. et al. (1984). “Adaptive Mesh Refinement for Hyperbolic Partial Differential Equations”. In: *J. Comput. Phys.* 53, p. 484. DOI: 10.1016/0021-9991(84)90073-1.
- Bernuzzi, Sebastiano et al. (2010). “Constraint violation in free evolution schemes: Comparing BSSNOK with a conformal decomposition of Z_4 ”. In: *Phys. Rev. D* 81, p. 084003. DOI: 10.1103/PhysRevD.81.084003. arXiv: 0912.2920 [gr-qc].
- Blanchet, Luc (2014). “Gravitational Radiation from Post-Newtonian Sources and Inspiralling Compact Binaries”. In: *Living Rev. Rel.* 17, p. 2. DOI: 10.12942/lrr-2014-2. arXiv: 1310.1528 [gr-qc].
- Bona, C. et al. (2003). “General-covariant evolution formalism for numerical relativity”. In: *Phys. Rev. D* 67 (10), p. 104005. DOI: 10.1103/PhysRevD.67.104005. URL: <https://link.aps.org/doi/10.1103/PhysRevD.67.104005>.

- Bona, C. et al. (July 1995). “New Formalism for Numerical Relativity”. In: *Physical Review Letters* 75, pp. 600–603. DOI: 10.1103/PhysRevLett.75.600. eprint: gr-qc/9412071.
- Bona, C. et al. (2004). “Symmetry-breaking mechanism for the Z4 general-covariant evolution system”. In: *Phys. Rev. D* 69 (6), p. 064036. DOI: 10.1103/PhysRevD.69.064036. URL: <https://link.aps.org/doi/10.1103/PhysRevD.69.064036>.
- Borges, Rafael et al. (2008). “An improved weighted essentially non-oscillatory scheme for hyperbolic conservation laws”. In: *Journal of Computational Physics* 227.6, pp. 3191–3211. ISSN: 0021-9991. DOI: <https://doi.org/10.1016/j.jcp.2007.11.038>. URL: <https://www.sciencedirect.com/science/article/pii/S0021999107005232>.
- Brandt, Steven R. et al. (Dec. 2021). *The Einstein Toolkit*. Version The "Katherine Johnson" release, ET_2021_11. To find out more, visit <http://einstein toolkit.org>. DOI: 10.5281/zenodo.5770803. URL: <https://doi.org/10.5281/zenodo.5770803>.
- Brill, Dieter R. et al. (1963). “Interaction Energy in Geometrostatics”. In: *Phys. Rev.* 131 (1), pp. 471–476. DOI: 10.1103/PhysRev.131.471. URL: <https://link.aps.org/doi/10.1103/PhysRev.131.471>.
- Broekgaarden, Floor S. et al. (2021). “Formation of the First Two Black Hole–Neutron Star Mergers (GW200115 and GW200105) from Isolated Binary Evolution”. In: *The Astrophysical Journal Letters* 920.1, p. L13. DOI: 10.3847/2041-8213/ac2832. URL: <https://doi.org/10.3847/2041-8213/ac2832>.
- Broekgaarden, Floor S. et al. (Dec. 2021). “Impact of massive binary star and cosmic evolution on gravitational wave observations I: black hole-neutron star mergers”. In: *Monthly Notices of the Royal Astronomical Society* 508.4, pp. 5028–5063. DOI: 10.1093/mnras/stab2716. arXiv: 2103.02608 [astro-ph.HE].
- Bruenn, S. W. (Aug. 1985). “Stellar core collapse - Numerical model and infall epoch”. In: *The Astrophysical Journal* 58, pp. 771–841. DOI: 10.1086/191056.
- Brügmann, Bernd (1996). “Bifunctional adaptive mesh (BAM) for 3d numerical relativity”. In: ed. by Singapore: World Scientific, pp. 613–615.
- (1999). “Binary Black Hole mergers in 3d numerical relativity”. In: *International Journal of Modern Physics D* 08.01, pp. 85–100. DOI: 10.1142/S0218271899000080. eprint: <https://doi.org/10.1142/S0218271899000080>. URL: <https://doi.org/10.1142/S0218271899000080>.

- Brügmann, Bernd et al. (2008). “Calibration of moving puncture simulations”. In: *Phys. Rev. D* 77 (2), p. 024027. DOI: 10.1103/PhysRevD.77.024027. URL: <https://link.aps.org/doi/10.1103/PhysRevD.77.024027>.
- Brügmann, Bernd et al. (2004). “Numerical Simulation of Orbiting Black Holes”. In: *Phys. Rev. Lett.* 92 (21), p. 211101. DOI: 10.1103/PhysRevLett.92.211101. URL: <https://link.aps.org/doi/10.1103/PhysRevLett.92.211101>.
- Burden, Richard (2011). *Numerical analysis*. Boston, MA: Brooks/Cole, Cengage Learning. ISBN: 9780538733519.
- Burrows, Adam et al. (2006). “Neutrino opacities in nuclear matter”. In: *Nucl. Phys. A* 777, pp. 356–394. DOI: 10.1016/j.nuclphysa.2004.06.012. arXiv: astro-ph/0404432.
- Campanelli, M. et al. (2006). “Accurate Evolutions of Orbiting Black-Hole Binaries without Excision”. In: *Phys. Rev. Lett.* 96 (11), p. 111101. DOI: 10.1103/PhysRevLett.96.111101. URL: <https://link.aps.org/doi/10.1103/PhysRevLett.96.111101>.
- Cao, Zhoujian et al. (2012). “Numerical stability of the Z4c formulation of general relativity”. In: *Phys. Rev. D* 85, p. 124032. DOI: 10.1103/PhysRevD.85.124032. arXiv: 1111.2177 [gr-qc].
- Caplan, M. E. et al. (2017). “Colloquium : Astromaterial science and nuclear pasta”. In: *Rev. Mod. Phys.* 89.4, p. 041002. DOI: 10.1103/RevModPhys.89.041002. arXiv: 1606.03646 [astro-ph.HE].
- Cardall, Christian Y. et al. (2013). “Conservative 3+1 General Relativistic Boltzmann Equation”. In: *Phys. Rev. D* 88, p. 023011. DOI: 10.1103/PhysRevD.88.023011. arXiv: 1305.0037 [astro-ph.HE].
- Cardall, Christian Y. et al. (2003). “Conservative formulations of general relativistic kinetic theory”. In: *Phys. Rev. D* 68, p. 023006. DOI: 10.1103/PhysRevD.68.023006. arXiv: astro-ph/0212460.
- Chattopadhyay, Debatri et al. (Apr. 2021). “Modelling neutron star–black hole binaries: future pulsar surveys and gravitational wave detectors”. In: *Monthly Notices of the Royal Astronomical Society* 504.3, pp. 3682–3710. ISSN: 0035-8711. DOI: 10.1093/mnras/stab973. eprint: <https://academic.oup.com/mnras/article-pdf/504/3/3682/37888780/stab973.pdf>. URL: <https://doi.org/10.1093/mnras/stab973>.
- Chaurasia, Swami Vivekanandji et al. (2021). “Black hole-neutron star simulations with the BAM code: First tests and simulations”. In: *Phys. Rev. D* 104 (8), p. 084010.

- DOI: 10.1103/PhysRevD.104.084010. URL: <https://link.aps.org/doi/10.1103/PhysRevD.104.084010>.
- Chaurasia, Swami Vivekanandji et al. (2020). “Gravitational waves and mass ejecta from binary neutron star mergers: Effect of the spin orientation”. In: *Phys. Rev. D* 102.2, p. 024087. DOI: 10.1103/PhysRevD.102.024087. arXiv: 2003.11901 [gr-qc].
- Cipolletta, F. et al. (July 2020). “Spritz: a new fully general-relativistic magnetohydrodynamic code”. In: *Classical and Quantum Gravity* 37.13, 135010, p. 135010. DOI: 10.1088/1361-6382/ab8be8. arXiv: 1912.04794 [astro-ph.HE].
- Cipolletta, Federico et al. (2021). “Spritz: General Relativistic Magnetohydrodynamics with Neutrinos”. In: *Class. Quant. Grav.* 38.8, p. 085021. DOI: 10.1088/1361-6382/abebb7. arXiv: 2012.10174 [astro-ph.HE].
- Clausen, Drew et al. (June 2014). “Dynamically formed black hole+millisecond pulsar binaries in globular clusters”. In: *Monthly Notices of the Royal Astronomical Society* 442.1, pp. 207–219. ISSN: 0035-8711. DOI: 10.1093/mnras/stu871. eprint: <https://academic.oup.com/mnras/article-pdf/442/1/207/4073763/stu871.pdf>. URL: <https://doi.org/10.1093/mnras/stu871>.
- Collaboration, LIGO Scientific et al. (2021). “Observation of Gravitational Waves from Two Neutron Star–Black Hole Coalescences”. In: *The Astrophysical Journal Letters* 915.1, p. L5. DOI: 10.3847/2041-8213/ac082e. URL: <https://doi.org/10.3847/2041-8213/ac082e>.
- Cook, Gregory B. (Nov. 2000). “Initial Data for Numerical Relativity”. In: *Living Reviews in Relativity* 3.1, 5, p. 5. DOI: 10.12942/lrr-2000-5. arXiv: gr-qc/0007085 [gr-qc].
- Cook, Gregory B. et al. (2004). “Excision boundary conditions for black hole initial data”. In: *Phys. Rev. D* 70, p. 104016. DOI: 10.1103/PhysRevD.70.104016. arXiv: gr-qc/0407078.
- Cooperstein, J. (1988). “Neutrinos in supernovae”. In: *Physics Reports* 163.1, pp. 95–126. ISSN: 0370-1573. DOI: [https://doi.org/10.1016/0370-1573\(88\)90038-5](https://doi.org/10.1016/0370-1573(88)90038-5). URL: <https://www.sciencedirect.com/science/article/pii/0370157388900385>.
- Dain, Sergio (2002). “Asymptotically flat and regular Cauchy data”. In: *Lect. Notes Phys.* 604. Ed. by J. Frauendiener et al., pp. 161–182. arXiv: gr-qc/0203021.
- Davis, Timothy A. (2004). “Algorithm 832: UMFPACK V4.3 - An unsymmetric-pattern multifrontal method”. In: *ACM Transactions on Mathematical Software*

- 30.2, pp. 196–199. ISSN: 00983500. DOI: 10.1145/992200.992206. URL: <https://doi.org/10.1145/992200.992206>.
- Dedner, A. et al. (2002). “Hyperbolic Divergence Cleaning for the MHD Equations”. In: *Journal of Computational Physics* 175.2, pp. 645–673. ISSN: 0021-9991. DOI: <https://doi.org/10.1006/jcph.2001.6961>. URL: <https://www.sciencedirect.com/science/article/pii/S002199910196961X>.
- Dietrich, Tim et al. (2015). “Numerical relativity simulations of neutron star merger remnants using conservative mesh refinement”. In: *Phys. Rev. D* 91 (12), p. 124041. DOI: 10.1103/PhysRevD.91.124041. URL: <https://link.aps.org/doi/10.1103/PhysRevD.91.124041>.
- Dimmelmeier, Harald et al. (2002). “Relativistic simulations of rotational core collapse. 1. Methods, initial models, and code tests”. In: *Astron. Astrophys.* 388, pp. 917–935. DOI: 10.1051/0004-6361:20020563. arXiv: astro-ph/0204288.
- Duez, Matthew D. et al. (2005). “Relativistic magnetohydrodynamics in dynamical spacetimes: Numerical methods and tests”. In: *Phys. Rev. D* 72 (2), p. 024028. DOI: 10.1103/PhysRevD.72.024028. URL: <https://link.aps.org/doi/10.1103/PhysRevD.72.024028>.
- Eichler, H. J. et al. (1997). “Optical Vector Wave Mixing Processes in Nonlinear Birefringent Nematic Liquid Crystals”. In: *Phys. Rev. Lett.* 78 (25), pp. 4753–4756. DOI: 10.1103/PhysRevLett.78.4753. URL: <https://link.aps.org/doi/10.1103/PhysRevLett.78.4753>.
- Endrizzi, Andrea et al. (2020). “Thermodynamics conditions of matter in the neutrino decoupling region during neutron star mergers”. In: *Eur. Phys. J. A* 56.1, p. 15. DOI: 10.1140/epja/s10050-019-00018-6. arXiv: 1908.04952 [astro-ph.HE].
- Epstein, R. I. et al. (Feb. 1981). “Lepton loss and entropy generation in stellar collapse”. In: *The Astrophysical Journal* 243, pp. 1003–1012. DOI: 10.1086/158665.
- Etienne, Zachariah B. et al. (2010). “Relativistic magnetohydrodynamics in dynamical spacetimes: A new adaptive mesh refinement implementation”. In: *Phys. Rev. D* 82 (8), p. 084031. DOI: 10.1103/PhysRevD.82.084031. URL: <https://link.aps.org/doi/10.1103/PhysRevD.82.084031>.
- Etienne, Zachariah B. et al. (Jan. 2012). “Relativistic magnetohydrodynamics in dynamical spacetimes: Improved electromagnetic gauge condition for adaptive mesh refinement grids”. English (US). In: *Physical Review D* 85.2. ISSN: 0556-2821. DOI: 10.1103/PhysRevD.85.024013.

- Evans, Charles R. et al. (1988). “Simulation of Magnetohydrodynamic Flows: A Constrained Transport Model”. In: *The Astrophysical Journal* 332, p. 659. DOI: 10.1086/166684.
- Fischer, Nils L. et al. (Aug. 2021a). “A discontinuous Galerkin scheme for a large class of elliptic equations”. In: arXiv: 2108.05826 [math.NA].
- Fischer, Nils L. et al. (Nov. 2021b). “A scalable elliptic solver with task-based parallelism for the SpECTRE numerical relativity code”. In: arXiv: 2111.06767 [gr-qc].
- Font, J. A. et al. (2002). “Three-dimensional numerical general relativistic hydrodynamics. II. Long-term dynamics of single relativistic stars”. In: *Physical Review. D, Particles Fields* 65 (8). DOI: 10.1103/PhysRevD.65.084024.
- Font, Jose A. et al. (2000). “Three-dimensional numerical general relativistic hydrodynamics. 1. Formulations, methods, and code tests”. In: *Phys. Rev. D* 61, p. 044011. DOI: 10.1103/PhysRevD.61.044011. arXiv: gr-qc/9811015.
- Foucart, Francois (2020). “A brief overview of black hole-neutron star mergers”. In: *Front. Astron. Space Sci.* 7, p. 46. DOI: 10.3389/fspas.2020.00046. arXiv: 2006.10570 [astro-ph.HE].
- (2012). “Black-hole–neutron-star mergers: Disk mass predictions”. In: *Phys. Rev. D* 86 (12), p. 124007. DOI: 10.1103/PhysRevD.86.124007. URL: <https://link.aps.org/doi/10.1103/PhysRevD.86.124007>.
- Foucart, Francois et al. (2018a). “Evaluating radiation transport errors in merger simulations using a Monte Carlo algorithm”. In: *Phys. Rev. D* 98.6, p. 063007. DOI: 10.1103/PhysRevD.98.063007. arXiv: 1806.02349 [astro-ph.HE].
- Foucart, Francois et al. (2016). “Impact of an improved neutrino energy estimate on outflows in neutron star merger simulations”. In: *Phys. Rev. D* 94.12, p. 123016. DOI: 10.1103/PhysRevD.94.123016. arXiv: 1607.07450 [astro-ph.HE].
- Foucart, Francois et al. (2008). “Initial data for black hole-neutron star binaries: A Flexible, high-accuracy spectral method”. In: *Phys. Rev. D* 77, p. 124051. DOI: 10.1103/PhysRevD.77.124051. arXiv: 0804.3787 [gr-qc].
- Foucart, Francois et al. (2015). “Post-merger evolution of a neutron star-black hole binary with neutrino transport”. In: *Phys. Rev. D* 91.12, p. 124021. DOI: 10.1103/PhysRevD.91.124021. arXiv: 1502.04146 [astro-ph.HE].
- Foucart, Francois et al. (2018b). “Remnant baryon mass in neutron star-black hole mergers: Predictions for binary neutron star mimickers and rapidly spinning black

- holes”. In: *Phys. Rev. D* 98.8, p. 081501. DOI: 10.1103/PhysRevD.98.081501. arXiv: 1807.00011 [astro-ph.HE].
- Furusawa, Shun et al. (Aug. 2013). “New Equations of State Based on the Liquid Drop Model of Heavy Nuclei and Quantum Approach to Light Nuclei for Core-collapse Supernova Simulations”. In: *The Astrophysical Journal* 772.2, 95, p. 95. DOI: 10.1088/0004-637X/772/2/95. arXiv: 1305.1508 [astro-ph.HE].
- Gammie, Charles F. et al. (May 2003). “HARM: A numerical scheme for general relativistic magnetohydrodynamics”. English (US). In: *Astrophysical Journal* 589.1 I, pp. 444–457. ISSN: 0004-637X. DOI: 10.1086/374594.
- Giacomazzo, Bruno et al. (2006). “The Exact solution of the Riemann problem in relativistic MHD”. In: *J. Fluid Mech.* 562, p. 223. DOI: 10.1017/S0022112006001145. arXiv: gr-qc/0507102.
- (2007). “WhiskyMHD: a new numerical code for general relativistic magnetohydrodynamics”. In: *Class. Quantum Grav.* 24. (), S235–S258. URL: <http://iopscience.iop.org/0264-9381/24/12/S16/>.
- Gourgoulhon, E. (2012). *3+1 Formalism in General Relativity: Bases of Numerical Relativity*. Vol. 846. Lecture Notes in Physics. Berlin; New York: Springer. DOI: 10.1007/978-3-642-24525-1. arXiv: gr-qc/0703035 [gr-qc].
- Gourgoulhon, Eric (2011). *3 + 1 Formalism in General Relativity*. July. Berlin New York: Springer. ISBN: 978-3-642-24525-1.
- Grandclement, Philippe (2006). “Accurate and realistic initial data for black hole-neutron star binaries”. In: *Phys. Rev. D* 74. [Erratum: Phys.Rev.D 75, 129903 (2007)], p. 124002. DOI: 10.1103/PhysRevD.74.124002. arXiv: gr-qc/0609044.
- Gundlach, Carsten (1998). “Pseudo-spectral apparent horizon finders: An efficient new algorithm”. In: *Phys. Rev. D* 57, pp. 863–875. eprint: gr-qc/9707050.
- Gundlach, Carsten et al. (2006). “Well-posedness of formulations of the Einstein equations with dynamical lapse and shift conditions”. In: *Physical Review D* 74, p. 024016.
- Hadamard, J. (1902). “Sur les Problèmes aux Dérivées Partielles et Leur Signification Physique”. In: *Princeton University Bulletin* 13, pp. 49–52.
- Hahn, S. G. et al. (Sept. 1964). “The two-body problem in geometrodynamics”. In: *Annals of Physics* 29, pp. 304–331. DOI: 10.1016/0003-4916(64)90223-4.
- Hannestad, Steen et al. (1998). “Supernova neutrino opacity from nucleon-nucleon Bremsstrahlung and related processes”. In: *Astrophys. J.* 507, pp. 339–352. DOI: 10.1086/306303. arXiv: astro-ph/9711132.

- Harten, Ami (1997). “High Resolution Schemes for Hyperbolic Conservation Laws”. In: *Journal of Computational Physics* 135.2, pp. 260–278. ISSN: 0021-9991. DOI: <https://doi.org/10.1006/jcph.1997.5713>. URL: <https://www.sciencedirect.com/science/article/pii/S0021999197957132>.
- Hempel, M. et al. (2012). “NEW EQUATIONS OF STATE IN SIMULATIONS OF CORE-COLLAPSE SUPERNOVAE”. In: *The Astrophysical Journal* 748.1, p. 70. DOI: 10.1088/0004-637x/748/1/70. URL: <https://doi.org/10.1088/0004-637x/748/1/70>.
- Hempel, Matthias et al. (2010). “Statistical Model for a Complete Supernova Equation of State”. In: *Nucl. Phys. A* 837, pp. 210–254. DOI: 10.1016/j.nuclphysa.2010.02.010. arXiv: 0911.4073 [nucl-th].
- Hilditch, David et al. (2013). “Compact binary evolutions with the Z4c formulation”. In: *Phys. Rev. D* 88, p. 084057. DOI: 10.1103/PhysRevD.88.084057. arXiv: 1212.2901 [gr-qc].
- Horowitz, C. J. (2002). “Weak magnetism for anti-neutrinos in supernovae”. In: *Phys. Rev. D* 65, p. 043001. DOI: 10.1103/PhysRevD.65.043001. arXiv: astro-ph/0109209.
- Hou, Thomas Y. et al. (1994). “Why nonconservative schemes converge to wrong solutions: error analysis”. In: *Mathematics of Computation* 62.206, pp. 497–530.
- Khamesra, Bhavesh et al. (2021). “Black hole–neutron star binary mergers: the imprint of tidal deformations and debris”. In: *Class. Quant. Grav.* 38.18, p. 185008. DOI: 10.1088/1361-6382/ac1a66. arXiv: 2101.10252 [astro-ph.HE].
- Kidder, Lawrence E. et al. (2000). “Black hole evolution by spectral methods”. In: *Phys. Rev. D* 62 (8), p. 084032. DOI: 10.1103/PhysRevD.62.084032. URL: <https://link.aps.org/doi/10.1103/PhysRevD.62.084032>.
- Kiuchi, Kenta et al. (2015). “Efficient magnetic-field amplification due to the Kelvin-Helmholtz instability in binary neutron star mergers”. In: *Phys. Rev. D* 92.12, p. 124034. DOI: 10.1103/PhysRevD.92.124034. arXiv: 1509.09205 [astro-ph.HE].
- Koide, S. et al. (1999). “Relativistic Jet Formation from Black Hole Magnetized Accretion Disks: Method, Tests, and Applications of a General Relativistic Magneto-hydrodynamic Numerical Code”. In: *The Astrophysical Journal* 522, pp. 727–752.
- Komissarov, S. S. (Feb. 1999). “A Godunov-type scheme for relativistic magnetohydrodynamics”. In: *Monthly Notices of the Royal Astronomical Society* 303.2, pp. 343–366. ISSN: 0035-8711. DOI: 10.1046/j.1365-8711.1999.02244.x. eprint: <https://arxiv.org/abs/199902244>.

- [//academic.oup.com/mnras/article-pdf/303/2/343/18631502/303-2-343.pdf](https://academic.oup.com/mnras/article-pdf/303/2/343/18631502/303-2-343.pdf). URL: <https://doi.org/10.1046/j.1365-8711.1999.02244.x>.
- Kulkarni, S. R. (Oct. 2005). “Modeling supernova-like explosions associated with gamma-ray bursts with short durations”. In: arXiv: astro-ph/0510256.
- Kutta, W. (1901). “Beitrag zur Naherungsweise Integration Totaler Differentialgleichungen”. In.
- Kyutoku, Koutarou et al. (2021). “Coalescence of black hole–neutron star binaries”. In: *Living Rev. Rel.* 24.1, p. 5. DOI: 10.1007/s41114-021-00033-4. arXiv: 2110.06218 [astro-ph.HE].
- Kyutoku, Koutarou et al. (2015). “Dynamical mass ejection from black hole–neutron star binaries”. In: *Phys. Rev. D* 92 (4), p. 044028. DOI: 10.1103/PhysRevD.92.044028. URL: <https://link.aps.org/doi/10.1103/PhysRevD.92.044028>.
- Kyutoku, Koutarou et al. (2011). “Gravitational waves from spinning black hole–neutron star binaries: dependence on black hole spins and on neutron star equations of state”. In: *Phys. Rev. D* 84 (6), p. 064018. DOI: 10.1103/PhysRevD.84.064018. URL: <https://link.aps.org/doi/10.1103/PhysRevD.84.064018>.
- Lattimer, James M. et al. (1991). “A generalized equation of state for hot, dense matter”. In: *Nuclear Physics A* 535.2, pp. 331–376. ISSN: 0375-9474. DOI: [https://doi.org/10.1016/0375-9474\(91\)90452-C](https://doi.org/10.1016/0375-9474(91)90452-C). URL: <https://www.sciencedirect.com/science/article/pii/037594749190452C>.
- Lax, Peter et al. (1960). “Systems of conservation laws”. In: *Communications on Pure and Applied Mathematics* 13.2, pp. 217–237. DOI: <https://doi.org/10.1002/cpa.3160130205>. eprint: <https://onlinelibrary.wiley.com/doi/pdf/10.1002/cpa.3160130205>. URL: <https://onlinelibrary.wiley.com/doi/abs/10.1002/cpa.3160130205>.
- Le Tiec, Alexandre et al. (July 2016). “Theory of Gravitational Waves”. In.
- Levermore, C.D. (1984). “Relating Eddington factors to flux limiters”. In: *Journal of Quantitative Spectroscopy and Radiative Transfer* 31.2, pp. 149–160. ISSN: 0022-4073. DOI: [https://doi.org/10.1016/0022-4073\(84\)90112-2](https://doi.org/10.1016/0022-4073(84)90112-2). URL: <https://www.sciencedirect.com/science/article/pii/0022407384901122>.
- Li, Li-Xin et al. (1998). “Transient events from neutron star mergers”. In: *Astrophys. J. Lett.* 507, p. L59. DOI: 10.1086/311680. arXiv: astro-ph/9807272.
- Lichnerowicz, A. (1944). “L’integration des equations de la gravitation relativiste et la probleme des n corps”. In: *J. Math. Pures et Appl.* 23, p. 87.

- Liebendorfer, Matthias et al. (2004). “A Finite Difference Representation of Neutrino Radiation Hydrodynamics in Spherically Symmetric General Relativistic Space-time”. In: *The Astrophysical Journal Supplement Series* 150.1, pp. 263–316. DOI: 10.1086/380191. URL: <https://doi.org/10.1086/380191>.
- Liebendörfer, Matthias et al. (May 2001). “Conservative general relativistic radiation hydrodynamics in spherical symmetry and comoving coordinates”. In: *Physical Review D* 63.10, 104003, p. 104003. DOI: 10.1103/PhysRevD.63.104003. arXiv: astro-ph/0012201 [astro-ph].
- Liebendörfer, Matthias et al. (2001). “Probing the gravitational well: No supernova explosion in spherical symmetry with general relativistic Boltzmann neutrino transport”. In: *Phys. Rev. D* 63 (10), p. 103004. DOI: 10.1103/PhysRevD.63.103004. URL: <https://link.aps.org/doi/10.1103/PhysRevD.63.103004>.
- Liebling, Steven L. et al. (2010). “Evolutions of magnetized and rotating neutron stars”. In: *Phys. Rev. D* 81 (12), p. 124023. DOI: 10.1103/PhysRevD.81.124023. URL: <https://link.aps.org/doi/10.1103/PhysRevD.81.124023>.
- Liu, Xu-Dong et al. (1998). “Convex ENO High Order Multi-dimensional Schemes without Field by Field Decomposition or Staggered Grids”. In: *Journal of Computational Physics* 142.2, pp. 304–330. ISSN: 0021-9991. DOI: <https://doi.org/10.1006/jcph.1998.5937>. URL: <https://www.sciencedirect.com/science/article/pii/S002199919895937X>.
- Lo, Ka-Wai et al. (2011). “The spin parameter of uniformly rotating compact stars”. In: *Astrophys. J.* 728, p. 12. DOI: 10.1088/0004-637X/728/1/12. arXiv: 1011.3563 [astro-ph.HE].
- Lorene (n.d.). *Langage Objet pour la RElativité Numérique*. URL: <http://www.lorene.obspm.fr>.
- Martí, José Ma. et al. (1991). “Numerical relativistic hydrodynamics: Local characteristic approach”. In: *Phys. Rev. D* 43 (12), pp. 3794–3801. DOI: 10.1103/PhysRevD.43.3794. URL: <https://link.aps.org/doi/10.1103/PhysRevD.43.3794>.
- McKinney, Jonathan C. et al. (2004). “A Measurement of the Electromagnetic Luminosity of a Kerr Black Hole”. In: *The Astrophysical Journal* 611.2, pp. 977–995. DOI: 10.1086/422244. arXiv: astro-ph/0404512 [astro-ph].
- Metzger, Brian D. (2017). “Kilonovae”. In: *Living Rev. Rel.* 20.1, p. 3. DOI: 10.1007/s41114-017-0006-z. arXiv: 1610.09381 [astro-ph.HE].

- Mezzacappa, Anthony et al. (Mar. 1993). “A Numerical Method for Solving the Neutrino Boltzmann Equation Coupled to Spherically Symmetric Stellar Core Collapse”. In: *The Astrophysical Journal* 405, p. 669. DOI: 10.1086/172395.
- Mezzacappa, Anthony et al. (Aug. 1989). “Computer Simulation of Time-dependent, Spherically Symmetric Spacetimes Containing Radiating Fluids: Formalism and Code Tests”. In: *The Astrophysical Journal* 343, p. 853. DOI: 10.1086/167756.
- Nakamura, Takashi et al. (1987). “General Relativistic Collapse to Black Holes and Gravitational Waves from Black Holes”. In: *Progress of Theoretical Physics Supplement* 90, p. 1. DOI: 10.1143/PTPS.90.1. eprint: /oup/backfile/content_public/journal/ptps/90/10.1143/ptps.90.1/2/90-1.pdf. URL: +http://dx.doi.org/10.1143/PTPS.90.1.
- Neilsen, David et al. (2014). “Magnetized neutron stars with realistic equations of state and neutrino cooling”. In: *Phys. Rev. D* 89 (10), p. 104029. DOI: 10.1103/PhysRevD.89.104029. URL: <https://link.aps.org/doi/10.1103/PhysRevD.89.104029>.
- Nobel Prize in Physics 2017* (n.d.). <https://www.nobelprize.org/prizes/physics/2017/summary/>.
- Noble, Scott C. et al. (Apr. 2006). “Primitive Variable Solvers for Conservative General Relativistic Magnetohydrodynamics”. In: *The Astrophysical Journal* 641.1, pp. 626–637. DOI: 10.1086/500349. arXiv: astro-ph/0512420 [astro-ph].
- Paerels, F. et al. (2009). “The Behavior Of Matter Under Extreme Conditions”. In: 2010, p. 230. arXiv: 0904.0435 [astro-ph.HE].
- Palenzuela, Carlos et al. (2015). “Effects of the microphysical equation of state in the mergers of magnetized neutron stars with neutrino cooling”. In: *Phys. Rev. D* 92 (4), p. 044045. DOI: 10.1103/PhysRevD.92.044045. URL: <https://link.aps.org/doi/10.1103/PhysRevD.92.044045>.
- Pannarale, Francesco et al. (2015). “Gravitational-wave cutoff frequencies of tidally disruptive neutron star-black hole binary mergers”. In: *Phys. Rev. D* 92 (8), p. 081504. DOI: 10.1103/PhysRevD.92.081504. URL: <https://link.aps.org/doi/10.1103/PhysRevD.92.081504>.
- Papenfort, L. Jens et al. (2021). “New public code for initial data of unequal-mass, spinning compact-object binaries”. In: *Phys. Rev. D* 104.2, p. 024057. DOI: 10.1103/PhysRevD.104.024057. arXiv: 2103.09911 [gr-qc].

- Paschalidis, Vasileios et al. (2015). “Relativistic Simulations of Black Hole - Neutron Star Coalescence: the jet Emerges”. In: *Astrophys. J.* 806.1, p. L14. DOI: 10.1088/2041-8205/806/1/L14. arXiv: 1410.7392 [astro-ph.HE].
- Penner, Andrew J (2011). “General Relativistic Magnetohydrodynamic Bondi–Hoyle Accretion”. In: *Mon. Not. Roy. Astron. Soc.* 414, p. 1467. DOI: 10.1111/j.1365-2966.2011.18480.x. arXiv: 1011.2976 [astro-ph.HE].
- Perego, A. et al. (2014a). “Neutrino-driven winds from neutron star merger remnants”. In: *Mon. Not. Roy. Astron. Soc.* 443.4, pp. 3134–3156. DOI: 10.1093/mnras/stu1352. arXiv: 1405.6730 [astro-ph.HE].
- Perego, Albino et al. (2016). “An advanced leakage scheme for neutrino treatment in astrophysical simulations”. In: *Astrophys. J. Suppl.* 223.2, p. 22. DOI: 10.3847/0067-0049/223/2/22. arXiv: 1511.08519 [astro-ph.IM].
- Perego, Albino et al. (2014b). “MODA: a new algorithm to compute optical depths in multidimensional hydrodynamic simulations”. In: *Astron. Astrophys.* 568, A11. DOI: 10.1051/0004-6361/201423755. arXiv: 1403.1297 [astro-ph.HE].
- Perego, Albino et al. (2019). “Thermodynamics conditions of matter in neutron star mergers”. In: *Eur. Phys. J. A* 55.8, p. 124. DOI: 10.1140/epja/i2019-12810-7. arXiv: 1903.07898 [gr-qc].
- Pfeiffer, Harald P. et al. (2003a). “A Multidomain spectral method for solving elliptic equations”. In: *Comput. Phys. Commun.* 152, pp. 253–273. DOI: 10.1016/S0010-4655(02)00847-0. arXiv: gr-qc/0202096.
- Pfeiffer, Harald P. et al. (2003b). “Extrinsic curvature and the Einstein constraints”. In: *Phys. Rev. D* 67, p. 044022. DOI: 10.1103/PhysRevD.67.044022. arXiv: gr-qc/0207095.
- Pons, Jose et al. (Nov. 1999). “An Exact Riemann Solver for Multidimensional Special Relativistic Hydrodynamics”. In: *Journal of Fluid Mechanics* 422. DOI: 10.1007/978-1-4615-0663-8_71.
- Poudel, Amit et al. (2020). “Increasing the accuracy of binary neutron star simulations with an improved vacuum treatment”. In: *Phys. Rev. D* 102 (10), p. 104014. DOI: 10.1103/PhysRevD.102.104014. URL: <https://link.aps.org/doi/10.1103/PhysRevD.102.104014>.
- Price, D. J. et al. (2006). “Producing Ultrastrong Magnetic Fields in Neutron Star Mergers”. In: *Science* 312.5774, pp. 719–722. DOI: 10.1126/science.1125201. eprint: <https://www.science.org/doi/pdf/10.1126/science.1125201>. URL: <https://www.science.org/doi/abs/10.1126/science.1125201>.

- Radice, David et al. (2018). “Binary Neutron Star Mergers: Mass Ejection, Electromagnetic Counterparts and Nucleosynthesis”. In: *Astrophys. J.* 869.2, p. 130. DOI: 10.3847/1538-4357/aaf054. arXiv: 1809.11161 [astro-ph.HE].
- Radice, David et al. (2016). “Dynamical Mass Ejection from Binary Neutron Star Mergers”. In: *Mon. Not. Roy. Astron. Soc.* 460.3, pp. 3255–3271. DOI: 10.1093/mnras/stw1227. arXiv: 1601.02426 [astro-ph.HE].
- Radice, David et al. (2012). “THC: a new high-order finite-difference high-resolution shock-capturing code for special-relativistic hydrodynamics”. In: *Astron. Astrophys.* 547, A26. DOI: 10.1051/0004-6361/201219735. arXiv: 1206.6502 [astro-ph.IM].
- Raffelt, Georg G. (2001). “Muon-neutrino and tau-neutrino spectra formation in supernovae”. In: *Astrophys. J.* 561, pp. 890–914. DOI: 10.1086/323379. arXiv: astro-ph/0105250.
- Rashti, Alireza et al. (2022). “New pseudospectral code for the construction of initial data”. In: *Phys. Rev. D* 105 (10), p. 104027. DOI: 10.1103/PhysRevD.105.104027. URL: <https://link.aps.org/doi/10.1103/PhysRevD.105.104027>.
- Rezzolla, L. et al. (Sept. 2013). *Relativistic Hydrodynamics*.
- Rezzolla, Luciano et al. (2011). “The missing link: Merging neutron stars naturally produce jet-like structures and can power short Gamma-Ray Bursts”. In: *Astrophys. J. Lett.* 732, p. L6. DOI: 10.1088/2041-8205/732/1/L6. arXiv: 1101.4298 [astro-ph.HE].
- Rosswog, S. et al. (July 2003). “High-resolution calculations of merging neutron stars - II. Neutrino emission”. In: *Monthly Notices of the Royal Astronomical Society* 342, pp. 673–689. DOI: 10.1046/j.1365-8711.2003.06579.x. arXiv: 0302301 [astro-ph].
- Rosswog, Stephan et al. (2003). “High resolution calculations of merging neutron stars. 2: Neutrino emission”. In: *Mon. Not. Roy. Astron. Soc.* 342, p. 673. DOI: 10.1046/j.1365-8711.2003.06579.x. arXiv: astro-ph/0302301.
- Ruffert, M. et al. (Sept. 1995). “Coalescing Neutron Stars as Gamma-Ray Bursters?” In: *Astrophysics and Space Science* 231, pp. 423–426. DOI: 10.1007/BF00658662. eprint: astro-ph/9503027.
- Ruiz, Milton et al. (2020). “Black hole-neutron star coalescence: effects of the neutron star spin on jet launching and dynamical ejecta mass”. In: *Phys. Rev. D* 102.12, p. 124077. DOI: 10.1103/PhysRevD.102.124077. arXiv: 2011.08863 [astro-ph.HE].

- Ruiz, Milton et al. (2011). “Constraint preserving boundary conditions for the Z4c formulation of general relativity”. In: *Phys. Rev. D* 83, p. 024025. DOI: 10.1103/PhysRevD.83.024025. arXiv: 1010.0523 [gr-qc].
- Runge, C. (1895). “Ueber die numerische Auflösung von Differentialgleichungen.” In: *Mathematische Annalen* 46, pp. 167–178. URL: <http://eudml.org/doc/157756>.
- Saad, Yousef (2003). *Iterative Methods for Sparse Linear Systems*. Philadelphia, Pa: Society for Industrial and Applied Mathematics (SIAM). ISBN: 9780898718003. DOI: 10.1137/1.9780898718003.
- Schneider, A. S. et al. (2017). “Open-source nuclear equation of state framework based on the liquid-drop model with Skyrme interaction”. In: *Phys. Rev. C* 96.6, p. 065802. DOI: 10.1103/PhysRevC.96.065802. arXiv: 1707.01527 [astro-ph.HE].
- Sekiguchi, Yuichiro (June 2010). “An implementation of the microphysics in full general relativity: a general relativistic neutrino leakage scheme”. In: *Classical and Quantum Gravity* 27.11, 114107, p. 114107. DOI: 10.1088/0264-9381/27/11/114107. arXiv: 1009.3358 [astro-ph.HE].
- Sekiguchi, Yuichiro (Aug. 2010). “Stellar Core Collapse in Full General Relativity with Microphysics: — Formulation and Spherical Collapse Test —”. In: *Progress of Theoretical Physics* 124.2, pp. 331–379. ISSN: 0033-068X. DOI: 10.1143/PTP.124.331. eprint: <https://academic.oup.com/ptp/article-pdf/124/2/331/5178680/124-2-331.pdf>. URL: <https://doi.org/10.1143/PTP.124.331>.
- Sekiguchi, Yuichiro et al. (2016). “Dynamical mass ejection from the merger of asymmetric binary neutron stars: Radiation-hydrodynamics study in general relativity”. In: *Phys. Rev. D* 93.12, p. 124046. DOI: 10.1103/PhysRevD.93.124046. arXiv: 1603.01918 [astro-ph.HE].
- Shapiro, S L et al. (Jan. 1983). “Black holes, white dwarfs and neutron stars: The physics of compact objects”. In: URL: <https://www.osti.gov/biblio/5869887>.
- Shen, G et al. (Mar. 2011a). “New equation of state for astrophysical simulations”. In: *Physical Review. C, Nuclear Physics* 83.3. ISSN: 0556-2813. DOI: 10.1103/PHYSREVC.83.035802. URL: <https://www.osti.gov/biblio/21499529>.
- Shen, G et al. (June 2011b). “Second relativistic mean field and virial equation of state for astrophysical simulations”. In: *Physical Review. C, Nuclear Physics* 83.6. ISSN: 0556-2813. DOI: 10.1103/PHYSREVC.83.065808. URL: <https://www.osti.gov/biblio/21502830>.
- Shen, H. et al. (2011c). “Relativistic Equation of State for Core-Collapse Supernova simulations”. In: *The Astrophysical Journal Supplement Series* 197.2, p. 20. DOI:

- 10.1088/0067-0049/197/2/20. URL: <https://doi.org/10.1088/0067-0049/197/2/20>.
- (1998a). “Relativistic equation of state of nuclear matter for supernova and neutron star”. In: *Nuclear Physics A* 637.3, pp. 435–450. ISSN: 0375-9474. DOI: [https://doi.org/10.1016/S0375-9474\(98\)00236-X](https://doi.org/10.1016/S0375-9474(98)00236-X). URL: <https://www.sciencedirect.com/science/article/pii/S037594749800236X>.
- Shen, Hong et al. (Nov. 1998b). “Relativistic Equation of State of Nuclear Matter for Supernova Explosion”. In: *Progress of Theoretical Physics* 100.5, pp. 1013–1031. ISSN: 0033-068X. DOI: 10.1143/PTP.100.1013. eprint: <https://academic.oup.com/ptp/article-pdf/100/5/1013/5281814/100-5-1013.pdf>. URL: <https://doi.org/10.1143/PTP.100.1013>.
- Shibata, Masaru (2015). *100 Years of General Relativity: Volume 1 Numerical Relativity*. WORLD SCIENTIFIC. DOI: 10.1142/9692. eprint: <https://www.worldscientific.com/doi/pdf/10.1142/9692>. URL: <https://www.worldscientific.com/doi/abs/10.1142/9692>.
- Shibata, Masaru et al. (Dec. 2011). “Coalescence of Black Hole-Neutron Star Binaries”. In: *Living Reviews in Relativity* 14.1, 6, p. 6. DOI: 10.12942/lrr-2011-6.
- Shibata, Masaru et al. (2014). “Conservative form of Boltzmann’s equation in general relativity”. In: *Phys. Rev. D* 89 (8), p. 084073. DOI: 10.1103/PhysRevD.89.084073. URL: <https://link.aps.org/doi/10.1103/PhysRevD.89.084073>.
- Shibata, Masaru et al. (1995). “Evolution of three-dimensional gravitational waves: Harmonic slicing case”. In: *Phys. Rev. D* 52 (10), pp. 5428–5444. DOI: 10.1103/PhysRevD.52.5428. URL: <https://link.aps.org/doi/10.1103/PhysRevD.52.5428>.
- Shibata, Masaru et al. (Aug. 2005). “Magnetohydrodynamics in full general relativity: Formulation and tests”. In: *Physical Review. D, Particles Fields* 72.4. ISSN: 0556-2821. DOI: 10.1103/PhysRevD.72.044014. URL: <https://www.osti.gov/biblio/20711349>.
- Shu, Chi-Wang et al. (1988). “Efficient Implementation of Essentially Non-oscillatory Shock-capturing Schemes”. In: *J. Comput. Phys.* 77.2, pp. 439–471. ISSN: 0021-9991. DOI: 10.1016/0021-9991(88)90177-5. URL: [http://dx.doi.org/10.1016/0021-9991\(88\)90177-5](http://dx.doi.org/10.1016/0021-9991(88)90177-5).
- Siegel, Daniel M. et al. (2018). “Recovery schemes for primitive variables in general-relativistic magnetohydrodynamics”. In: *Astrophys. J.* 859.1, p. 71. DOI: 10.3847/1538-4357/aabcc5. arXiv: 1712.07538 [astro-ph.HE].

- Sigurdsson, Steinn (2003). “Black holes and pulsar binaries”. In: *ASP Conf. Ser.* 302. Ed. by Matthew Bailes et al., p. 391. arXiv: astro-ph/0303312.
- Spivak, Michael David (1975). “A comprehensive introduction to differential geometry”. In.
- Sumiyoshi, K. et al. (2005). “Postbounce Evolution of Core-Collapse Supernovae: Long-Term Effects of the Equation of State”. In: *The Astrophysical Journal* 629.2, pp. 922–932. DOI: 10.1086/431788. URL: <https://doi.org/10.1086/431788>.
- Sun, Lunan et al. (Feb. 2022). “Jet Launching from Binary Neutron Star Mergers: Incorporating Neutrino Transport and Magnetic Fields”. In: arXiv: 2202.12901 [astro-ph.HE].
- SXS Gravitational Waveform Database* (n.d.). <https://data.black-holes.org/waveforms/catalog.html>.
- Tacik, Nick et al. (2015). “Binary Neutron Stars with Arbitrary Spins in Numerical Relativity”. In: *Phys. Rev. D* 92.12. [Erratum: Phys.Rev.D 94, 049903 (2016)], p. 124012. DOI: 10.1103/PhysRevD.92.124012. arXiv: 1508.06986 [gr-qc].
- Tacik, Nick et al. (2016). “Initial data for black hole–neutron star binaries, with rotating stars”. In: *Class. Quant. Grav.* 33.22, p. 225012. DOI: 10.1088/0264-9381/33/22/225012. arXiv: 1607.07962 [gr-qc].
- Taniguchi, Keisuke et al. (2005). “Black hole-neutron star binaries in general relativity: Effects of neutron star spin”. In: *Phys. Rev. D* 72 (4), p. 044008. DOI: 10.1103/PhysRevD.72.044008. URL: <https://link.aps.org/doi/10.1103/PhysRevD.72.044008>.
- (2007). “Quasiequilibrium black hole-neutron star binaries in general relativity”. In: *Phys. Rev. D* 75, p. 084005. DOI: 10.1103/PhysRevD.75.084005. arXiv: gr-qc/0701110.
- (2006). “Quasiequilibrium sequences of black-hole-neutron-star binaries in general relativity”. In: *Phys. Rev. D* 74, p. 041502. DOI: 10.1103/PhysRevD.74.041502. arXiv: gr-qc/0609053.
- (2008). “Relativistic black hole-neutron star binaries in quasiequilibrium: Effects of the black hole excision boundary condition”. In: *Phys. Rev. D* 77, p. 044003. DOI: 10.1103/PhysRevD.77.044003. arXiv: 0710.5169 [gr-qc].
- Taylor, L. R. et al. (1987). *Numerical Recipes: The Art of Scientific Computing*. Vol. 56. 1. Cambridge, UK New York: Cambridge University Press, p. 374. ISBN: 978-0521880688. DOI: 10.2307/4830.

- Thierfelder, Marcus et al. (2011a). “Numerical relativity simulations of binary neutron stars”. In: *Phys. Rev. D* 84 (4), p. 044012. DOI: 10.1103/PhysRevD.84.044012. URL: <https://link.aps.org/doi/10.1103/PhysRevD.84.044012>.
- Thierfelder, Marcus et al. (2011b). “Trumpet solution from spherical gravitational collapse with puncture gauges”. In: *Phys. Rev. D* 83 (6), p. 064022. DOI: 10.1103/PhysRevD.83.064022. URL: <https://link.aps.org/doi/10.1103/PhysRevD.83.064022>.
- Thorne, Kip S. (Feb. 1981). “Relativistic radiative transfer: moment formalisms”. In: *Monthly Notices of the Royal Astronomical Society* 194.2, pp. 439–473. ISSN: 0035-8711. DOI: 10.1093/mnras/194.2.439. eprint: <https://academic.oup.com/mnras/article-pdf/194/2/439/3033490/mnras194-0439.pdf>. URL: <https://doi.org/10.1093/mnras/194.2.439>.
- Tichy, Wolfgang (Sept. 2009). “A new numerical method to construct binary neutron star initial data”. In: *Classical and Quantum Gravity* 26.17, 175018, p. 175018. DOI: 10.1088/0264-9381/26/17/175018. arXiv: 0908.0620 [gr-qc].
- Tichy, Wolfgang (2012). “Constructing quasi-equilibrium initial data for binary neutron stars with arbitrary spins”. In: *Phys. Rev. D* 86, p. 064024. DOI: 10.1103/PhysRevD.86.064024. arXiv: 1209.5336 [gr-qc].
- Tichy, Wolfgang (2016). “The initial value problem as it relates to numerical relativity”. In: *Reports on Progress in Physics* 80.2, p. 026901. DOI: 10.1088/1361-6633/80/2/026901. URL: <https://doi.org/10.1088/1361-6633/80/2/026901>.
- Tichy, Wolfgang et al. (2019). “Constructing binary neutron star initial data with high spins, high compactnesses, and high mass ratios”. In: *Phys. Rev. D* 100.12, p. 124046. DOI: 10.1103/PhysRevD.100.124046. arXiv: 1910.09690 [gr-qc].
- Toro, E.F. (2013). *Riemann Solvers and Numerical Methods for Fluid Dynamics: A Practical Introduction*. Springer Berlin Heidelberg. ISBN: 9783662034903. URL: <https://books.google.de/books?id=zKtCAAQBAJ>.
- Tsokaros, Antonios et al. (2015). “New code for quasiequilibrium initial data of binary neutron stars: Corotating, irrotational, and slowly spinning systems”. In: *Phys. Rev. D* 91.10, p. 104030. DOI: 10.1103/PhysRevD.91.104030. arXiv: 1502.05674 [gr-qc].
- Typel, S. et al. (2010). “Composition and thermodynamics of nuclear matter with light clusters”. In: *Phys. Rev. C* 81, p. 015803. DOI: 10.1103/PhysRevC.81.015803. arXiv: 0908.2344 [nucl-th].

- Tóth, Gábor (2000). “The $\nabla \cdot B = 0$ Constraint in Shock-Capturing Magnetohydrodynamics Codes”. In: *Journal of Computational Physics* 161.2, pp. 605–652. ISSN: 0021-9991. DOI: <https://doi.org/10.1006/jcph.2000.6519>. URL: <https://www.sciencedirect.com/science/article/pii/S0021999100965197>.
- Uryu, Koji et al. (2012). “A new code for equilibriums and quasiequilibrium initial data of compact objects”. In: *Phys. Rev. D* 85, p. 064014. DOI: 10.1103/PhysRevD.85.064014. arXiv: 1108.3065 [gr-qc].
- Van Riper, K A (June 1982). “Stellar core collapse: II. Inner core bounce and shock propagation”. In: *Astrophys. J.; (United States)* 257:2. DOI: 10.1086/160032. URL: <https://www.osti.gov/biblio/7064043>.
- van Riper, K. A. et al. (Oct. 1981). “Stellar core collapse. I - Infall epoch”. In: *The Astrophysical Journal* 249, pp. 270–289. DOI: 10.1086/159285.
- Weyhausen, Andreas et al. (2012). “Constraint damping for the Z4c formulation of general relativity”. In: *Phys. Rev. D* 85, p. 024038. DOI: 10.1103/PhysRevD.85.024038. arXiv: 1107.5539 [gr-qc].
- Wilson., J. R (1972). “Numerical Study of Fluid Flow in a Kerr Space”. In: *Astrophysical Journal* 173, p. 431.
- York, James W. (1999). “Conformal “Thin-Sandwich” Data for the Initial-Value Problem of General Relativity”. In: *Phys. Rev. Lett.* 82 (7), pp. 1350–1353. DOI: 10.1103/PhysRevLett.82.1350. URL: <https://link.aps.org/doi/10.1103/PhysRevLett.82.1350>.
- York, James W. Jr. (1979). “Kinematics and dynamics of general relativity”. In.
- Zanna, L. Del et al. (2002). “An efficient shock-capturing central-type scheme for multidimensional relativistic flows. I. hydrodynamics”. In: *Astron. Astrophys.* 390, p. 1177. DOI: 10.1051/0004-6361:20020776. arXiv: astro-ph/0205290.

Published content and contributions

Alireza Rashti, Francesco Maria Fabbri, Bernd Brügmann, Swami Vivekanandji Chaurasia, Tim Dietrich, Maximiliano Ujevic, and Wolfgang Tichy. New pseudospectral code for the construction of initial data. *Phys. Rev. D*, 105:104027, May 2022.

Alireza Rashti, Francesco Maria Fabbri, Bernd Brügmann, Swami Vivekanandji Chaurasia, Tim Dietrich, Maximiliano Ujevic, and Wolfgang Tichy. Elliptica: a new pseudo-spectral code for the construction of initial data. *gr-qc*, arXiv:2109.14511, September 2021.

Andrea Endrizzi, Albino Perego, Francesco M. Fabbri, Lorenzo Branca, David Radice, Sebastiano Bernuzzi, Bruno Giacomazzo, Francesco Pederiva, and Alessandro Lovato. Thermodynamics conditions of matter in the neutrino decoupling region during neutron star mergers. *Eur. Phys. J. A*, 56(1):15, 2020.

Swami Vivekanandji Chaurasia, Tim Dietrich, Maximiliano Ujevic, Kai Hendriks, Reetika Dudi, Francesco Maria Fabbri, Wolfgang Tichy, and Bernd Brügmann. Gravitational waves and mass ejecta from binary neutron star mergers: Effect of the spin orientation. *Phys. Rev. D*, 102(2):024087, 2020.

Acknowledgements

I am grateful to Prof. Bernd Brügmann, who welcomed me into his research group and allowed me to complete this thesis work in Jena. I have deeply valued his mentorship and guidance during these years. I also consider it to be an honor to have been a member of the numerical relativity group and of the TPI.

I am especially grateful to Prof. Tim Dietrich for his constant counsel and valuable input throughout my all Ph.D. His help and support have been of extraordinary importance during my work. I want to thank him also for taking the time to go through this thesis and giving me corrections and suggestions.

Any amount of appreciation will fall short in expressing my gratitude to Alireza Rashti, who allowed me to join his project side by side with him, despite the geographical distance. I want also to renew my gratitude to him for the extensive and valuable conversation we had during this time. On a related note, I am thankful to Prof. Maximiliano Ujevic Tonino and Prof. Wolfgang Tichy for the discussions on the topic of mixed binaries and their precious help.

I want to convey my gratitude to Prof. Sebastiano Bernuzzi for allowing me to collaborate on the research of his group and for his helpful advice along the way.

I am indebted to Dr. Swami Vivekanandji Chaurasia and Dr. Andrea Endrizzi for involving me in their projects and their persistence in tutoring me during that time.

I want to thank Sarah and Daniela for their patience in reviewing this thesis and for giving me their corrections and improvements. I will miss you as colleagues and friends. I am grateful to Ondrej, my office mate, and then to Max, Rossella, Florian, Vseva, Roxana, Reetika, Sohrab, Nestor, Sarp, and Hannes for being splendid colleagues and for brightening the time spent working together.

I am and always be very fond of all the memory that I have built during my time in Jena. The countless people I've met turned this part of my life into an invaluable treasure chest of experiences and emotions that I will keep with myself forever. So thanks Serena for being with me since the day we met. And thanks Francesco and Matteo, always present in and out of work, Ale, Lola, Martino, Sara and Davide. The

bonds born in this strange and magical city will extend and tighten despite the distance and will stay with us forever.

I am beholden to my family and friends who, for most of the time, could not be here physically, nonetheless without whose support none of this would have been possible. Mum, Dad, your endless love and affection have sustained me in my darkest moments. Dad, I would have loved for you to be here at this moment, to see the conclusion of this chapter of my life. I will miss you.

Curriculum Vitae

Personal details

Name: Francesco Maria
Surname: Fabbri
Address: via dei Cardellini 9
51017, Pescia (PT)
Italy
Telephone: +39 333 5347112
Date of birth: 11/05/1991
Nationality: Italian

Education:

2017-2022 Doctoral Student in Theoretical Physics Institute at University of Jena
2016-2017 Thesis work in the Numerical Relativity group at University of Trento
2014-2017 Master's Degree in in Astrophysics and Cosmology at University of Trieste
2010-2014 Bachelor's Degree in Physics at University of Pisa
2010 High School qualification in Scientific studies at
"Liceo Scientifico Tecnologico E.Fermi" in Lucca (IT)

Professional Experience:

2017 - 2022 Research Assistant in Theoretical Physics at Institute University of Jena
2016 - 2017 Research Assistant at INFN (IT)

Teaching:

2021-2022, WS Laboratory tutor "Numerical Treatment of Navier-Stokes-Equations"
2021, SS Laboratory tutor for "Numerical Treatment of Navier-Stokes-Equations"
2019-2020, WS Tutoring assistant for "Computational Physics 4: Machine Learning"
2018-2019, WS Tutoring assistant for "Computational Physics 3: Machine Learning"

Datum:

Unterschrift

Zusammenfassung

Die Ära der Gravitationswellenastronomie begann mit dem Erfolg des ersten Beobachtungslaufs der LIGO-Kollaboration und der VIRGO-Kollaboration. Die unglaubliche Leistung der großen Laserinterferometer machte umfangreiche Studien auf dem Gebiet der kompakten astrophysikalischen Objekte wie Schwarze Löcher und Neutronensterne erforderlich. Heute, sieben Jahre nach diesem Ereignis, erfährt das Forschungsgebiet eine bemerkenswerte Erweiterung, bekräftigt durch die Entdeckung eines Signals, das von der Verschmelzung eines binären Neutronensterns ausgeht, zusammen mit seinem elektromagnetischen Gegenstück, und in jüngerer Zeit durch die ersten Entdeckungen von Signalen, die von gemischten kompakten Doppelsternen stammen, d.h. von Doppelsternen aus Schwarzen Löchern und Neutronensternen.

In dieser Dissertation befassen wir uns mit verschiedenen Aspekten der Verschmelzung kompakter Objekte, einschließlich der Einbeziehung neuer physikalischer Aspekte in den bereits leistungsstarken numerischen Relativitätscode BAM und der Untersuchung spezifischer Systeme kompakter Objekte.

Wir untersuchen zunächst die Behandlung von Neutrinos im Fall von Verschmelzungen von Binären Neutronensternen und ein Werkzeug zur Identifizierung und weiteren Analyse von Regionen, die gefangene Neutrinos enthalten, im heißen Überrest solcher Verschmelzungen. Neutrinos spielen in der Tat eine Schlüsselrolle bei den schnellen Prozessen, die die Bildung von Elementen in den dynamischen Ejekta, die während diesen katastrophalen Ereignissen ausgestoßen werden, charakterisieren.

Im Folgenden untersuchen wir eine Vielzahl von Konfigurationen gemischter kompakter Doppelsternsysteme. Nach der Entwicklung des neuen ID-Codes *Elliptica* und den zur Überprüfung seiner Genauigkeit unternommenen Schritten, nutzen wir seine Fähigkeit, Sätze von physikalischen Systemen mit verschiedenen Eigenschaften zu entwickeln. Bei der Erkundung des Parameterraums untersuchen wir verschiedene Spin-Konfigurationen und Größen von Einzelobjekten und deren Auswirkungen auf die Fusionsdynamik.

Selbstständigkeitserklärung

Ich erkläre hiermit, dass ich die vorliegende Arbeit selbständig, ohne unzulässige Hilfe Dritter und ohne Benutzung anderer als der angegebenen Hilfsmittel und Literatur angefertigt habe. Die aus anderen Quellen direkt oder indirekt übernommenen Daten und Konzepte sind unter Angabe der Quelle gekennzeichnet. Bei der Auswahl und Auswertung dieser Arbeit haben mir die nachstehend aufgeführten Personen in beratender Weise unentgeltlich geholfen:

- Prof. Bernd Brüggemann
- Prof. Tim Dietrich
- Prof. Maximiliano Ujevic
- Prof. Wolfgang Tichy
- M.Sc. Alireza Rashti
- Dr. Andrea Endrizzi
- Dr. Swami Vivekanandji Chaurasia
- Prof. Sebastiano Bernuzzi

In Bereichen bei denen auf Arbeit anderer zurückgegriffen wurde, ist dies ausdrücklich in der Arbeit erwähnt. Weitere Personen waren an der inhaltlich-materiellen Erstellung der vorliegenden Arbeit nicht beteiligt. Insbesondere habe ich hierfür nicht die entgeltliche Hilfe von Vermittlungs- bzw. Beratungsdiensten (Promotionsberater oder andere Personen) in Anspruch genommen. Niemand hat von mir unmittelbar oder mittelbar geldwerte Leistungen für Arbeiten erhalten, die im Zusammenhang mit dem Inhalt der vorgelegten Dissertation stehen. Die Arbeit wurde bisher weder im In- noch im Ausland in gleicher oder ähnlicher Form einer anderen Prüfungsbehörde vorgelegt. Ich versichere ehrenwörtlich, dass ich nach bestem Wissen die reine Wahrheit gesagt und nichts verschwiegen habe.

Datum:

Unterschrift

Declaration of Authorship

I, Francesco Maria FABRI (M.Sc.), declare that this thesis titled, “Compact Binary Merger Simulations in Numerical Relativity ” and the work presented in it are my own. I confirm that:

- This work was done wholly or mainly while in candidature for a research degree at this University.
- Where any part of this thesis has previously been submitted for a degree or any other qualification at this University or any other institution, this has been clearly stated.
- Where I have consulted the published work of others, this is always clearly attributed.
- Where I have quoted from the work of others, the source is always given. With the exception of such quotations, this thesis is entirely my own work.
- I have acknowledged all main sources of help.
- Where the thesis is based on work done by myself jointly with others, I have made clear exactly what was done by others and what I have contributed myself.

Signed:

Date:
